Study of laser propagation and soliton formation in strongly magnetized plasmas

Feng Wu

Abstract

The laser plasma interactions in the presence of strong magnetic field have received attractions recently due to the success generation of kilo-tesla magnetic field. The introduction of perpendicular or parallel magnetic field could potentially benefit many applications, e.g. the plasma based particle acceleration, the harmonic generation, the tunable terahertz radiation generation and magnetically assisted fast ignition. This thesis is thus devoted to study the effects of strong parallel magnetic field on the laser plasma interactions, specifically on the various laser propagation modes and soliton formation by both the particle-in-cell (PIC) simulations and theoretical analysis.

As an introduction, the relativistic dispersion relation and single particle orbit inside the relativistic laser field in the presence of strong magnetic field are first discussed. Then the effects of strong magnetic field on the laser propagation modes and heating in plasmas are studied by the PIC simulations. The various linear propagation modes (left and right hand circularly polarized waves, electron cyclotron wave) and their conversion in the inhomogeneous plasma areas are analyzed. A solitary wave with lower frequency compared to the incident laser frequency is observed in a density well, which greatly enhances the heating of the laser pulse. The parametric window of the laser intensity and magnetic field for the generation of solitons is identified. The soliton properties and stabilities are investigated.

To have a better understanding of the solitons, the soliton formation in strongly magnetized plasmas is analyzed systematically in the framework of relativistic, warm fluid model. Three nonlinear ordinary differential equations describing the coupling between the longitudinal and transverse waves due to the density perturbation and relativistic effects are obtained. By assuming appropriate dispersion relations, the general criterion for the existence of solitons is found. Then the coupled soliton equations are solved numerically through the shooting method or the rational spectral method. Based on the soliton equations and numerical calculations, a variety of solitary waves including the continuous spectrum bright solitons, single-hump and multi-hump dark solitons are identified. Their properties and appearance with different magnetic fields and soliton frequencies are discussed.

For the case of bright solitons, the parametric region of the magnetic field and soliton frequency for the existence of solitons are obtained in both cold and warm plasmas. The ion’s effects on the soliton formation

are investigated, where they are found to play an important role especially when the magnetic field is opposite to the soliton propagation direction. The numerical calculations show that in the limit of immobile ions, the bright soliton tends to be peaked and stronger as the magnetic field increases while it becomes broader and smaller as the soliton frequency increases.

For dark solitons, the wavenumber is proved to be of great importance in determining the parametric region of magnetic field and soliton frequency required for the existence of solitons. In warm plasmas, dark solitons with multiple humps in both the scalar and vector potential profiles are observed. The numerical calculations without ion's motion show that the dark soliton amplitude decreases with increasing magnetic field and decreasing soliton frequency. These tendencies are opposite to the bright solitons. However, for both bright and dark solitons, the temperature effects suppress the soliton amplitude.

Keywords: propagation modes, dispersion relation, bright and dark soliton, dynamical systems theory, PIC simulations

Acknowledgments

First of all, I would like to express my deepest gratitude to my supervisor Prof. Yasuaki Kishimoto. I am very thankful to him for his wise guidance and encouragement during my research, for his generosity in sharing knowledge and methodology to find scientific nature and allowing me the freedom to pursue on my own path. Without his support, I would not have been able to finish this PhD study. I hope what I learned these years and his efforts were not in vain.

I am very grateful to Prof. Jiquan Li for his continuous help and enlightening discussion and advice along these years. His patient discussions and revisions on my manuscript help me a lot in improving my writing skills. Also I thank Prof. Kenji Imadera for his valuable comments on my research and kind help on the lab affairs.

I would like to thank all the laboratory members, especially, Ms. Takahashi who patiently processed all my questions and daily lab issues. I thank Daiki Kawahito and Ryutaro Matsui not only for their useful discussions on understanding the physical meanings of numerical simulations but also for their enthusiastic explanations on Japanese way of life. Special thanks to Ali Ahamd for his endurance on my complaints and continuous encouragement during my frustrating times. Also I thank Philippe Mathieu for his company and sending me cookies from France.

I would like to give my sincere thanks to Zhang Jun, who explored with me the beauty of Kyoto and shared with me the tears and joys during the first year living in Japan. I thank Wang Wei, Liu Hairui, Lin Qing, Zang Jiachen and Fu Jiaxin for spending their precious time with me to enjoy the holidays. I was lucky to have all the friends and the fun and experiences I had are unforgettable.

Finally, many thanks to my parents and my sister. They are always a great source of power for me to keep on going.

Contents

1. Introduction

Plasma, usually referred as the fourth state of matter, is a matter with macro spatiotemporal scales which contains enough free charged particles for its dynamics to be dominated by the electromagnetic forces. The term “plasma” was coined by Langmuir in 1928 to describe the ionized regions in gas discharges. Though on the earth, plasma only exists in limited areas such as the earth’s ionosphere, fire flames and lightning, it is the most abundant form of ordinary matter in the universe. For instance, the sun and stars are made of hot and dense plasmas and much of the interstellar space is filled with cold and rarefied plasmas. The parameters of the plasmas, e.g. density and temperature, can vary many orders of magnitude as illustrated by Fig. 1.1.

From the second half of the twentieth century, much of the development of plasma physics was motivated by the pursuit of controlled thermonuclear fusion on the one hand and the astrophysical and space physics on the other hand. Nowadays, the plasma physics has developed into many fields of research and applications such as the space plasma physics, the low temperature industrial plasmas and the high temperature fusion plasmas. Among these sub-disciplines, the laser plasma interactions have always been one of the most active and exciting fields ever since the advent of laser in the 1960s. Specifically, in the past three decades, due to the rapid development of chirped pulse amplification (CPA) [1, 2] and Kerr lens mode-locking [3, 4] techniques, ultra-intense laser pulses with peak powers up to several petawatt (PW) became available. As a comparison, the total power of sunlight striking earth’s atmosphere is estimated around 174 PW. When such laser systems are focused onto micro spot sizes, they can generate electromagnetic intensities up to $10^{22} W/cm^2$. Such intensities can create novel states of matter and a variety of phenomena can occur including the wake field generation, ultrahigh magnetic field generation, relativistic self-focusing and transparency, nonlinear wave modulation, high harmonic radiation generation, electron and ion acceleration and so on (see Fig. 1.2).

The ultra-intense laser plasma interactions can have many applications, e.g. the plasma based particle accelerator, the compact radiation source and the laser inertial confinement fusion. To accomplish and develop these applications, a profound and detailed understanding of the ultra-intense laser plasma interactions is necessary.

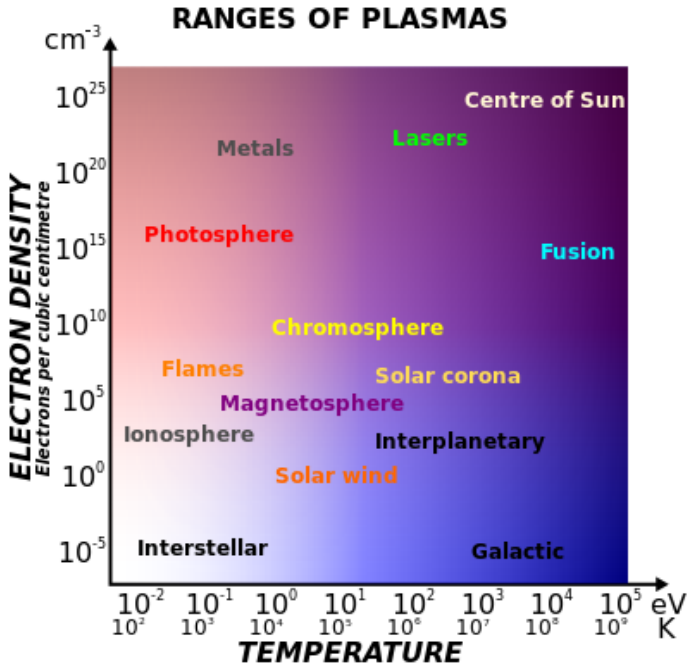

Fig. 1.1. The remarkable range of temperatures and densities of plasmas. Density increases upwards and temperature increases towards the right. The free electrons in a metal may be considered as an electron plasma. [Adapted from A. L. Peratt [5]].

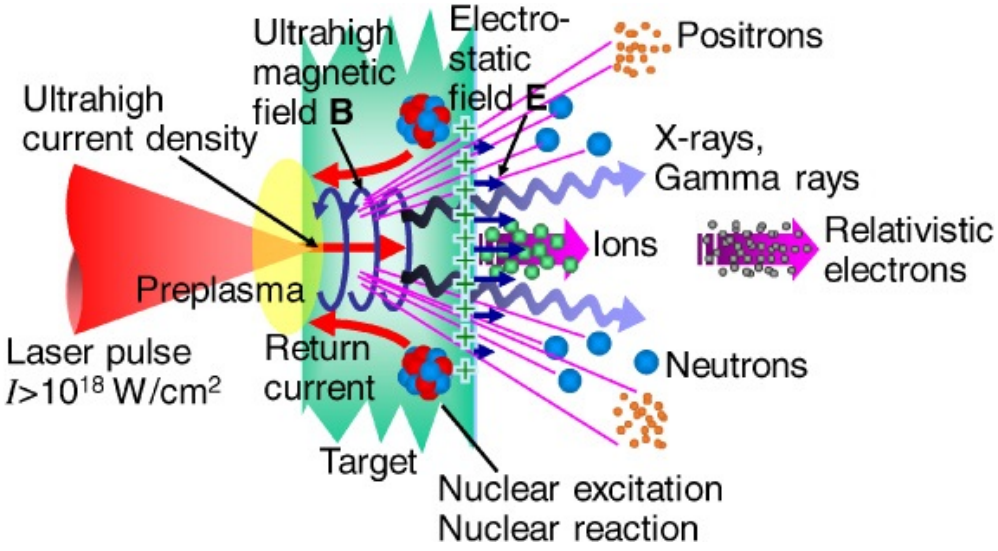

Fig. 1.2. Sketch of ultra-intense laser plasma interactions. The electrons are preferentially pushed forward, followed by the ions, leading to a charge separation field. The plasma emits high energy electrons, ions and various radiations including high order harmonics, X-rays, gamma rays, terahertz radiation, etc. Also megagauss class magnetic fields can be produced by the enormous current density of the hot electrons. [Adapted from H. Daido [6]].

1.1 Ultra-intense laser plasma interactions

A key parameter in the discussion of the ultra-intense laser plasma interactions is the dimensionless laser amplitude a, which is defined as the normalized quiver momentum of the electron in the laser field,

$$a = \frac{eE_0}{m_e \omega_0 c} \tag{1.1}$$

Here ω_0 and E_0 are the round frequency and electric field of the laser, $-e$ and m_e are the electron charge and mass and c is the speed of light. Another commonly used expression is,

$$a = \left[\frac{I\lambda_0^2}{1.37 \times 10^{18} W/cm^2 \cdot \mu m^2}\right]^{1/2} \tag{1.2}$$

Here a linearly polarized laser is assumed and the laser intensity $I = (c/8\pi)E_0^2$ is in unit of W/cm^2 and the wavelength λ_0 is in unit of microns. For circularly polarized laser, the value of the denominator in Eq. (1.2) is two times larger. For a $1\mu m$ wavelength laser, the intensity is around $10^{18} W/cm^2$ when $a \sim 1$. In this regime, the electron motion inside the laser field becomes relativistic. Note that the dimensionless amplitude $a_i \equiv eE_0/(m_i \omega_0 c)$, where m_i is the ion mass, remains much less than unity. The intensity value corresponding to $a_i \sim 1$ for a $1\,\mu m$ wavelength laser is about $5 \times 10^{24}\, W/cm^2$. Hence, for all the experiments performed up to now and nearly all the theoretical calculations the ions are non-relativistic. At even higher intensities, e.g. on order of $10^{29} W/cm^2$ for a $1\mu m$ wavelength laser, the work done by the laser field over a Compton wavelength ($\lambda = h/m_e c$ with h the Planck constant) is comparable to $m_e c^2$. In this case, electron-positron pair can be produced from the vacuum. In this thesis, we only consider a is of order unity, e.g. I is around $10^{17} - 10^{20} W/cm^2$.

1.1.1 Basic physical concepts

Basically, there are two kinds of interactions between the charged particles and the intense laser waves. The first one is the laser single-particle interactions, e.g. the scattering of electromagnetic wave by a particle. The second is the laser plasma interactions where collective effects come to play. For illustrative purpose, we consider a laser propagating in the z direction with the amplitude $\boldsymbol{E} = E_0\big[\cos(k_0 z - \omega_0 t)\,\delta_x \boldsymbol{e}_x + \sin(k_0 z - \omega_0 t)\,\delta_y \boldsymbol{e}_y\big]$. Here ω_0, k_0 are the frequency and wavenumber of the laser and $\boldsymbol{e}_x, \boldsymbol{e}_y$ are the unit vectors in the x and y directions. (δ_x, δ_y) are the factors describing the polarization direction, e.g. $(\delta_x, \delta_y) = (1,0)$ is for linearly polarization in the x direction and $(\delta_x, \delta_y) = (\sqrt{2}/2, \sqrt{2}/2)$ is for circularly polarization. Note that $\delta_x^2 + \delta_y^2 \equiv 1$.

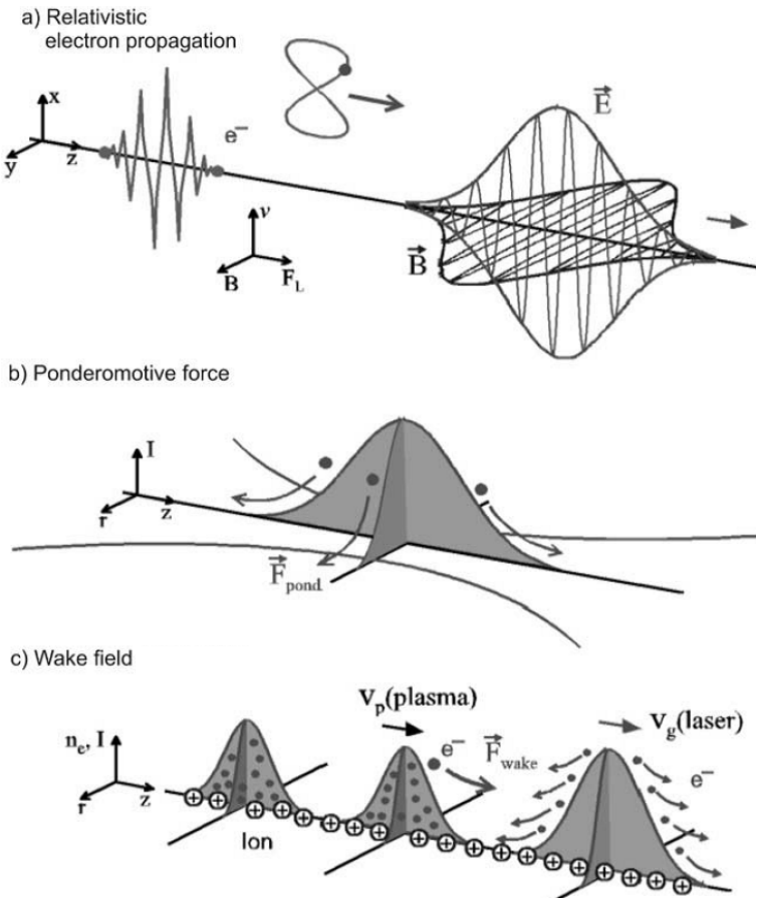

Fig. 1.3. (a) The relativistic electron motion inside the linearly polarized laser field; the Lorentz force pushes the electrons forward which results in an "8-figure" motion in the average rest frame. (b) The laser intensity versus propagation (z) and radial (r) directions; the effective Lorentz force pushed the electrons out of the high intensity areas. (c) Plasmas density versus z and r; the ponderomotive force pushes the electrons and the charge separation between electrons and ions produces a strong longitudinal static electric field which can be used to accelerate the electrons. [Adapted from H. Schwoerer [8]].

In the laser single particle interactions, the electron motion inside the laser field is governed by the Lorentz equation,

$$\frac{d\boldsymbol{p}}{dt} = -e\left(\boldsymbol{E} + \frac{\boldsymbol{v}}{c} \times \boldsymbol{B}\right) \tag{1.3}$$

with $\boldsymbol{p}$, $\boldsymbol{v}$ the electron momentum and velocity and $\boldsymbol{E}, \boldsymbol{B}$ the laser electric and magnetic field. In the non-relativistic regime, e.g. $a \ll 1$, the electron motion inside the laser field is an oscillation at the laser frequency along the laser polarization direction. However, the magnetic field of the laser wave becomes significant when $a \gtrsim 1$ and the electron will develop a motion along the laser propagation direction due to the $v \times B$ force. For linearly polarized laser, this longitudinal motion oscillates at double of the laser frequency and the amplitude is proportional to a^2 whereas the transverse motion scales as a. Hence, when $a > 1$ the longitudinal motion dominates the transverse one. In the frame moving at the average electron velocity, this electron motion is an "8-figure" as shown in Fig. 1.3(a). For circularly polarized laser, the electrons do not oscillate in the propagation direction and the transverse motion is a circle. [7]

One of the consequences of this relativistic "8-figure" motion is the *harmonic generation*, or *nonlinear Thomson scattering*. According to the classical electrodynamics, electrons with this kind of motion should emit radiations at multiples of the laser frequency. In other words, the incident laser wave is scattered by the electrons and the frequency of the first harmonic of the scattered radiation is same as the incident one in the reference frame where the electrons are at rest. Hence, if the electrons are initially from an energetic electron beams, the scattered wave can be up-shifted to the X-ray regime due to the Doppler effects. This mechanism provides a way to generate X-rays which can be used to resolve various physical, chemical or biological reactions with ultrashort spatiotemporal scales.

For the plane laser wave, the electron returns to rest with some displacement in the z direction after the laser pulse passes over it. However, when the laser pulse has spatial or temporal dependences, e.g. the Gaussian laser pulse $E = E_0 \exp(-r^2/r_0^2)\cos(k_0 z - \omega_0 t)$ as shown in Fig. 1.3(b), the electrons can get energy from the laser field irreversibly by the so called *ponderomotive force*. Here r_0 is the laser spot size. The mechanism of ponderomotive force is simple. Imaging an electron is initially at the optical axes $r = 0$, it will accelerate outwards in the first half of the laser period but never return to the original position at the second half of the laser period due to the decrease of the laser intensity. Hence, electrons will gradually be expelled from the high intensity region and the ponderomotive force can be viewed as a radiation pressure. The derivation of ponderomotive force can be found by rewriting Eq. (1.3) in the form of vector potential $\boldsymbol{A}$ and scalar potential ϕ,

$$\frac{d\boldsymbol{p}}{dt} = \frac{e}{c}\frac{\boldsymbol{\partial A}}{\boldsymbol{\partial t}} + e\nabla\phi - \frac{\boldsymbol{p}}{\gamma m_e} \times \left(\nabla \times \frac{e}{c}\boldsymbol{A}\right) \tag{1.4}$$

Here $\boldsymbol{E} = -(1/c)\,\partial\boldsymbol{A}/\partial t - \nabla\phi$, $\boldsymbol{B} = \nabla \times \boldsymbol{A}$ have been used and $\gamma = \sqrt{1 + (p/m_e c)^2}$ is the electron relativistic factor. If $\boldsymbol{\nabla} \times (\boldsymbol{p} - e\boldsymbol{A}/c) = 0$ is satisfied, e.g. $\boldsymbol{p} = e\boldsymbol{A}/c + \boldsymbol{\nabla} f$ with f an arbitrary function, using $d/dt = \partial/\partial t + \boldsymbol{v} \cdot \nabla$, Eq. (1.4) can be written as [9],

$$\begin{aligned} \frac{\partial}{\partial t}\left(\boldsymbol{p} - \frac{e}{c}\boldsymbol{A}\right) &= e\nabla\phi - \frac{\boldsymbol{p}}{\gamma m_e} \times \left[\nabla \times \left(\frac{e}{c}\boldsymbol{A}\right)\right] - \left(\frac{\boldsymbol{p}}{\gamma m_e} \cdot \nabla\right)\boldsymbol{p} \\ &= m_e c^2 \nabla\left(\frac{e\phi}{m_e c^2} - \gamma\right) \end{aligned} \tag{1.5}$$

Here the identity $\nabla\boldsymbol{p^2}/2 = \boldsymbol{p} \times (\nabla \times \boldsymbol{p}) + (\boldsymbol{p} \cdot \nabla)\boldsymbol{p}$ has been used in obtaining the second equation. In one dimensional (1D) or three dimensional (3D) with broad laser spot size $r_0 \gg \lambda_0$ cases, the transverse canonical momentum is conserved or $\boldsymbol{p}_\perp = e\boldsymbol{A}/c$. Hence the left hand side of Eq. (1.5) represents the change of longitudinal momentum while on the right hand side $e\nabla\phi$ is the electrostatic field force produced by the charge separation. Thus, the generalized nonlinear ponderomotive force is expressed as,

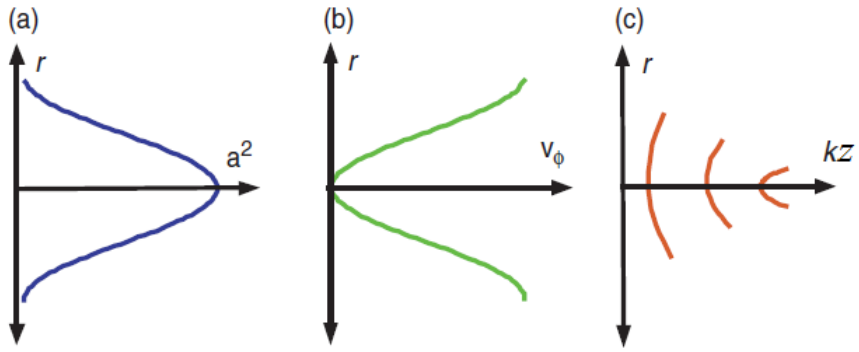

Fig. 1.4. (a) The laser intensity versus radial direction; (b) The phase velocity of the laser depends on the laser intensity; (c) The distortion of wave front due to different phase velocities. [Adapted from D. Umstadter [14]].

$$\boldsymbol{F} = -m_e c^2 \nabla \gamma \tag{1.6}$$

For a linearly polarized laser, the relativistic factor is related to the dimensionless laser amplitude as $\gamma = 1 + a^2/2$ and the ponderomotive force becomes $\boldsymbol{F} = -m_e c^2 \nabla (a^2/2)$. It is proportional to the negative gradient of the laser intensity. Since a is inversely proportional to the particle's mass, the ponderomotive force acting on the electrons is much larger than on the ions. Hence the electrons are easily to be pushed out of the high intensity laser region.

In plasmas, one of the immediate effects of the ponderomotive force is the *wake field generation*. [10] The electrons are first pushed forward by the ponderomotive force until the laser pulse overtakes them and pushes them backwards. Due to the mass difference between the electrons and ions, density variation or charge separation will be generated as shown in Fig. 1.3(c). The restoring force causes the electrons to oscillate at the plasma frequency which leads to an electrostatic wake wave with its phase velocity nearly equals to the group velocity of the laser. In low-density plasmas, this velocity is close to the speed of light and electrons can be continuously accelerated in the wake wave. This acceleration mechanism is called as the *wake field acceleration*. Usually, the accelerated electrons are of quasi-thermal spectrum. However, by carefully controlling the laser and plasma parameters, in particular, matching the acceleration length to the dephasing length, high quality electron bunches with high average energy, narrow energy spread and low divergence can be generated. [11, 12, 13] The major advantage of this wake field acceleration is its ability to sustain extremely large acceleration gradients. For instance, the acceleration gradient ($\sim 100 GeV/m$) can be three orders of magnitude greater than that obtained in the conventional radio-frequency linacs ($\sim 100 MeV/m$).

In addition to the wake field generation, other effects may occur in the relativistic laser plasma interactions such as the *relativistic self-focusing*. At high laser intensities, the electron mass increases due to the relativistic effects and the plasma frequency $\widetilde{\omega}_{pe} = \omega_{pe}/\gamma^{1/2} = \sqrt{4\pi n_0 e^2/(\gamma m_e)}$ varies with the laser intensity. Here n_0 is the unperturbed electron density and $\omega_{pe} = (4\pi n_0 e^2/m_e)^{1/2}$ is the plasma frequency without relativistic effects. In unmagnetized plasmas, the dispersion relation for an electromagnetic wave is,

$$\omega^2 = k^2c^2 + \widetilde{\omega}_{pe}^2 \tag{1.7}$$

As a result, the index of refraction $\eta \equiv ck/\omega = \left(1 - \widetilde{\omega}_{pe}^2/\omega^2\right)^{1/2}$ increases at higher laser intensity regions. Since the phase velocity of the wave is determined by $v_\phi \equiv \omega/k = c/\eta$, the variation of phase speed will distort the wave front. For a Gaussian type laser pulse, this effect results in a self-focusing of the laser pulse as shown in Fig. 1.4. Meanwhile, since the ponderomotive force tends to expel the electrons forwards and radially to the lower intensity areas, it leads to a decreasing of electron density and an increasing of refractive index on the axis. This effect further enhances the self-focusing. The threshold power P_c for the relativistic self-focusing can be found when the focus effects are balanced by the diffractive spreading, which is $P_c \approx 17.4\,\omega^2/\omega_{pe}^2\,GW$. [15, 16] When the laser power $P \gg P_c$, relativistic focusing overcomes the diffractive effects and pulse filamentation may occur. Depending on the laser pulse and plasma conditions, the whole laser pulse can be self-focused or it may split into several filaments and each of them undergoes self-focusing. [17].

One of the immediate applications of the refractive index variation is the *optical guiding* in plasmas. A laser can be guided if the refractive index has a maximum on the axis or $\partial\eta/\partial r < 0$. Such kind of refractive index profile can be achieved by modifying the relativistic factor γ, e.g. through the relativistic self-focusing, or the density profile, e.g. through the preformed density channel or self-channeling. [12,18,19] Furthermore, the dependence of plasma frequency on the relativistic factor makes it possible for the ultra-intense laser to propagate into the over-dense plasmas. This is usually referred as the *relativistic transparency*. It can be seen from Eq. (1.7) that a laser can penetrate into the plasmas only when its frequency is larger than the plasmas frequency. Hence, for ultra-intense laser pulse, the cutoff frequency of the electromagnetic wave decreases as the laser intensity increases and relativistic transparency happens when $\omega > \widetilde{\omega}_{pe}$.

1.1.2 Magnetic field in laser plasma interactions

During the intense laser plasmas interactions, not only the electric fields but also the various configurations of magnetic fields can be generated spontaneously. Simulations [20,21] and experiments [22] have shown that a poloidal magnetic field is generated by the current of relativistic electrons driven by the laser radiation in the laser propagation direction. These magnetic fields are quasi-static with amplitude the same order of the laser magnetic field and thus can affect the laser propagation, e.g. they can lead to a magnetic focusing in addition to the usual ponderomotive and self-focusing mechanisms. [23, 24] Furthermore, an axial magnetic field may be induced by a circularly polarized laser via the inverse Faraday effects [25] and a toroidal magnetic field is generated through the thermoelectric effects when there is a temperature gradient orthogonal to a density gradient. In these cases, magnetic field with strength up to kilotesla can be driven. Hence, plasmas are always magnetized during the laser plasma interactions. In additional to the self-generated magnetic field, recently kilotesla external magnetic field has been demonstrated in a laboratory by a high power laser irradiated to a capacitor-coil target. [26] By applying such kind of strong and shaped magnetic fields, new frontiers in plasmas physics, solar physics, material science, etc. can be explored.

The introduction of various configurations of magnetic field can affect the propagation of the laser pulse and the transport of the particles [27,28], which can benefit many potential applications. For instance, in laser fast ignition scheme, the collimation of the relativistic electron beam by an axial magnetic field has shown an increase in the coupling efficiency between the laser and fusion core. [29, 30, 31]. Also terahertz radiation [32,33,34] or harmonic radiation [35,36,37] can be generated when longitudinal or transverse magnetic field is imposed. In addition, it is proved that the magnetic field can provide some other mechanisms for particle acceleration. [38, 39, 40] Hence, the study of ultra-intense laser plasma interactions with self-consistently generated or externally imposed strong magnetic fields is of much importance.

Despite the various configurations of the magnetic field, throughout this thesis we only consider the case where the external magnetic field is applied along the laser propagation direction. Such kind of magnetic field is of special importance in laser fast ignition, electron and ion acceleration, terahertz radiation, etc.

1.1.3 Ultra-intense laser propagation in magnetized plasmas

During the ultra-intense laser plasma interactions, the plasma parameters are altered by the wave. Meanwhile, the wave fields are also modified by the plasmas. Hence, the propagation of an intense electromagnetic wave should be studied consistently with all the dynamics including the wake field generation, self-focusing, pulse modulation, magnetic field generation, etc. Due to the complexity of the

problem, the theory on the evolution of an electromagnetic wave in a plasma is always studied by various simplifications, e.g. the quasi-static approximation or the weakly relativistic approximation. On the other hand, for intense laser pulse, the superposition principle to the waves is no longer applicable, say, the linearly polarized laser cannot be described as a linear combination of right and left hand circularly polarized waves, since the there is no way of generating the oscillations in the propagation direction by the circularly polarized waves alone. Hence, linearly polarized waves are especially complex compared to the circularly polarized case where the simplification of no harmonic contents cannot be made. Thus, particle-in-cell (PIC) simulation becomes the very useful and important tool for understanding the various dynamics during the ultra-intense laser plasma interactions.

In magnetized plasmas, the laser propagation modes strongly depend on the plasma densities, the magnetic field as well as the intensity and polarization of the laser pulse, e.g. if the magnetic field is along the wave propagation direction, the propagation modes can be the high frequency left and right hand circularly polarized waves (LCP and RCP), the electron cyclotron wave (Whistler mode), the Alfven waves, etc. When the magnetic field varies, these propagation modes can co-exist and convert to each other, which leads to abundant laser magnetized plasma physics. One of the important phenomena of the laser propagation is the *soliton formation*. [41, 42, 43] The solitons are finite size, self-trapped electromagnetic waves which consist of synchronously oscillating electric and magnetic fields plus a steady electrostatic field arising from the ponderomotive force of the oscillating fields. In laser plasma interactions, the solitons are usually generated in the wake of the laser pulse with strong plasma depletion. Inside the solitons, the dispersion effects are balanced by the nonlinearities due to the density redistribution and relativistic effects. Solitons in unmagnetized plasma have been observed in experiments by a proton imaging technique [41] as well as in PIC simulations [42, 43], where people find up to 30~40% of the laser energy can convert into the soliton or soliton-like structures. Hence, the soliton generation which represents an effective energy transfer process deserves special attentions.

1.2 Solitons in laser plasmas interactions

The solitary wave or soliton, first observed by the Scottish engineer John Scott Russell in 1834, is a localized wave which persists its shape and velocity during the propagation and interaction with other solitons. At that time, Russel's observations contradicted the shallow water theory of Airy (1845) in that the solitons did not change their form. Later, Joseph Boussinesq (1871) and Lord Rayleigh (1876) showed that this was due to the cancellation between the dispersion and nonlinearity. In 1895, Korteweg and de Vries [44] developed the famous Korteweg-de Vries (KdV) equation describing the propagation of waves

(a) (b)

Fig. 1.5 (a) A morning glory cloud formation between Burketwon and Normanton, Australia [image credit: Wikipedia]; The morning glory cloud is a rare atmospheric solitary wave. (b) Recreation of a solitary wave on the Scott Russell Aqueduct on the Union Canal. [Photograph courtesy of Heriot-Watt University [47]]

on shallow water surfaces, which had the soliton solution and periodic cnoidal solutions. On the other hand, E. Fermi, J. R. Pasta and S. M. Ulam (FPU) [45] found a quasi-periodic behavior instead of the ergodic behavior when they were simulating the vibrating string in 1955. N. Zabusky and M. Kruskal [46] argued that it was the fact that soliton solutions can pass through one another without affecting the shapes that contributed to the quasi-periodicity of the waves in the FPU experiment. Soliton are solutions to many famous equations including the KdV equation, the nonlinear Schrodinger (NLS) equation, the coupled NLS equations and the sine-Gordon equation. Although solitons were originally discovered in water waves and lattice dynamics, they also appear in many other systems, such as the optical fibers, the magnets, the meteorology and the plasmas, e.g. see Fig. 1.5.

1.2.1 Bright and dark solitons

Generally, solitons evolve from the nonlinear change in the refractive index of the plasmas induced by the laser intensity distribution and electron density perturbation. When the nonlinear effects compensate the dispersion (in the case of temporal solitons) or diffraction (in the case of spatial solitons) effects, the pulse can propagate without change in shape. In this thesis, we mainly focus on the two different types of solitons in the plasmas: the *bright soliton* and the *dark soliton*. The bright and dark solitons are well-known in optics, where bright solitons are generated in optical fibers with negative or anomalous group velocity dispersion and dark solitons are formed in optical fibers with positive or normal group velocity dispersion. [48] The first observation of bright optical solitons was in 1980 by Mollenauer et al. [49] whereas by 1987 dark

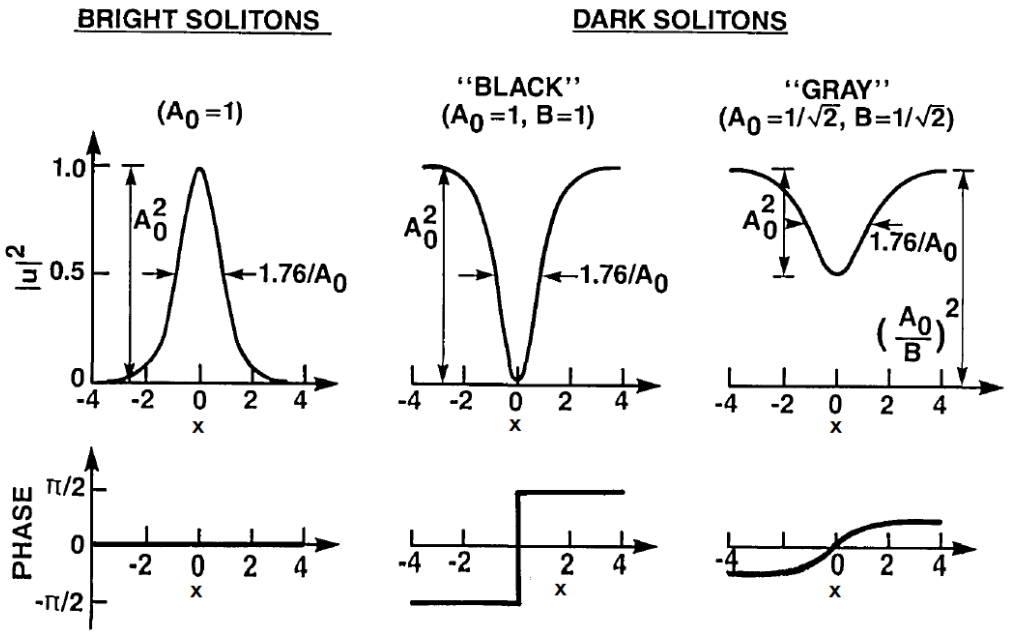

Fig. 1.6. Intensity and phase as function of normalized coordinates x for bright and dark solitons. [adapted from W. J. Tomlinson et al. [51]]

solitons were formed in laboratory experiments [50]. In the moving frame with the soliton, the bright soliton envelop can be written as, [51]

$$u(x) = A_0 \operatorname{sech}(x) \tag{1.8}$$

Here A_0 is the soliton amplitude and $\operatorname{sech} x$ is the hyperbolic secant function. Hence, bright soliton describes a localized wave with intensity maximum at the center and zero at the infinity (see Fig. 1.6). For the dark soliton, it has the form,

$$\begin{cases} u(x) = A_0[B^{-2} - \operatorname{sech}^2(x)]^{1/2} \exp[i\varphi(x)] \\ \varphi(x) = \sin^{-1}\left\{\dfrac{B \tanh(x)}{[1 - B^2 \operatorname{sech}^2(x)]^{1/2}}\right\} \end{cases} \tag{1.9}$$

Here $|B| \leq 1$ is a parameter represents the darkness and $\tanh x$ is the hyperbolic tangent function. In the limiting case of $B = \pm 1$, Eq. (1.9) is reduced to $u(x) = \pm A_0 \tanh x$ which is referred as the fundamental dark soliton or black soliton. For $|B| < 1$, the minimum intensity does not drop to zero and it is called as the grey soliton. Hence, dark solitons appear as holes of the intensity on a continuous wave background. One of the major differences between the bright and dark solitons is their phase dependence as shown in Fig. 1.6. The bright solitons are symmetric with a constant phase across the entire pulse, while the dark solitons undergo a phase jump $2 \sin^{-1} B$. For the black soliton, the phase jump is π.

1.2.1 Researches on solitons in unmagnetized plasmas

The solitons in laser unmagnetized plasma interactions have been studied by many authors in experiments and simulations. In the uniform plasmas, the soliton velocity is much smaller than the group velocity of the laser and in fact it is almost zero. [42] The typical size of the soliton is of the order of the collisionless electron skin depth $\sim c/\omega_p$. Eventually, the soliton decays due to the interaction with fast electrons. In non-uniform plasmas, the soliton can propagate to the low density direction with an acceleration proportional to the gradient of the plasma density. [52] When the soliton approaches the plasma-vacuum interface, it will radiate away its energy in the form of low frequency electromagnetic waves due to the non-adiabatic interaction with the plasma boundary, resulting in a burst of electromagnetic radiation, which makes it possible for the detection of soliton generation and various applications. [53] Since the time of soliton generation is much shorter than the ion's response time, ions can be assumed to be at rest during approximately $2\pi/\omega_{pi}$ time scale. Here $\omega_{pi} = \sqrt{4\pi n_o e^2/m_i}$ is the ion plasma frequency and m_i is the ion mass. At later time, the ponderomotive force starts to dig a hole in the ion density and the parameters of the soliton change. Such kind of slowly expanding solitons are referred as the post-soliton. [43, 53]. We mention that all the solitons observed in the simulations are of bright type.

The theory of relativistic electromagnetic solitons in a cold plasma was first studied by Kozlov et al [54] in an envelope approximation. They proved the existence of small amplitude solitons under quasi-neutral approximation and found that relativistic amplitude solitons only existed when the charge separation was essential and the large amplitude solitons could have a discrete velocity spectrum. Their work has been extended by Kaw et al [55], Poornakala et al [56] and Farina et al [57, 58, 59] where ion's motion effects are investigated and different types of solitons are demonstrated. In the limit of quasi-neutral approximation, bright solitons exist when the soliton group velocity V exceeds a threshold and below which dark solitons occur. Collisionless electromagnetic shock waves are also found at critical velocities. Large amplitude solitons with several humps in the vector potential profile and one hump in the scalar potential profile are also observed and the soliton spectrum varies with different number of humps. Solitons can break up at certain velocities and the breaking of solitons provides an additional mechanism for particle acceleration, e.g. the estimated ion energy could reach the order of 70Mev [58].The soliton in warm plasma case was treated by Lontano et al [60] in a quasi-neutral approximation and Poornakala et al [61] in a weakly relativistic approximation. It was found that temperature effects played a crucial role when the soliton group velocity was small, e.g. comparable to the thermal speed of the particles. Specifically, the finite temperature effects made it possible for the existence of the non-drifting solitons and this kind of soliton was prohibited in cold plasma if ion's motion was taken into account. In the absence of ions, the exact solution for non-drifting solitons in cold plasmas was given by Esirkepov et al [62]. Sanchez-Arriaga et al. [63] studied the

parametric domain for the dark solitons and also their stabilities. A review can be found in Ref 59, where different types of solitons and their properties under different soliton velocities are shown. Note that all of these works mentioned above are constrained to the relation $Vv_\phi = c^2$, where $v_\phi \equiv \omega/k$ is the soliton phase velocity and ω, k are the soliton frequency and wavenumber. Sanchez-Arriaga et al [64] first consider the case when this relation breaks up and find that a phase modulation exists.

The stabilities of the solitons in unmagnetized plasmas were also studied in the past. [65, 66, 67] It was found that, in 1D geometry, single hump bright solitons without ion's motion were stable and multi-hump bright soliton could break up due to the forward Raman scattering. [68, 69] In 2D simulations, all solitons suffered from the transverse instabilities. [70]

1.2.2 Researches on solitons in magnetized plasmas

Compared with the systematic and abundant research results in unmagnetized plasmas, the studies of solitons in magnetized plasma are much less and insufficient. Pioneering works were mainly on the nonlinear propagation of electromagnetic waves parallel to the magnetic field in plasmas. Karpman et al. [71, 72] derived the nonlinear Schrodinger equation for the envelope of a high frequency wave modulated by the effects of low frequency perturbations. The relativistic nonlinearities and parallel electron flow contributions were later incorporated by Berezhiani et al. and Shukla et al. [73,74]. Hasegawa [75] developed the coupling equations governing the electron cyclotron wave by the reductive perturbation method. Shukla et al. [76] studied the nonlinear coupling of Whistler wave with ion cyclotron oscillations. In general, a pair of nonlinear equations coupling the wave amplitude and electrostatic density perturbations can be derived from these models by assuming a slowly-varying envelop approximation. As a result, a stationary soliton solution can be obtained. Rao et al. [77] adopted this method to discuss the parameter domain for large amplitude solitons in cold plasmas, however they neglected the longitudinal momentum of the electrons and the ion current density effects. The standing bright soliton solution without ion's motion effects in cold plasmas was considered by Farina et al [78]. Different from the above researchers, Borhanian et al [79] employed a multi-scale perturbation method to solve the Maxwell-fluid equations in the weakly relativistic limit, where they also obtained a nonlinear Schrodinger-type equation to govern the soliton vector potential.

1.3 Outline of the thesis

As discussed in the previous sections, the ultra-intense laser plasma interactions in the presence of strong parallel magnetic field are of great importance in many applications including the magnetically assisted fast

ignition, the wake field acceleration, terahertz radiation, etc. In all of these applications, the laser pulse needs to propagate a long distance in the under-dense plasmas. However, the details about the propagation modes, specifically the soliton formations in magnetized plasmas still remain unclear. Since a substantial part of the laser energy can be transformed into the solitons before it can interact with the target, it is very important and necessary to figure out the underlying physics of the solitons.

In this thesis, the effects of strong magnetic field on the laser plasma interactions, specifically on the various laser propagation modes and soliton formations are studied numerically through a PIC simulation and analytically by solving the soliton equations. The uniform external magnetic field is applied along the laser propagation direction. The outline of the thesis is as follows,

- In chapter 2, we first introduce the single particle orbit inside the relativistic linearly and circularly polarized laser field in the presence of strong parallel magnetic field. Then the relativistic dispersion relation for the electromagnetic waves is discussed. Specifically, the shrink and disappearance of the Whistler mode under the ultra-relativistic regime is investigated.
- In chapter 3, the simulation results performed by the extended particle based integrated code (EPIC3D) are shown. We mainly focus on the laser heating efficiency and soliton formation with different magnetic fields and laser intensities and polarizations. The linear propagation modes, namely the right hand circularly polarized wave (RCP), the left hand circularly polarized wave (LCP) and the Whistler wave are analyzed theoretically in the inhomogeneous plasmas areas. The soliton mechanism and properties, e.g. the stabilities and the position dependence are studied.
- In chapter 4, the coupled soliton equations are derived in the framework of relativistic warm fluid model. Different dispersion relations for bright and dark solitons are assumed from the boundary conditions and the Hamiltonian of the system is found. The theory of dynamical systems as well as the concepts of fixed point, bifurcation, homoclinic and heteroclinic orbit and manifold are interpreted at the end of the chapter.
- In chapter 5, the bright soliton generation in magnetized plasmas is systematically studied based on the coupled soliton equations. The parametric domain of magnetic field and soliton frequency for the existence of bright solitons is identified in cold and warm plasmas, respectively. Ion's effects on this parametric domain are investigated and the small amplitude soliton solution is obtained under the quasi-neutral limit. The numerical methods, namely the shooting and rational spectral methods, are presented to solve the soliton equations and compute the manifolds. Based on the numerical calculations, the dependences of soliton amplitude and density on the magnetic field, soliton frequency, temperature and ion's motion are investigated.

- In chapter 6, the dark soliton formation in magnetized plasmas is presented. The parametric domain of the magnetic field, soliton frequency and wavenumber for the existence of dark solitons is identified in both and warm plasmas. Specifically, the temperature effects on the single hump and multi-hump dark solitons are investigated.
- In chapter 7, the meaning of our research is pointed. The main results are concluded and several open problems are proposed for the extension of this work.
- In the appendix, the validity of the Hamiltonian of the system and the existence conditions of the additional fixed points for the bright and dark solitons are shown. We also benchmark the shooting method with the rational spectral scheme to confirm their correctness.

2. Single particle orbit and dispersion relation in magnetized plasmas

The introduction of magnetic field can affect the charged particle's motion and thus the plasma's response to electromagnetic perturbations. In principle, the theory of laser plasma interaction should simultaneously treat the interactions between the field and particles self-consistently. However, due to the complexity of this problem, some simplifications should be made. One of the simplifications commonly used is to neglect the forces among the particles, and the reaction of the particles on the field, e.g. the particle's radiation, which leads to the single particle orbit theory. Since the collective effects of the plasma are ignored, the single particle orbit theory can only be used to the weakly coupled plasmas in short time scale. However, the charged particle's motion is the basis of understanding the various physical processes in plasmas and it is also very important to the physics of particle accelerator, electron optical imaging and so on. In this chapter we first introduce the single particle motion inside the relativistic laser field in the presence of parallel magnetic field. The Lagrangian mechanics is used and the system is completely integrable. Then the linear dispersion relation in strongly magnetized plasmas with the inclusion of relativistic effects is discussed in the framework of fluid model.

2.1 Single particle motion in relativistic laser field

The single particle orbit inside the relativistic laser field without magnetic field is well known. [7] For linearly polarized laser, the particle has the "8-figure" structure in the average rest frame, while for circularly polarized laser, the orbit is a circle. In the presence of magnetic field, the particle's motion will be changed.

2.1.1 Linearly polarized laser

Considering a linearly polarized laser represented by $\boldsymbol{E} = E_L \cos(k_0 z - \omega_0 t)\, \hat{\boldsymbol{e}}_x$, propagates in an uniform cold plasma with density n_0 in the presence of a constant magnetic field $\boldsymbol{B}_0$ applied parallel to the direction of the propagation z, where E_L, k_0, ω_0 are the amplitude, wavenumber and frequency of the laser field respectively. The corresponding vector and scalar potentials can be chosen as $\boldsymbol{A} = (cE_L/\omega_0)\sin(k_0 z -$

$\omega_0 t)\,\hat{\boldsymbol{e}}_x + B_0 x\hat{\boldsymbol{e}}_y$ and $\phi = 0$. Notice that the electric and magnetic fields can be calculated by $\boldsymbol{E} = -(1/c)\,\partial\boldsymbol{A}/\partial t - \nabla\phi$ and $\boldsymbol{B} = \nabla \times \boldsymbol{A}$. The Lagrangian of the particle in this field is,

$$\begin{aligned} L(\boldsymbol{r}, \boldsymbol{v}, t) &= -mc^2\sqrt{1 - \frac{v^2}{c^2}} + \frac{q}{c}\boldsymbol{A}\cdot\boldsymbol{v} - q\phi \\ &= -mc^2\sqrt{1 - \frac{v^2}{c^2}} + \frac{qE_L v_x}{\omega_0}\sin(k_0 z - \omega_0 t) + \frac{qv_y}{c}B_0 x \end{aligned} \tag{2.1}$$

Here q, m, $\boldsymbol{v}$, γ, c, are the particle charge, mass, velocity, relativistic factor and speed of light. Note that the particle charge is defined with sign, e.g. for electrons $q = -e$. Since the Lagrangian doesn't depend on y and it only depends on the combination of $\eta = k_0 z - \omega_0 t = k_0(z - ct)$, we have,

$$\frac{\partial L}{\partial y} = 0 = \frac{dP_y}{dt}; \qquad \frac{\partial L}{\partial t} + c\frac{\partial L}{\partial z} = 0 = -\frac{dH}{dt} + c\frac{dP_z}{dt}$$

Here $\boldsymbol{P} = \mathbf{p} + (q/c)\boldsymbol{A}$ is the canonical momentum and $\boldsymbol{p} = \gamma m\boldsymbol{v}$ is the kinetic momentum with $\gamma = (1 - v^2/c^2)^{-1/2}$ and $H = \sqrt{m^2c^4 + c^2p^2}$ is the Hamiltonian. In deriving the above equations we have used the relation $\partial L/\partial t = -\,dH/dt$ since the Hamiltonian H does not contain t explicitly. The above equations give two integrals of motion,

$$p_y + \frac{q}{c}B_0 x = c_1 \tag{2.2}$$

$$H - cP_z = \sqrt{m^2c^4 + c^2p^2} - cp_z = c_2 \tag{2.3}$$

c_1 and c_2 are two constants depending on the initial conditions. Meanwhile, the equations of motion in the x and z directions are,

$$\frac{dP_x}{dt} = \frac{d}{dt}\left(p_x + \frac{qE_L}{\omega_0}\sin\eta\right) = \frac{\partial L}{\partial x} = \frac{qv_y}{c}B_0 \tag{2.4}$$

$$\frac{dP_z}{dt} = \frac{dp_z}{dt} = \frac{\partial L}{\partial z} = \frac{qE_L v_x}{c}\cos\eta \tag{2.5}$$

Using ω_0^{-1}, k_0^{-1}, mc and mc^2 to normalize the time, space, momentum and energy, Eqs. (2.2) – (2.5) become,

$$\begin{aligned} &p_y + bx = c_1; && \gamma - p_z = c_2; \\ &\frac{dp_x}{dt} = -a\cos\eta\frac{d\eta}{dt} + \frac{p_y}{\gamma}b; && \frac{dp_z}{dt} = \frac{ap_x}{\gamma}\cos\eta\,. \end{aligned} \tag{2.6}$$

Here $a = qE_L/(m\omega_0 c)$ and $b = qB_0/(m\omega_0 c)$. Note that we have the identify $d\eta/dt = (p_z - \gamma)/\gamma = -c_2/\gamma$. Hence, Eq. (2.6) is reduced to the forced oscillation equation,

$$\frac{d^2 p_x}{d\eta^2} + \frac{b^2}{c_2^2} p_x = a \sin\eta \tag{2.7}$$

Depending on different values of b/c_2, this equation may have resonance and non-resonance solutions. In the next, we assume the particle is initially located at the origin and at rest, e.g. $c_1 = 0$ and $c_2 = 1$.

a) Non-resonance solution

If $b \neq \pm 1$, we can have the non-resonance solution,

$$p_x = \frac{a}{b^2 - 1}\sin\eta + c_3 \sin b\eta + c_4 \cos b\eta$$

Here c_3, c_4 are undetermined factors and they can be determined by the initial condition, $p_x = 0$ and

$$\left.\frac{dp_x}{d\eta}\right|_{\eta=0} = -a\cos\eta - b p_y\big|_{\eta=0} = -a = \frac{a}{b^2 - 1} + c_3 b$$

Hence $c_4 = 0,\ c_3 = -ab/(b^2 - 1)$. Then the particle's momenta are,

$$\begin{cases} p_x = \dfrac{a}{b^2 - 1}(\sin\eta - b\sin b\eta); \qquad p_y = -\dfrac{ab}{b^2 - 1}(\cos\eta - \cos b\eta); \\ p_z = \dfrac{1}{2}\left(\dfrac{a}{b^2 - 1}\right)^2 [sin^2\eta + b^2 cos^2\eta + b^2 - 2b(\sin\eta \sin b\eta + b\cos\eta\cos b\eta)]. \end{cases} \tag{2.8}$$

The momentum in *x*-*y* plane has two frequencies: the laser frequency and the cyclotron frequency. The particle's orbit can be integrated directly using the relation $\boldsymbol{p} = \gamma\, d\boldsymbol{r}/dt = -d\boldsymbol{r}/d\eta$ to get,

$$\begin{cases} x = \dfrac{a}{b^2 - 1}(\cos\eta - \cos b\eta); \qquad y = \dfrac{a}{b^2 - 1}(b\sin\eta - \sin b\eta); \\ z = -\dfrac{1}{2}\left(\dfrac{a}{b^2 - 1}\right)^2 \left\{\dfrac{\eta}{2}(1 + 3b^2) + \dfrac{b^2 - 1}{4}\sin 2\eta - b\left[\dfrac{b+1}{b-1}\sin(b-1)\eta + \dfrac{b-1}{b+1}\sin(b+1)\eta\right]\right\}. \end{cases}$$

(2.9)

Obviously, the motion is no longer planar. If $b = 0$, Eqs. (2.8) and (2.9) reduce to the zero magnetic field case, which describes an "8-figure" motion in the average at rest frame,

$$\begin{cases} p_x = -a\sin\eta\,; \qquad p_y = 0; \qquad p_z = \dfrac{1}{2}a^2 sin^2\eta; \\ x = -a(\cos\eta - 1); \qquad y = 0; \qquad z = -\dfrac{1}{4}a^2\left(\eta - \dfrac{1}{2}\sin 2\eta\right). \end{cases} \tag{2.10}$$

b) Resonance solution

The resonance case happens when $b = \pm 1$ or the cyclotron frequency equals to the laser frequency. In

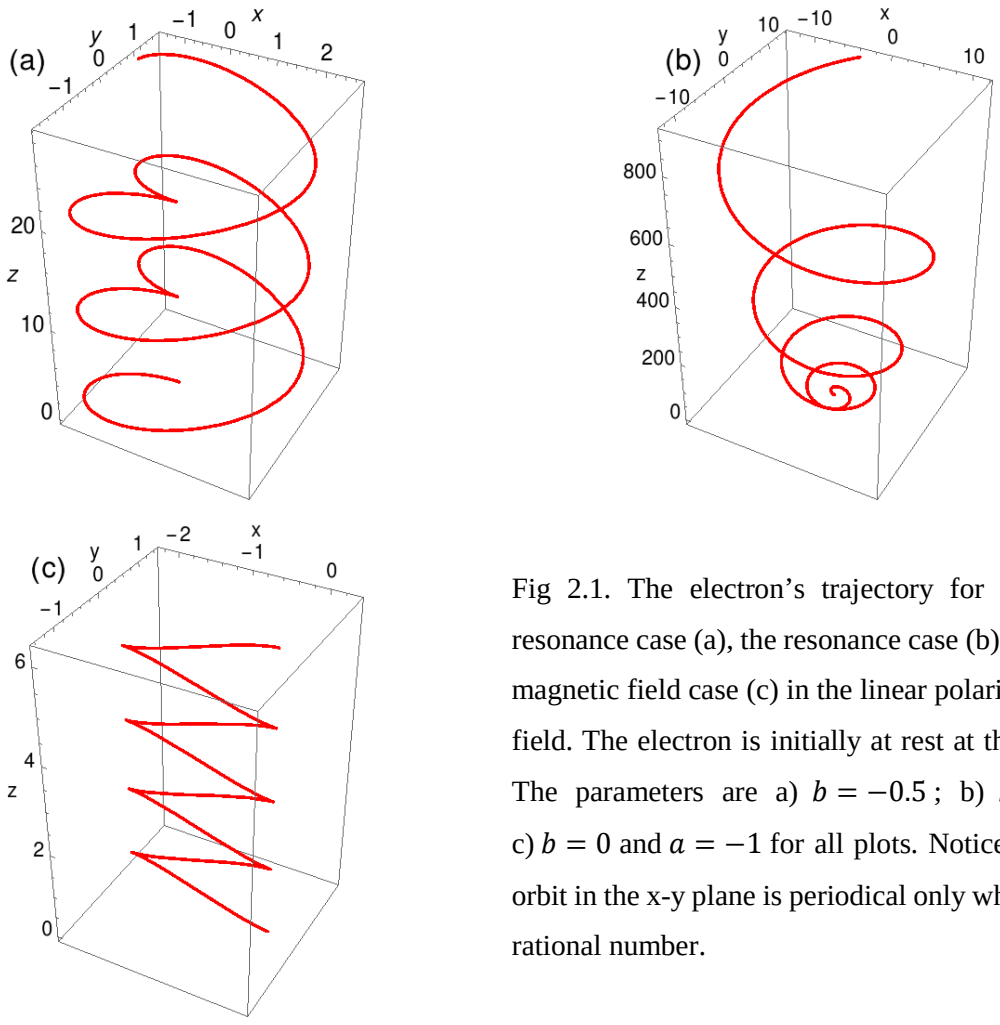

Fig 2.1. The electron's trajectory for the non-resonance case (a), the resonance case (b) and zero magnetic field case (c) in the linear polarized laser field. The electron is initially at rest at the origin. The parameters are a) $b=-0.5$; b) $b=-1$; c) $b=0$ and $a=-1$ for all plots. Notice that the orbit in the x-y plane is periodical only when b is a rational number.

this case, the particle will get energy from the laser continuously. The momenta and orbit can be calculated in the limit of $b \to \pm 1$ of Eqs. (2.8) and (2.9),

$$\begin{cases} p_x = -\dfrac{a}{2}(\eta\cos\eta + \sin\eta); & p_y = -\dfrac{a}{2}\eta\sin\eta\,; & p_z = \dfrac{a^2}{8}(\eta^2 + \sin^2\eta + \eta\sin 2\eta); \\ x = \dfrac{a}{2}\eta\sin\eta\,; & y = \dfrac{a}{2}(\sin\eta - \eta\cos\eta); & z = -\dfrac{a^2}{8}\left(\dfrac{\eta^3}{3} + \dfrac{\eta}{2} - \dfrac{\eta\cos 2\eta}{2}\right). \end{cases} \tag{2.11}$$

The comparison of particle's orbit for the resonance and non-resonance as well as the zero magnetic field cases are shown in Fig 2.1. It can be seen that the usual "8-figure" plane motion (Fig 2.1(c)) in unmagnetized case has now changed to 3 dimensional. Notice that the particle's orbit in the *x-y* plane is closed or periodical only when *b* is a rational number.

2.1.2 Circularly polarized laser

A similar calculation can be made for the circularly polarized laser. Here we take the right hand circular polarized laser as an example. In this case, the vector potential becomes $\boldsymbol{A} = (cE_L/\omega_0)\sin\eta\,\hat{\boldsymbol{e}}_x + [B_0 x - (cE_L/\omega_0)\cos\eta]\hat{\boldsymbol{e}}_y$ and the scalar potential ϕ remains zero. The Lagrangian is

$$L(\boldsymbol{r},\boldsymbol{v},t) = -mc^2\sqrt{1-v^2/c^2} + \frac{qE_L v_x}{\omega_0}\sin\eta + \frac{qv_y}{c}\left(B_0 x - \frac{cE_L}{\omega_0}\cos\eta\right). \tag{2.12}$$

There are also two integrals of motion similar to Eqs. (2.2) and (2.3), and the equations of motion become,

$$\begin{aligned} c_2\frac{dp_y}{d\eta} &= bp_x - ac_2\sin\eta\,; \qquad & \gamma - p_z &= c_2; \\ c_2\frac{dp_x}{d\eta} &= -bp_y - ac_2\cos\eta\,; \qquad & c_2\frac{dp_z}{d\eta} &= -a\left(p_x\cos\eta + p_y\sin\eta\right). \end{aligned} \tag{2.13}$$

Then the forced oscillation equation for p_x is,

$$\frac{d^2p_x}{d\eta^2} + \frac{b^2}{c_2^2}p_x = a\left(1+\frac{b}{c_2}\right)\sin\eta. \tag{2.14}$$

For the left hand circularly polarized laser, the sign of the second term in the parentheses of the right hand side of Eq. (2.14) is negative. Again we assume the particle is initially at rest at the origin, then $c_2 = 1$.

a) Non-resonance solution

For the non-resonance solution, $b \neq 1$. The particle's momenta and orbit are,

$$\begin{cases} p_x = \dfrac{a}{b-1}(\sin\eta - \sin b\eta); & p_y = -\dfrac{a}{b-1}(\cos\eta - \cos b\eta); \quad p_z = \left(\dfrac{a}{b-1}\right)^2[1-\cos(b-1)\eta]; \\ x = \dfrac{a}{b-1}\left(\cos\eta - \dfrac{1}{b}\cos b\eta\right) - \dfrac{a}{b}; & y = \dfrac{a}{b-1}\left(\sin\eta - \dfrac{1}{b}\sin b\eta\right); \quad z = -\left(\dfrac{a}{b-1}\right)^2\left[\eta - \dfrac{\sin(b-1)\eta}{b-1}\right]. \end{cases} \tag{2.15}$$

For the zero magnetic field case $b = 0$, Eq. (2.15) is reduced to,

$$\begin{cases} p_x = -a\sin\eta\,; & p_y = a(\cos\eta - 1); & p_z = a^2(1-\cos\eta); \\ x = -a\cos\eta\,; & y = -a(\cos\eta - \eta); & z = -a^2(\eta - \sin\eta). \end{cases} \tag{2.16}$$

It describes a circle with moving center at $(0, a\eta)$ in the x-y plane. Interestingly, a special case happens when $b = -1$,

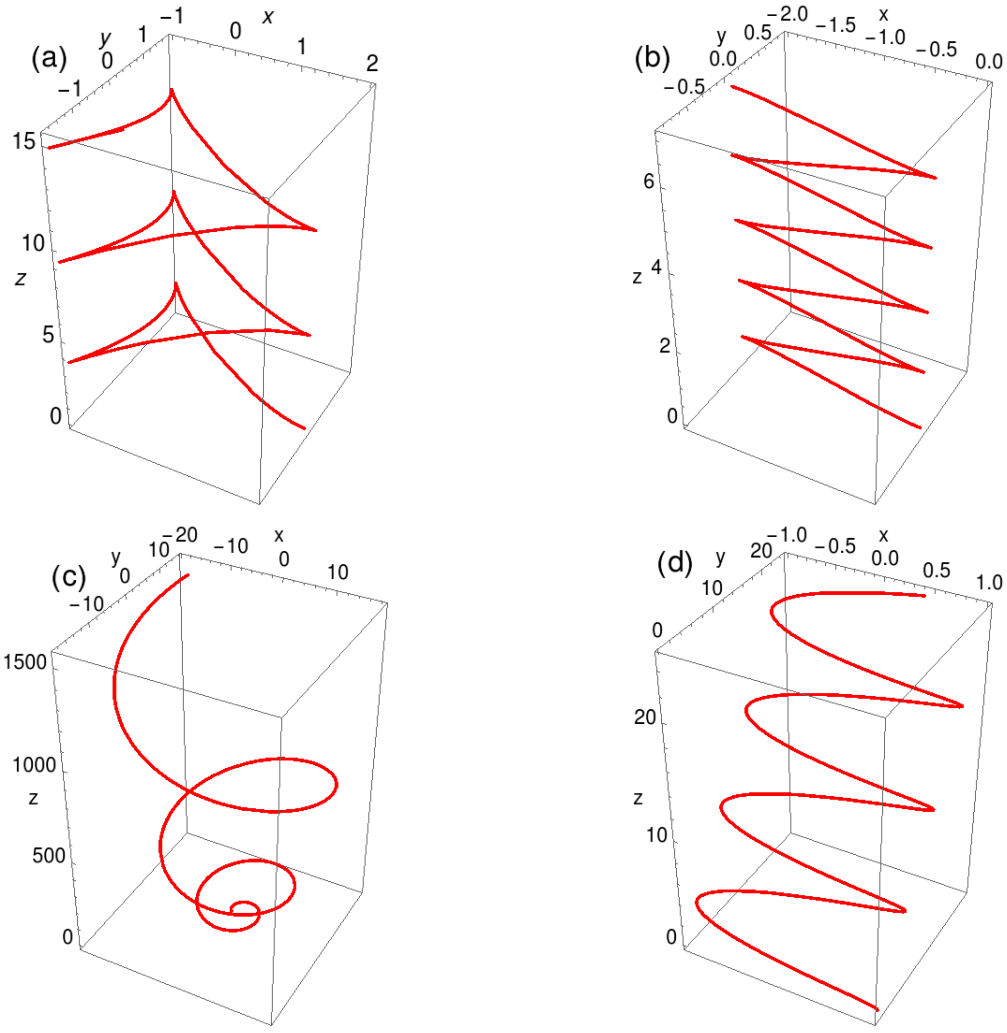

Fig 2.2. The electron's trajectory for the non-resonance case (a), the special case (b), the resonance case (c) and zero magnetic field case (d) in the right hand circularly polarized laser field. The electron is initially at rest at the origin. The parameters are a) $b = -0.5$; b) $b = -1$; c) $b = 1$; (d) $b = 0$ and $a = -1$ for all plots.

$$\begin{cases} p_x = -a\sin\eta\,; & p_y = 0; & p_z = \dfrac{a^2}{4}(1-\cos 2\eta); \\ x = a(1-\cos\eta); & y = 0; & z = -\dfrac{a^2}{4}\left(\eta - \dfrac{1}{2}\sin 2\eta\right). \end{cases} \tag{2.17}$$

Eq. (2.17) is exactly the same as (2.10). Hence, in the average at rest frame, the motion is the "8-figure" structure which is same as the linearly polarized laser without magnetic field. In this case, the circularly polarization effects are canceled by the cyclotron effects of the particles.

b) Resonance solution

If $b = 1$, resonance happens and the particle's momenta and orbit are,

$$\begin{cases} p_x = -a\eta\cos\eta\,; & p_y = -a\eta\sin\eta\,; & p_z = a^2\eta^2/2\,; \\ x = a(\eta\sin\eta+\cos\eta)-a; & \mathrm{y} = -a(\eta\cos\eta-\sin\eta); & \mathrm{z} = -\frac{1}{6}a^2\eta^3. \end{cases} \tag{2.18}$$

In Fig 2.2, we show the electron's orbits for various magnetic fields in the right hand circularly polarized laser field. The figures (a), (b), (c) and (d) correspond to the general case, the special case, the resonance case and the zero magnetic field case, respectively.

One of the applications of these exact expressions for the particle's orbit is to calculate the radiation from this relativistic motion, e.g. the scattering of a laser pulse by the electrons. Such radiation becomes non-ignorable when the laser intensity is ultra-high, say, $I > 10^{23}W/cm^2$.

2.2 Electromagnetic waves in magnetized plasmas

When there is some perturbations in the plasmas, the electromagnetic field can propagate away in the form of waves. In this section, we introduce the waves propagating parallel to the constant external magnetic field in the linear regime.

2.2.1 Dispersion relation

The field in the plasmas should satisfy the Maxwell equations and the fluid equations, which are,

$$\frac{\partial n_s}{\partial t} + \nabla\cdot(n_s\boldsymbol{v_s}) = 0; \tag{2.19a}$$

$$\frac{\partial \boldsymbol{p_s}}{\partial t} + \boldsymbol{v_s}\cdot\nabla\boldsymbol{p_s} = q_s\left(\boldsymbol{E}+\frac{1}{c}\boldsymbol{v_s}\times\boldsymbol{B}\right); \tag{2.19b}$$

$$\nabla(\nabla\cdot\boldsymbol{E}) - \nabla^2\boldsymbol{E} + \frac{1}{c^2}\frac{\partial^2\boldsymbol{E}}{\partial t^2} = -\frac{4\pi}{c^2}\frac{\partial\boldsymbol{J}}{\partial t}; \tag{2.19c}$$

$$\boldsymbol{J} = \sum\nolimits_s n_s q_s \frac{\boldsymbol{p_s}}{\gamma_s m_s}. \tag{2.19d}$$

Here the sum $\sum$ stands for a summation over particle species s. In 1D case $\nabla \equiv \hat{\boldsymbol{e}}_z(\partial/\partial z)$. The density, velocity, relativistic factor, momentum, charge, mass are denoted as $n_s, \boldsymbol{v_s}, \gamma_s, \boldsymbol{p_s}, q_s, m_s$ for s[th] particle as usual and the current, electric and magnetic fields are $\boldsymbol{J}, \boldsymbol{E}$ and $\boldsymbol{B}$.

Introduce the symbols $f_\pm = f_x \pm if_y$ for $f = E, B, v$, Eq. (2.19) has the following two exact solutions, [80]

$$E_{\pm} = E_L e^{\pm i(\omega t - kz)}; \quad B_{\pm} = \pm\frac{ikc}{\omega}E_{\pm}; \quad v_{s\pm} = \mp\frac{iq_s E_{\pm}(\omega - kv_{sd})}{\gamma_s m_s \omega(\omega - kv_{sd} + \Omega_{cs}/\gamma_s)}; \tag{2.20a}$$

$$E_z = 0; \quad B_z = B_0; \quad v_{sz} = v_{sd}; \tag{2.20b}$$

$$n = n_{s0}; \quad \gamma_s = (1 - v_s^2/c^2)^{-1/2}; \quad \omega^2 - k^2c^2 = \sum_s \frac{(\omega_{ps}^2/\gamma_s)(\omega - kv_{sd})}{\omega - kv_{sd} + \Omega_{cs}/\gamma_s}. \tag{2.20c}$$

or

$$E_{\pm} = E_L e^{\mp i(\omega t - kz)}; \quad B_{\pm} = \pm\frac{ikc}{\omega}E_{\pm}; \quad v_{s\pm} = \pm\frac{iq_s E_{\pm}(\omega - kv_{sd})}{\gamma_s m_s \omega(\omega - kv_{sd} - \Omega_{cs}/\gamma_s)}; \tag{2.21a}$$

$$E_z = 0; \quad B_z = B_0; \quad v_{sz} = v_{sd}; \tag{2.21b}$$

$$n = n_{s0}; \quad \gamma_s = (1 - v_s^2/c^2)^{-1/2}; \quad \omega^2 - k^2c^2 = \sum_s \frac{(\omega_{ps}^2/\gamma_s)(\omega - kv_{sd})}{\omega - kv_{sd} - \Omega_{cs}/\gamma_s}. \tag{2.21c}$$

Here E_L, B_0 are arbitrary constant electric and magnetic field amplitudes, v_{sd} and $\Omega_{cs} = q_s B_0/(m_s c)$ are the constant drift velocity and cyclotron frequency for s[th] particle, respectively. Solutions (2.20) and (2.21) describe a right or left hand circularly polarized wave with electric field E_L and an external magnetic field B_0 in the plasmas. In different frequency limit, the electromagnetic wave can be the Whistler wave, the Alfven wave or the high frequency electromagnetic waves (RCP or LCP). Notice that the frequency ω and wavenumber k should satisfy the dispersion relation,

$$\omega^2 - k^2c^2 = \sum_s \frac{(\omega_{ps}^2/\gamma_s)(\omega - kv_{sd})}{\omega - kv_{sd} \pm \Omega_{cs}/\gamma_s}. \tag{2.22}$$

Here the plasma frequency ω_{ps} is denoted as $\omega_{ps}^2 = 4\pi n_s q_s^2/m_s$.

The verification of solutions (2.20) and (2.21) is easy. We take solution (2.20) as an example. First notice that γ_s is constant since $v_s^2 = v_{s+}v_{s-} + v_{sd}^2$ is constant. Hence Eq. (2.19a) is always satisfied. Meanwhile, the longitudinal and transverse components of Eq. (2.19b) become,

$$\frac{\partial p_{sz}}{\partial t} + v_z\frac{\partial p_{sz}}{\partial z} = q_s\left[E_z + \frac{1}{c}\left(v_{sx}B_y - v_{sy}B_x\right)\right]; \tag{2.23a}$$

$$\frac{\partial p_{s+}}{\partial t} + v_{sz}\frac{\partial p_{s+}}{\partial z} = q_s\left[E_+ + \frac{i}{c}(-v_{s+}B_z + v_{sz}B_+)\right]; \tag{2.23b}$$

$$\frac{\partial p_{s-}}{\partial t} + v_{sz}\frac{\partial p_{s-}}{\partial z} = q_s\left[E_- + \frac{i}{c}(v_{s-}B_z - v_{sz}B_-)\right]. \tag{2.23c}$$

The left hand side of Eq. (2.23a) is zero and the right hand side of Eq. (2.23a) is also zero, since

$$v_{sx}B_y - v_{sy}B_x = \frac{1}{2i}(-v_{s+}B_- + v_{s-}B_+) = \frac{kc}{2\omega}(v_{s+}E_- + v_{s-}E_+) \equiv 0.$$

Hence, Eq. (2.23a) always holds. On the other hand, the left hand side of Eqs. (2.23b) and (2.23c) is,

$$L = \pm i(\omega - kv_{sd})p_{s\pm} = \frac{q_s E_\pm(\omega - kv_{sd})^2}{\omega(\omega - kv_{sd} + \Omega_{cs}/\gamma_s)}. \tag{2.24}$$

The right hand side of Eqs. (2.23b) and (2.23c) is,

$$\begin{aligned} R &= q_s E_\pm \left[1 - \frac{q_s B_0(\omega - kv_{sd})}{\gamma_s m_s c\omega(\omega - kv_{sd} + \Omega_{cs}/\gamma_s)} - \frac{kv_{sd}}{\omega}\right] \\ &= q_s E_\pm \frac{(\omega - kv_{sd})^2}{\omega(\omega - kv_{sd} + \Omega_{cs}/\gamma_s)} = L. \end{aligned} \tag{2.25}$$

Thus, Eq. (2.19b) also holds. Notice that the longitudinal component of Eq. (2.19c) is always zero and the transverse component of Eq. (2.19c) is,

$$\begin{aligned} -\nabla^2 E_\pm + \frac{1}{c^2}\frac{\partial^2 E_\pm}{\partial t^2} &= \left(k^2 - \frac{\omega^2}{c^2}\right)E_\pm = -\sum_s \frac{4\pi n_s q_s}{c^2}\frac{\partial v_{s\pm}}{\partial t} \\ &= -\sum_s \frac{\omega_{ps}^2}{c^2}\frac{(\omega - kv_{sd})}{\gamma_s(\omega - kv_{sd} + \Omega_{cs}/\gamma_s)}E_\pm. \end{aligned} \tag{2.26}$$

Hence, if the dispersion relation (2.20c) is satisfied, Eq. (2.20) is the solution to Eq. (2.19). Similar procedure can used to prove that Eq. (2.21) is also the solution to Eq. (2.19).

2.2.2 Relativistic effects

Now let's look at the case when ion's motion is negligible and the drift velocity v_{ed} is zero. In this case, the relativistic factor and the dispersion relation are,

$$\gamma_e^2 = 1 + \frac{\gamma_e^2 \omega_E^2}{(\gamma_e\omega \pm \omega_{ce})^2}; \tag{2.27}$$

$$\omega^2 - k^2c^2 = \frac{\omega_{pe}^2}{\gamma_e \pm \omega_{ce}/\omega}; \tag{2.28}$$

Here $\omega_E = eE_L/(m_e c)$ and $\omega_{ce} = -\Omega_{ce} = eB_0/(m_e c)$. Eq. (2.27) is a fourth-order equation of γ_e. Combining Eqs. (2.27) and (2.28), we find,

$$\frac{\omega(\omega^2 - k^2c^2)}{\omega_{pe}^2\omega \mp \omega_{ce}(\omega^2 - k^2c^2)} = \left[1 - \left(\frac{eE_L}{m_e\omega c}\right)^2\left(\frac{\omega^2 - k^2c^2}{\omega_{pe}^2}\right)^2\right]^{1/2} \equiv \gamma_e^{-1}. \tag{2.29}$$

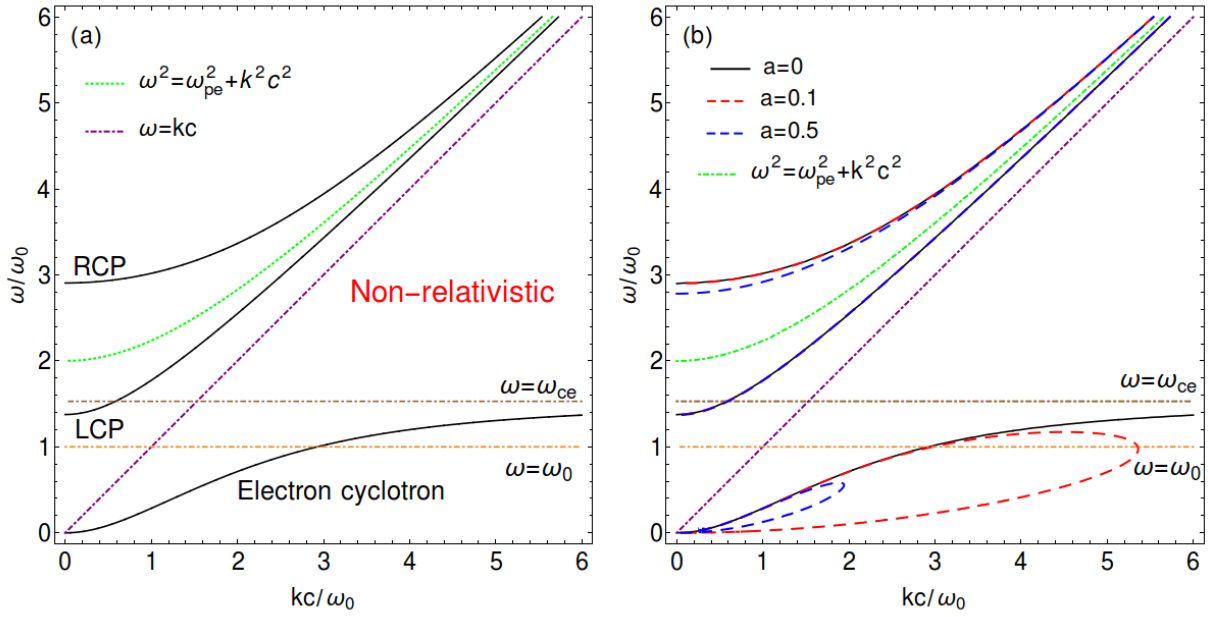

Fig. 2.3. (a) The dispersion relation in the nonrelativistic case without ion's motion; The high frequency right and left hand side circularly polarized electromagnetic waves (RCP and LCP) as well as the electron cyclotron wave are shown. (b) The comparison of relativistic and nonrelativistic dispersion relations with different laser amplitudes. Here $a = \omega_E/\omega_0$. The black line is for non-relativistic case and red and blue lines are for $a = 0.1$ and 0.5, respectively. The parameters are $\omega_{ce} = 1.53\omega_0$ and $\omega_{pe} = 2\omega_0$.

For infinitesimal perturbations, e.g. $E_L = 0$, Eq. (2.29) returns to the usual non-relativistic dispersion relation,

$$\omega^2 - k^2c^2 = \frac{\omega_{pe}^2}{1 \pm \omega_{ce}/\omega} \tag{2.30}$$

In Fig. 2.3(a), the non-relativistic dispersion relation Eq. (2.30) for $\omega_{pe} = 2\omega_0$ and $\omega_{ce} = 1.53\omega_0$ with ω_0 the laser frequency is plotted. The high frequency right and left hand side circularly polarized electromagnetic waves (RCP and LCP) and the electron cyclotron wave (Whistler) are all shown. Since we have neglected the ion's motion, Alfven branch is not included. In Fig. 2.3(b), we compare the dispersion relations in the relativistic and nonrelativistic cases with the same parameters. It is shown that with the inclusion of relativistic effects, both the frequencies of RCP and LCP components decreases and the RCP is more affected than the LCP component. This is because the rotation of electric field of the RCP wave is the same direction as the electron's motion. Hence, relativistic effects are more likely to appear. Interestingly, the electron cyclotron branch is found to shrink dramatically and in the ultra-relativistic regimes totally disappears. In the weakly relativistic regime, a new branch with larger wavenumber

compared to the electron cyclotron mode appears and it connects to the electron cyclotron mode at some critical point. Beyond this point, both the new branch and Whistler mode do not exist.

The shrink of the electron cyclotron mode is due to the relativistic increase of the electron mass. To see this, we expand Eq. (2.27) in the regime of $\gamma_e \gg 1$, [81]

$$\gamma_e \approx (\mp\omega_{ce} \pm \omega_E)/\omega \gg 1. \tag{2.31}$$

Substituting Eq. (2.31) into Eq. (2.28), we find the dispersion relation becomes,

$$\omega = \left(\frac{\omega_{pe}^4}{4\omega_E^2} + k^2c^2\right)^{1/2} \pm \frac{\omega_{pe}^2}{2\omega_E}. \tag{2.32}$$

Clearly, the electron cyclotron branch disappears since these two modes described by Eq. (2.32) are the LCP and RCP components in the ultra-relativistic approximation. The cut off frequency for LCP drops to zero whereas the cut off frequency for RCP becomes ω_{pe}^2/ω_E due to relativistic transparence. Both of them approach the asymptotic line $\omega = kc$ at large wavenumbers.

To verify the above results, we performed a PIC simulation to check the propagation modes. The simulation is done by the extended particle based integrated code (EPIC3D). The EPIC3D code is a three-dimensional (3D), fully relativistic electromagnetic particle-in-cell code in which various atomic and relaxation processes, such as the field and impact ionizations, Coulomb collision as well as the radiation reaction are involved. [82,83] These physical components can be turned on or off independently for different research purposes. Here, the EPIC3D code ignoring the ionization and collision processes is adopted. The simulation is set up as follows. The system size is 15.36μm in the y direction, which corresponds to $L_y = 3072$ in normalized unit of 0.005μm. A continuous plane laser wave with the wavelength of $\lambda_0 = 0.82$μm and the frequency of $\omega_0 = 2.3 \times 10^{15}\, rad/s$ is excited by the antenna current near the boundary. The laser is linearly polarized in the x direction. The intensity of the laser wave varies from $5.1 \times 10^{15}\,\mathrm{W/cm^2}$ to $2 \times 10^{18}\,\mathrm{W/cm^2}$, corresponding to normalized values from $a = 0.05$ to $a = 1.0$. A fully ionized carbon plasma with electron and ion temperature 0.5kev is initially set in the region between $y = 1024$ and 2048. The plasma is uniform with density $n_e = 6.64 \times 10^{21} cm^{-3}$ which corresponds to four times of the cut off density $n_c = 1.66 \times 10^{21} cm^{-3}$ or $\omega_{pe} = 2\omega_0$. The external magnetic field is also applied in the y direction with amplitude $B_0 = 20kT$ and the corresponding electron cyclotron frequency is $\omega_{ce} = 1.53\omega_0$. Under these conditions, the electron ion collision frequency is about $\nu_{ei} \sim 10^{13} s^{-1}$, which is much smaller than the laser frequency as well as the cyclotron frequency. Hence, neglecting the collision process is feasible in our simulations.

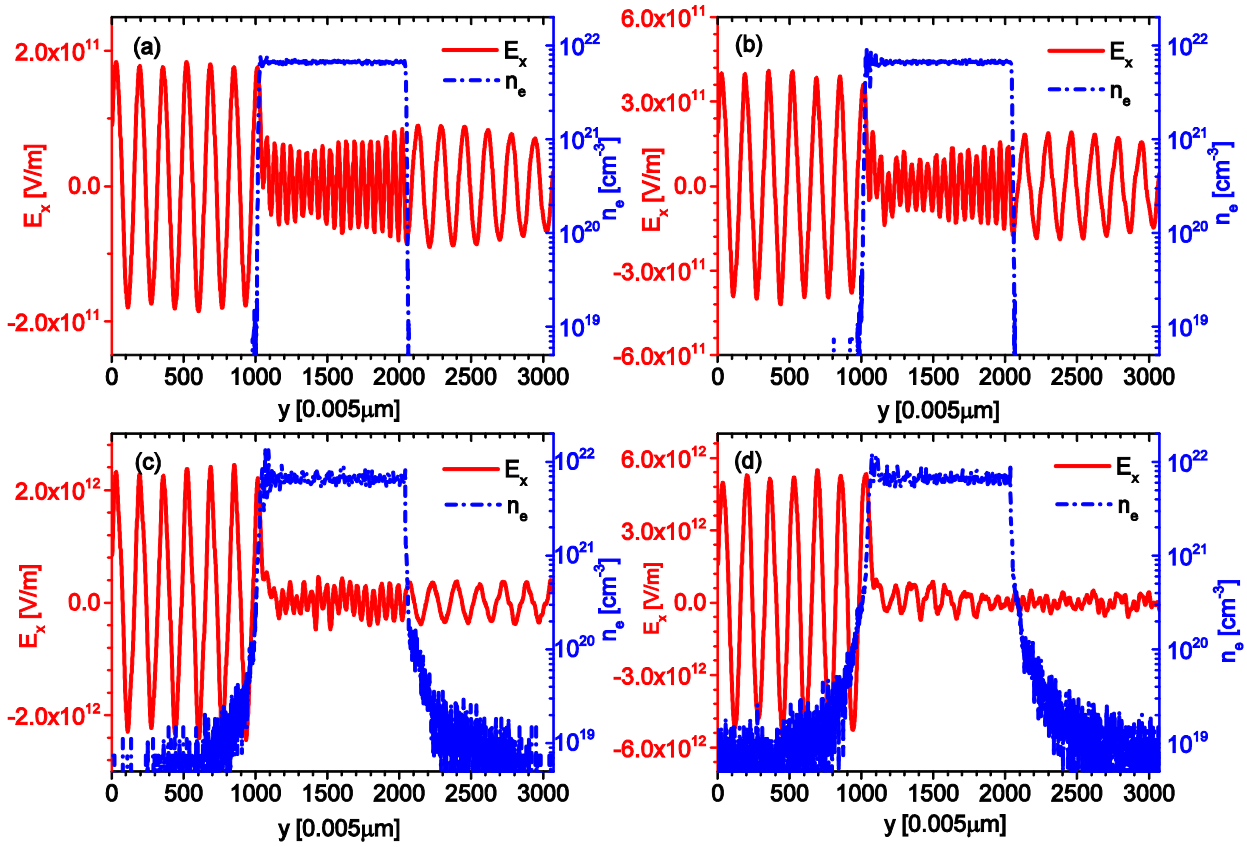

Fig. 2.4. The electric field of the laser and electron density at $t = 120.3fs$ with laser intensities (a) $a = 0.05$; (b) $a = 0.1$; (c) $a = 0.5$; and (d) $a = 1$.

In Fig. 2.4, we show the propagation of the wave and density for different laser intensities at $t = 120.3fs$. It can be seen that when the laser intensity is small, e.g. $a = 0.05$ and 0.1 in Fig. 2.4(a) and (b), the laser can propagate into the over-dense plasma as short wavelength waves. And at the rear plasma-vacuum boundary, the wavelength returns to the incident laser wavelength. Notice that the amplitude of the transmitted wave is about half of the incident laser, hence in the non-relativistic or weakly relativistic regimes, half of the linearly polarized laser can penetrate into the over-dense plasma as the right hand side circularly polarized electron cyclotron mode. When the laser intensity becomes large, e.g. $a = 1$ in Fig. 2.4(d), there is no propagation mode. At the intermediate regime with $a = 0.5$ in Fig. 2.4(c), only a small portion of the laser wave can propagate into the over-dense plasma. In fact, such penetration only happens at the early time. At later time, e.g. $t > 170fs$, this propagation mode disappears. These observations are qualitatively consistent with the predictions.

To further investigate the propagation modes, we have shown in Fig. 2.5(a) the fast Fourier transformation (FFT) results of the electric field depicted in Fig. 2.4(a) and (b). The FFT region is between

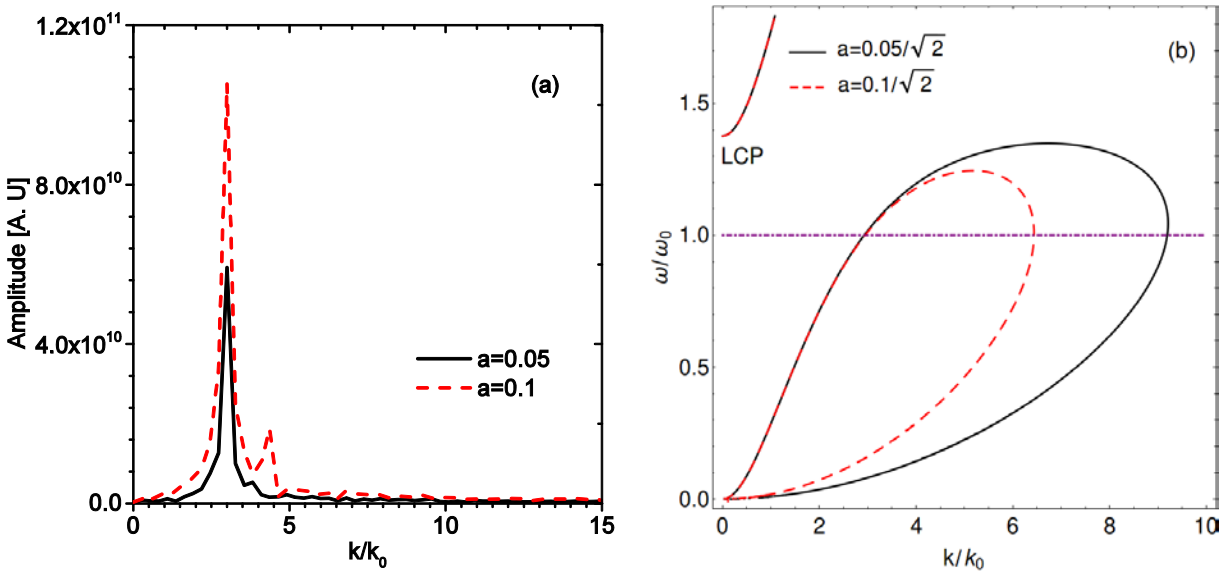

Fig. 2.5. (a) The spectrum of the wavelength for the propagation modes depicted in Fig. 2.4(a) and (b). The spectrum analysis is done between the region $y = 1400$ and $y = 2000$ (b) The enlarged plot of the dispersion relations for $a = 0.05/\sqrt{2}$ and $a = 0.1/\sqrt{2}$. Notice that in the simulation the laser is linearly polarized, hence the effective intensity for the right hand circularly component should be divided by a factor of $\sqrt{2}$.

$y = 1400$ and $y = 2000$. In Fig. 2.5(b), the enlarged plot of the dispersion relations for $a = 0.05/\sqrt{2}$ and $0.1/\sqrt{2}$ are shown. It should be mentioned that in the simulation the laser is linearly polarized, hence the effective intensity for the right hand circularly component should be divided by a factor of $\sqrt{2}$. It can be seen from Fig. 2.5(a) that the propagation modes have the $3.0k_0$ component for both $a = 0.05$ and $a = 0.1$. Also there is another peak at around $4.4k_0$ when $a = 0.1$. On the other hand, the theory predicts that in both cases there are two propagation modes: one with longer wavelength at around $k_1 = 2.93k_0$, which fits the simulation very well; and the other with shorter wavelength at $k_2 = 9.2k_0$ for $a = 0.05$, which is not found in the simulation and $k_2 = 6.4k_0$ for $a = 0.1$, which is a little different from the simulation. These differences may come from the difficulty for PIC simulations to resolve the very short wavelength waves on the one hand and the non-applicable of the fluid model in the intense laser regime on the other hand.

2.3 Summary

In this chapter, we have obtained the exact expressions of the charged particle's orbit inside the relativistic laser field in the presence of strong parallel magnetic field. Such expressions can be used to calculate the

radiations from the particles which become important when the laser intensity exceeds $10^{23} W/cm^2$. Then the relativistic dispersion relation for the magnetized plasmas are discussed. Specifically, a new branch is found in the weakly relativistic regime and the electron cyclotron mode shrinks and totally disappears in the ultra-intense regimes. Our PIC simulations qualitatively fit the theoretical predictions.

3. Simulation of laser plasma interactions in the presence of strong magnetic field

In this chapter, we investigate the various propagation modes in strongly magnetized plasmas in both the linear and nonlinear regimes by the EPIC3D code. The conversion of the propagation modes and their polarizations as well as the effects on plasma absorption rate are studied. Both 1D and 2D simulations are performed with different magnetic field strengths and laser polarizations and intensities. The linear propagation modes namely the left and right hand side circularly polarized (LCP and RCP) modes and electron cyclotron mode (Whistler mode) are analyzed in the inhomogeneous density areas. Specifically, the nonlinear propagation mode—soliton in magnetized plasmas is observed, which greatly enhances the laser heating efficiency. The laser intensity and magnetic field regions where the electron cyclotron resonance heating (ECRH) and soliton induced enhanced heating dominate respectively are identified. By the end of the chapter, the characteristics and stabilities of the solitons are investigated.

3.1 Laser heating in magnetized plasmas

To investigate the laser plasma interactions in the presence of strong magnetic field, we have employed the EPIC3D code [82, 83] as introduced in the previous chapter. In this section, we mainly present the 1D simulation results and the 2D results are discussed in the last section.

3.1.1 Simulation setup

The simulation is set up as follows. The system size is 15.36μm in the y direction, which corresponds to $L_y = 3072$ in normalized unit of 0.005μm. The Gaussian shaped laser pulse with the wavelength of $\lambda_0 = 0.82\mu m$, the frequency of $\omega_0 = 2.3 \times 10^{15}\, rad/s$ and the duration of 40fs is excited by the antenna current near the left boundary. The laser is plane wave and linearly polarized (LP) in the x direction unless otherwise specified. The peak intensity of the laser pulse varies from $2.1 \times 10^{16}\,\mathrm{W/cm^2}$ to $8.2 \times 10^{18}\,\mathrm{W/cm^2}$, corresponding to normalized values from $a = 0.1$ to $a = 2.0$. A fully ionized carbon plasma with electron and ion temperature $T_e = T_i = 0.5kev$ is initially set in the region between $y = 500$ and

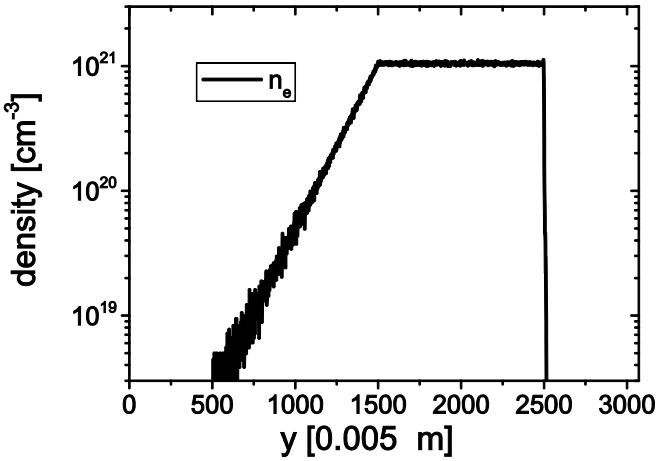

Fig. 3.1. The initial electron density profile. The laser irradiates from the left boundary and the external magnetic field is along the y direction. Periodic boundary conditions are employed for particles and laser is outgoing in y direction. The uniform plasma density is about $0.63n_c$ with n_c the cutoff density.

2500 and a pre-profile of density with $n_e(y) = 0.63n_c \exp[(y-1500)/164]$ is assumed from $y = 500$ to 1500, as shown in Fig. 3.1. Here, $n_c = 1.66 \times 10^{21} cm^{-3}$ is the cut off density for the laser wave. Periodic boundary conditions are employed for particles in both x and y directions as well as the waves in the x direction, and in the y direction the waves are outgoing. The external strong uniform magnetic field B_0 is applied along the y direction. The minimum adopted magnetic field is 2kT corresponding to an electron cyclotron frequency at $\omega_{ce} = 0.15\omega_0$. Notice that the collision frequency between the electrons and ions are $v_{ei} \sim 10^{13} s^{-1}$, which is much smaller than the laser frequency as well as the smallest cyclotron frequency. Hence, in the simulations we have neglected the collision processes.

3.1.2 Plasma absorption rate and polarization

The laser absorption rate is used to evaluate the laser heating efficiency during the propagation of the laser pulse in the magnetized plasma, as summarized in Fig. 3.2. The absorption rate is calculated by the ratio of the energy increment of electrons and ions to half of the antenna energy. It is found that, the dependence of heating efficiency on the laser intensity is different with the magnetic field. Generally, larger amplitude laser in the plasma with strong magnetic field has higher heating efficiency. However, for not so strong magnetic field, there exists a region of moderate laser intensity where enhanced heating occurs, e.g. $a = 0.4 \sim 0.8$ for $B_0 = 3.8kT$, as shown in Fig. 3.2(a). The enhanced laser heating region moves towards the lower intensity direction as the magnetic field increases and disappears as the magnetic field approaches the value where the electron cyclotron resonance happens. Afterwards, the heating efficiency is almost independent of the laser intensity. Hence, the absorption is characterized mainly by the ECRH in the high magnetic field regime. This is also evidenced by Fig. 3.2(b) in which, for high power laser, ($a = 2.0$), the heating efficiency increases up to a peak as the magnetic field increases. Note that there is a little decay at the beginning when the magnetic field is weak. The corresponding magnetic field of the peak is consistent

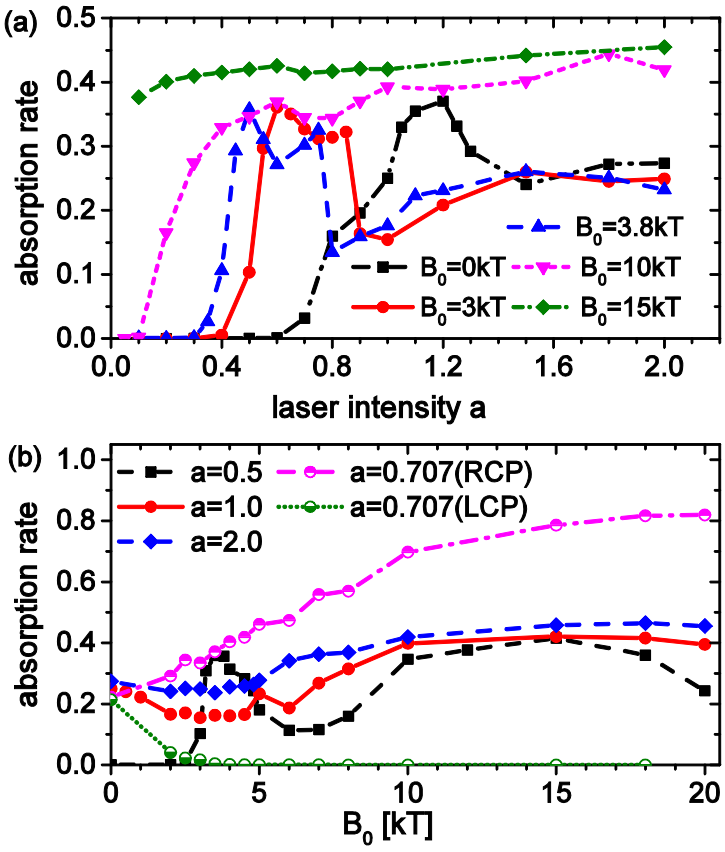

Fig. 3.2. Plasma absorption rate for different magnetic fields (a) and laser intensities and polarizations (b). Here RCP (LCP) means right (left) hand circularly polarized laser. The other lasers are linearly polarized (LP).

with the electron cyclotron resonance. Theoretically, it is estimated around $B_0 = 13kT$, which is slightly lower than the observation in Fig. 3.2(b). The difference may result from the relativistic correction of the electron cyclotron frequency.

In Fig. 3.2(b), the cases of LCP and RCP laser pulses with intensity $a = 0.707$ are also plotted to show the polarization effects on the heating efficiency. The total energy of the LCP and RCP lasers is the same as the linearly polarized one with $a = 1.0$. In the absence of magnetic field, i.e., $B_0 = 0kT$, linearly polarized laser has slightly higher heating efficiency compared to the LCP or RCP laser because of the ponderomotive oscillations in the longitudinal direction. However, when the magnetic field is present, the heating efficiency decreases with magnetic field for LCP lasers due to the easier penetration, whereas the RCP laser has an increasing heating efficiency since the ECRH effects become more and more significant.

Interestingly, the enhanced heating efficiency peak appears again around $B_0 = 3.8kT$ for the laser pulse with moderate amplitude, i.e., $a = 0.5$, as shown in Fig. 3.2(b). In the 1D simulations, the peak efficiency is about 37%, comparable to the ECRH efficiency. In fact, a localized mode, namely a solitary wave is observed at this parameter. Fig. 3.3 shows the time evolution of the laser magnetic field amplitude with $a = 0.5$ at the pre-plasma ($y = 1000$), uniform plasma ($y = 2000$) and vacuum ($y = 2750$) regions

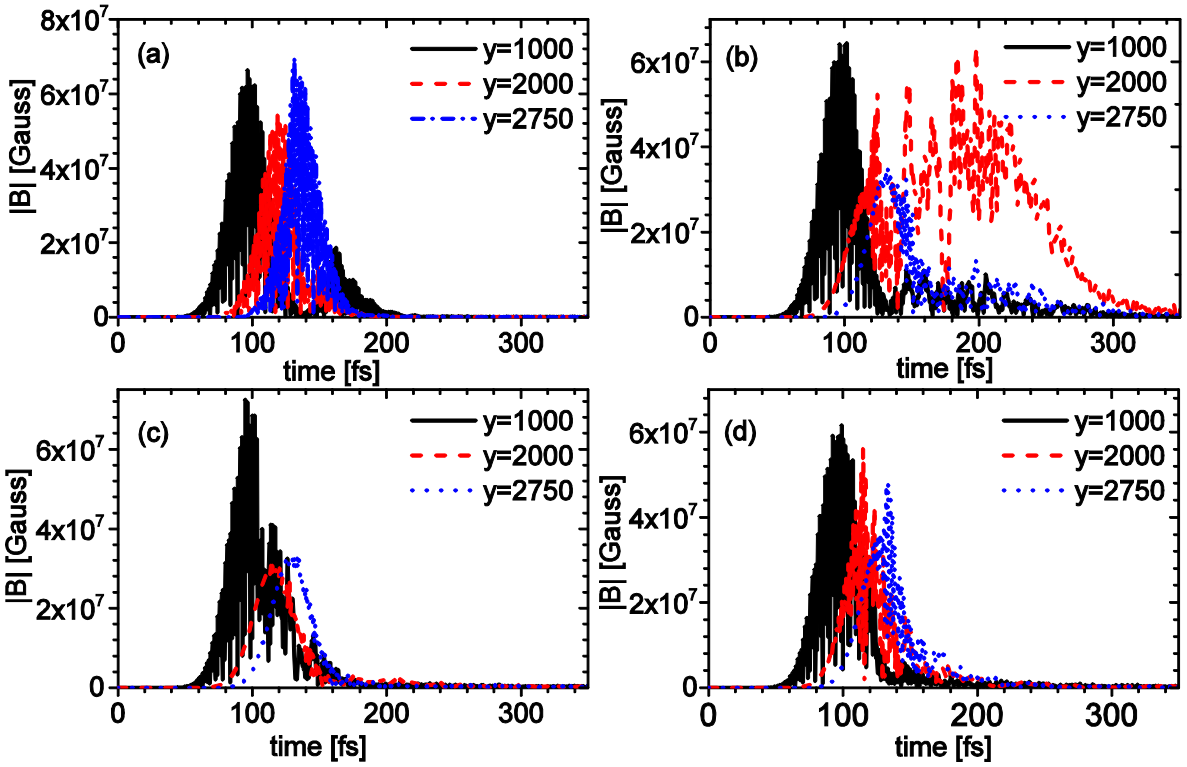

Fig. 3.3. Time evolution of laser magnetic field amplitude at the pre-plasma $y = 1000$ (solid), the uniform plasma $y = 2000$ (dash), and the vacuum $y = 2750$ (dash-dotted) for (a) $B_0 = 0kT$; (b) $B_0 = 3.8kT$, (c) $B_0 = 10kT$ and (d) $B_0 = 18kT$ with $a = 0.5$. The time oscillations imply the linearly polarization of the incident laser field.

for different magnetic fields. The Fig. 3.3(a) is without magnetic field for comparison. While the time oscillations of the laser field at $y = 1000$ (black solid lines) in each plot exhibit the linearly polarization of the incident laser pulse, their disappearance at $y = 2000$ (red dashed lines) and 2750 (blue dash-dotted lines) in Fig. 3.3(c) signifies a polarization conversion from linearly to circularly polarized one. Note that the blue dash-dotted lines indicate that the laser pulses have passed through all the observation locations with pulse length of 40fs. The prolonged red dashed lines in Fig. 3.3(b) imply that part of the laser wave has converted into the solitary wave. Meanwhile, since there is no peak at $y = 2750$ after $t = 140$ fs, the solitary wave has been trapped at $y = 2000$ for a long time and totally absorbed, which contributes to the peak of heating efficiency in Fig. 3.2(b). In Fig. 3.3(d), the laser passes through all the points and the oscillations at $y = 2000$ and 2750 imply that the laser has changed to elliptically polarized compared to Fig. 3.2(a) and Fig. 3.2(c).

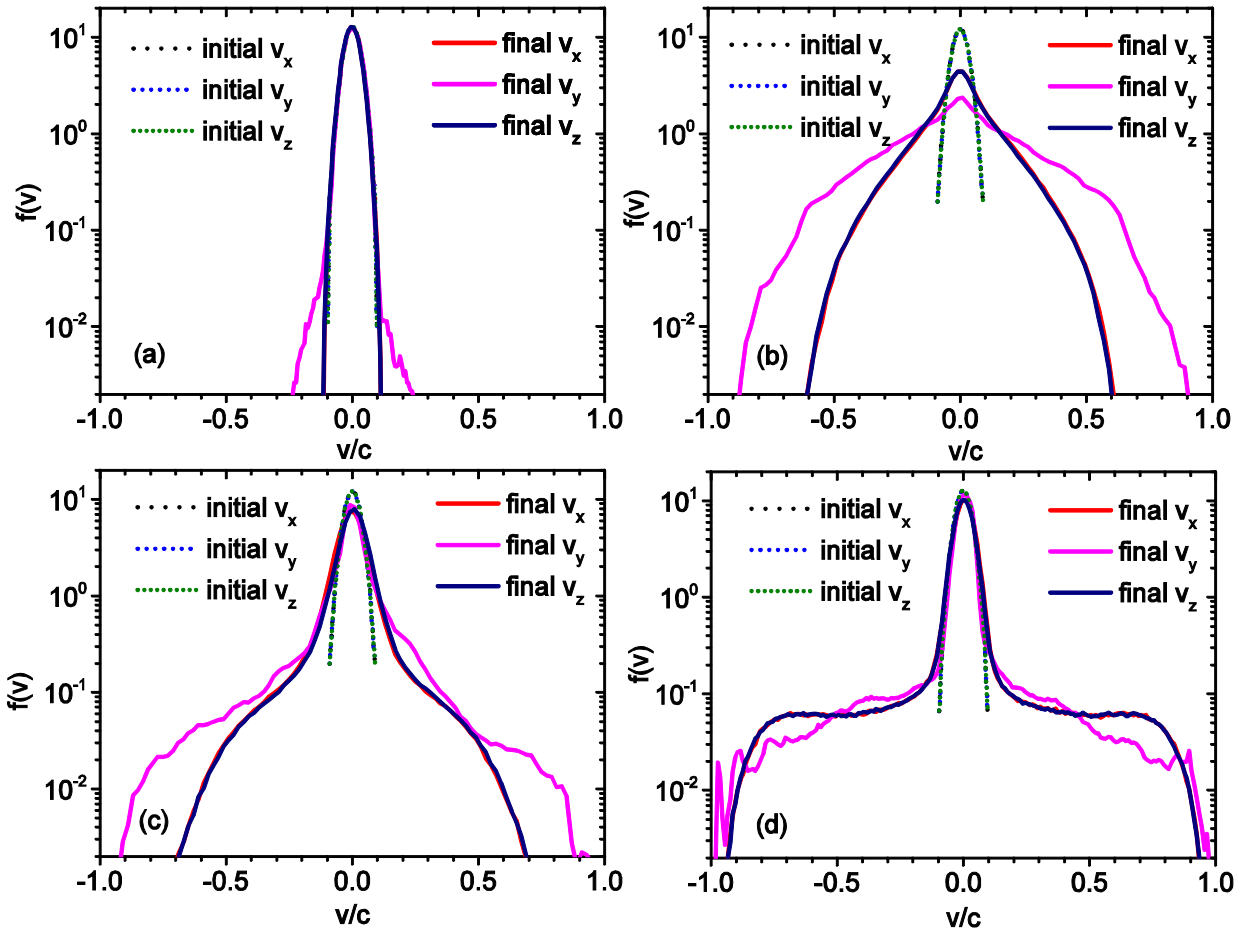

Fig. 3.4. The initial and final velocity distributions for different magnetic fields with $a = 0.5$. (a) $B_0 = 2kT$; (b) $B_0 = 3.8kT$; (c) $B_0 = 7kT$ and (d) $B_0 = 15kT$. The initial distributions are Maxwell-Boltzmann for v_x, v_y and v_z. The final distributions are taken at a long enough time when the laser or solitons disappear. In (b), the soliton induced enhanced heating is dominant and in (d) the ECRH is dominant.

3.1.1 Velocity distribution

To further investigate the plasma absorption rate with magnetic field, we have shown in Fig. 3.4 the comparison of initial and final velocity distributions with different magnetic fields for $a = 0.5$. The initial distribution is Maxwell-Boltzmann. The four figures in Fig. 3.4 (a)-(d) correspond to the no heating case ($B_0 = 2kT$); the soliton induced heating case ($B_0 = 3.8kT$); the transition from soliton to ECRH case ($B_0 = 7kT$) and the ECRH dominated case ($B_0 = 15kT$). It can be seen that when where is weak magnetic field, the energy is first deposited in the longitudinal direction and as the magnetic field increases the energy starts to deposit in the transverse direction. Furthermore, the distribution function in the x direction is exactly the same as the one in the z direction due to the cyclotron effects. Notice that the total heating

efficiencies for Fig. 3.4(b) and Fig. 3.4(d) are almost the same. In the ECRH dominant regime, e.g. Fig. 3.4(d), the main body of the distribution function is Maxwell and there is energetic tails. This means small portion of the electrons are heated to very high velocities. In the region where soliton is generated, e.g. Fig. 3.4(b), the distribution function strongly deviates from the Maxwell. In this case, more electrons are heated to moderate energies.

As discussed in the previous chapter, the propagation modes of the laser pulse in magnetized plasma strongly depend on the magnetic field strength. In the next two section, we will analysis the various linear and nonlinear propagation modes in magnetized plasmas.

3.2 Linear propagation modes

The linear propagation modes of the laser pulse along the magnetic field direction can be described generally by following the wave equation in the limit of cold plasmas, [84]

$$\frac{\partial^2 E_\pm}{\partial y^2} + \frac{\omega_0^2}{c^2}\left(1 - \frac{\omega_{pe}^2}{\omega_0(\omega_0 \pm \Omega_{ce})}\right)E_\pm = 0. \tag{3.1}$$

Here $\Omega_{ce} = q_e B_0/(m_e c)$ and $q_e = -e$. The electric field component is written as $E_\pm = E_z \pm iE_x$, in which '$\pm$' represent the RCP and LCP waves, respectively. This equation can be solved exactly in the pre-plasma region ($y = 500\sim1500$) with density profile of $n_e = n_0 \exp[(y - y_0)/L]$. Here, $y = y_0$ is the left boundary of the plasma and n_0 is the uniform plasma density. In the simulations, $y_0 = 500$, $L = 164$ and $n_0 = 0.63n_c$. Using the variable transformation,

$$\xi_\pm = 2\frac{\omega_0 L}{c}\frac{\omega_{pe0}}{[\omega_0(\omega_0 \pm \Omega_{ce})]^{1/2}}\exp\left(\frac{y - y_0}{2L}\right), \tag{3.2}$$

Eq. (3.1) can be rewritten as the modified Bessel equation in form,

$$\xi_\pm^2\frac{\partial^2 E_\pm}{\partial \xi_\pm^2} + \xi_\pm\frac{\partial E_\pm}{\partial \xi_\pm} - \left(\xi_\pm^2 - \frac{4\omega_0^2 L^2}{c^2}\right)E_\pm = 0. \tag{3.3}$$

Here $\omega_{pe0}^2 = 4\pi n_0 q_e^2/m_e$. The general solution of Eq. (3.3) is,

$$E_\pm = c_{1\pm} I_\nu(\xi_\pm) + c_{2\pm} K_\nu(\xi_\pm) \tag{3.4}$$

$c_{1\pm}$, $c_{2\pm}$ are integration constants depending on the boundary conditions. $I_\nu(\xi_\pm)$ and $K_\nu(\xi_\pm)$ are the modified Bessel functions of the second kind with the order $\nu = \pm i\,2\omega_0 L/c$. Eq. (3.4) describes the linear propagation and polarization properties of the electromagnetic waves in strongly magnetized

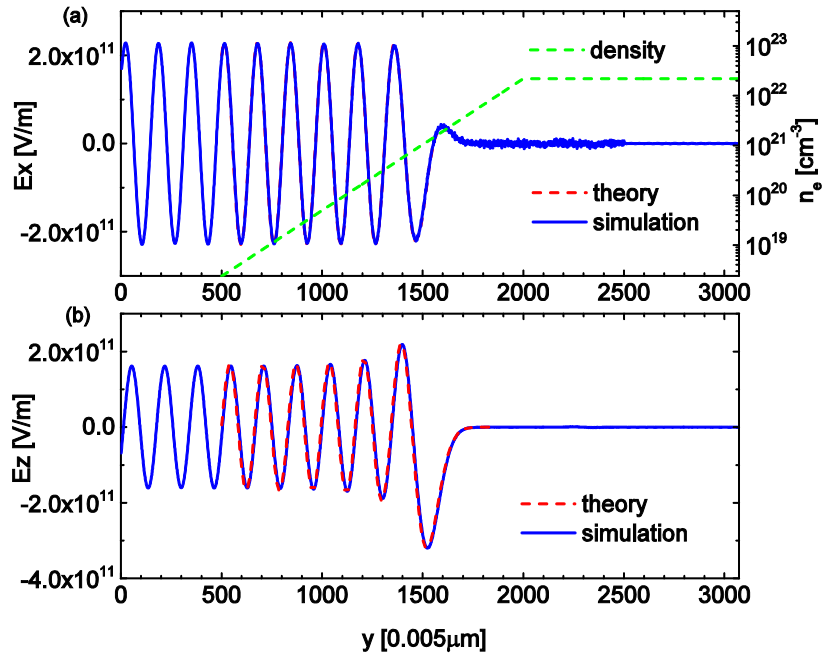

Fig. 3.5. (a) The spatial profile of E_x (left axis) and initial density profile (right axis); (b) the spatial profile of E_z. The parameters are $B_0 = 2\text{kT}, a = 0.05$ and $n_0 = 13.3n_c$.

inhomogeneous plasmas. With different magnetic field, the laser propagation and absorption behaves differently depending on the linear propagation modes characterized by the polarizations.

3.2.1 LCP and RCP modes

In the case with weaker magnetic field strength, i.e., $|\Omega_{ce}| < \omega_0$, the laser cannot access into the high density plasma. As $\xi_\pm \to \infty$, it gives $I_\nu(\xi_\pm) \to e^{\xi_\pm}/\sqrt{2\pi\xi_\pm}$ and $K_\nu(\xi_\pm) \to e^{-\xi_\pm}\sqrt{\pi/2\xi_\pm}$. Hence $c_{1\pm} = 0$. Assuming a linearly polarized laser with $E_z = 0$ and $E_x = E_0$ at $y = y_0$ initially, the electric field components can be written as,

$$\begin{cases} E_x = \dfrac{E_0}{2}\left[\dfrac{K_\nu(\xi_+)}{K_\nu(\xi_{+0})} + \dfrac{K_\nu(\xi_-)}{K_\nu(\xi_{-0})}\right]; \\ E_z = \dfrac{E_0}{2}\left[\dfrac{K_\nu(\xi_+)}{K_\nu(\xi_{+0})} - \dfrac{K_\nu(\xi_-)}{K_\nu(\xi_{-0})}\right] e^{\frac{\pi}{2}i}. \end{cases} \tag{3.5}$$

Here $\xi_{\pm 0} = 2(\omega_0 L/c)\{\omega_{pe}/[\omega_0(\omega_0 \pm \Omega_{ce})]^{1/2}\}$. It should be emphasized that the boundary conditions used here are artificial since the polarization direction keeps rotating as the laser propagates. As a result, the laser field at $y = y_0$ also rotates due to the reflection. However, there still exists a moment probably taken as an initial time when the imposed boundary conditions are satisfied. Eq. (3.5) shows that $E_z \equiv 0$ when $B_0 = 0$, so that the laser keeps linearly polarized. However, when $B_0 \neq 0$, E_z increases or the Faraday rotation takes place. The rotating angle of the polarization direction can be calculated through the

ratio between E_z and E_x. Note that in the over-dense area, both the RCP and LCP components decay as $\sqrt{\pi/2\xi_\pm}\, e^{-\xi_\pm}$. However, the RCP component decays faster than the LCP since ξ_+ is always larger than ξ_-. Resultantly, for a proper high density plasma only the LCP component may be able to propagate into the main plasmas. Hence, the incident linearly polarized propagation mode may convert into the LCP wave with $E_z \approx -iE_x$. This analytical result is consistent with the numerical observation on the disappearance of the time oscillations at y=2000 and 2750 in Fig. 3.3(c). Furthermore, such decay and conversion characteristics of different propagation modes may be helpful to understand the dependence of the laser heating efficiency on the magnetic field strength observed in Fig. 3.2(b), where the heating efficiency decreases in the weak magnetic field region due to the above mode conversion.

To further verify the solution Eq. (3.5), a PIC simulation for $B_0 = 2\text{kT}$ or $|\Omega_{ce}| = 0.153\omega_0$ is performed with the same initial density profile as in the analysis. The pre-plasma area is extended to $y = 2000$ to examine the cutoff of linearly polarized continuous laser so that the uniform plasma becomes over-dense (the uniform plasmas density is $13.3n_c$). A rather weak laser intensity is chosen ($a = 0.05$) to avoid the nonlinearity in the simulation. Fig. 3.5 clearly exhibits that E_z is amplified and both the RCP and LCP components cut off successively as the density increases.

3.2.2 Electron cyclotron mode (Whistler mode)

In the case with stronger magnetic field $|\Omega_{ce}| > \omega_0$, ξ_- is real for the LCP wave. Then, c_{1-} remains zero. However, for the RCP wave, ξ_+ is imaginary so that both $I_\nu(\xi_+)$ and $K_\nu(\xi_+)$ are kept. For simplicity, an initial condition with $E_z = 0$ and $E_x = E_0$ at $y = y_0$ is still assumed, then the electric field can be written as,

$$\begin{cases} E_x = \dfrac{E_0}{2}\left[\dfrac{K_\nu(\xi_-)}{K_\nu(\xi_{-0})} + \dfrac{I_{\nu 0}^R K_\nu^I - K_{\nu 0}^R I_\nu^I}{I_{\nu 0}^R K_{\nu 0}^I - I_{\nu 0}^I K_{\nu 0}^R} + i\,\dfrac{K_{\nu 0}^R I_\nu^R - I_{\nu 0}^R K_\nu^R}{I_{\nu 0}^R K_{\nu 0}^I - I_{\nu 0}^I K_{\nu 0}^R}\right]; \\ E_z = \dfrac{E_0}{2}\left[-\dfrac{K_\nu(\xi_-)}{K_\nu(\xi_{-0})} + \dfrac{I_{\nu 0}^R K_\nu^I - K_{\nu 0}^R I_\nu^I}{I_{\nu 0}^R K_{\nu 0}^I - I_{\nu 0}^I K_{\nu 0}^R} + i\,\dfrac{K_{\nu 0}^R I_\nu^R - I_{\nu 0}^R K_\nu^R}{I_{\nu 0}^R K_{\nu 0}^I - I_{\nu 0}^I K_{\nu 0}^R}\right] e^{\frac{\pi}{2}i}. \end{cases} \tag{3.6}$$

Here $I_\nu^R = Re[I_\nu(\xi_+)]$, $I_\nu^I = Im[I_\nu(\xi_+)]$, $K_\nu^R = Re[K_\nu(\xi_+)]$, $K_\nu^I = Im[K_\nu(\xi_+)]$. The subscript '0' stands for the value taken at $y = y_0$. The superscripts 'R' and 'I' denote the real and imaginary parts, respectively. Eq. (3.6) shows that the linearly polarized laser converts into an elliptical one and the ellipticity varies spatially. This is consistent with the results shown in Fig. 3.3(d). As $\xi_\pm \to \infty$, the RCP wave decays with $1/\sqrt{\xi_+}$, while the LCP wave decays with $e^{-\xi_-}\sqrt{\pi/2\xi_-}$. Hence, in the over-dense plasma, the RCP component can propagate much deeper than LCP component. In this case, the linearly polarized laser may

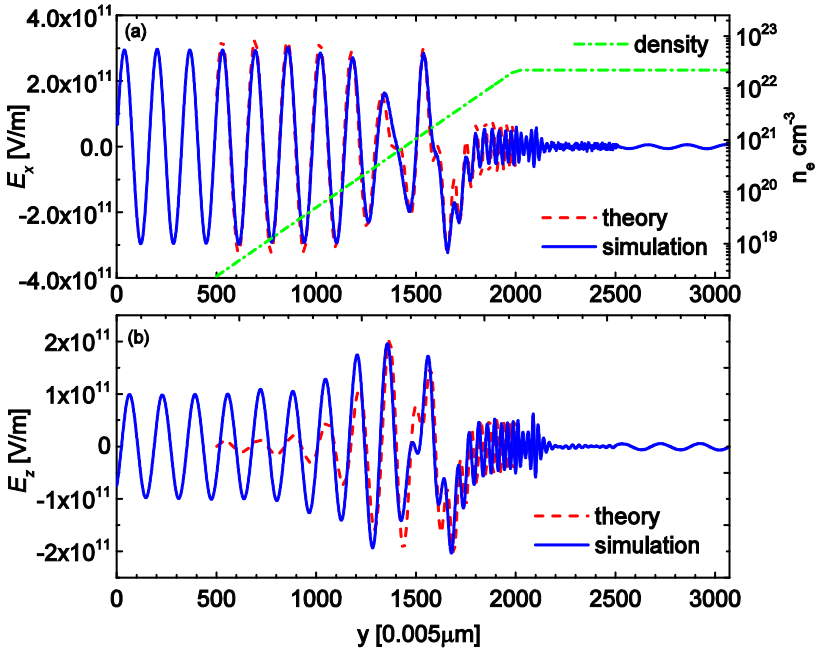

Fig. 3.6. (a) The spatial profile of E_x (left axis) and initial density profile (right axis); (b) the spatial profile of E_z. The parameters are $B_0 = 18\text{kT}, a = 0.05$ and $n_0 = 13.3n_c$.

convert into an electron cyclotron mode which oscillates in space as $e^{i|\xi_+|}$. The laser wave behaves more like a right hand circularly polarized one since $E_z \approx iE_x$.

To validate the theoretical analysis, a PIC simulation for $B_0 = 18\text{kT}$ and with other parameters same as in Fig. 3.5 is carried out as shown in Fig. 3.6. It can be seen that the laser wave penetrates into the over-density plasma area as a short wavelength electron cyclotron mode. At $y = 2000$, the laser wave can be extended approximately in the propagation direction with a relation of $E_+ \propto e^{i0.237y}$. It is comparable to the theoretical prediction $E_+ \propto e^{i0.228y}$. The difference for E_z at the left boundary results from the assumption of the artificial boundary conditions in Eq. (3.6).

Eq. (3.1) describes the linear propagation modes with different magnetic fields in the limit of cold plasmas. However, the nonlinear dynamics may become dominant under certain conditions even if the laser intensity is not very strong, as exhibited in the parameter window for moderate laser intensities in Fig. 3.2, where solitary waves are generated in the uniform density area. This is because in the presence of magnetic field, the ponderomotive force depends on not only the laser intensity but also the magnetic field. In the next section, we will discuss the nonlinear propagation mode - soliton in magnetized plasmas.

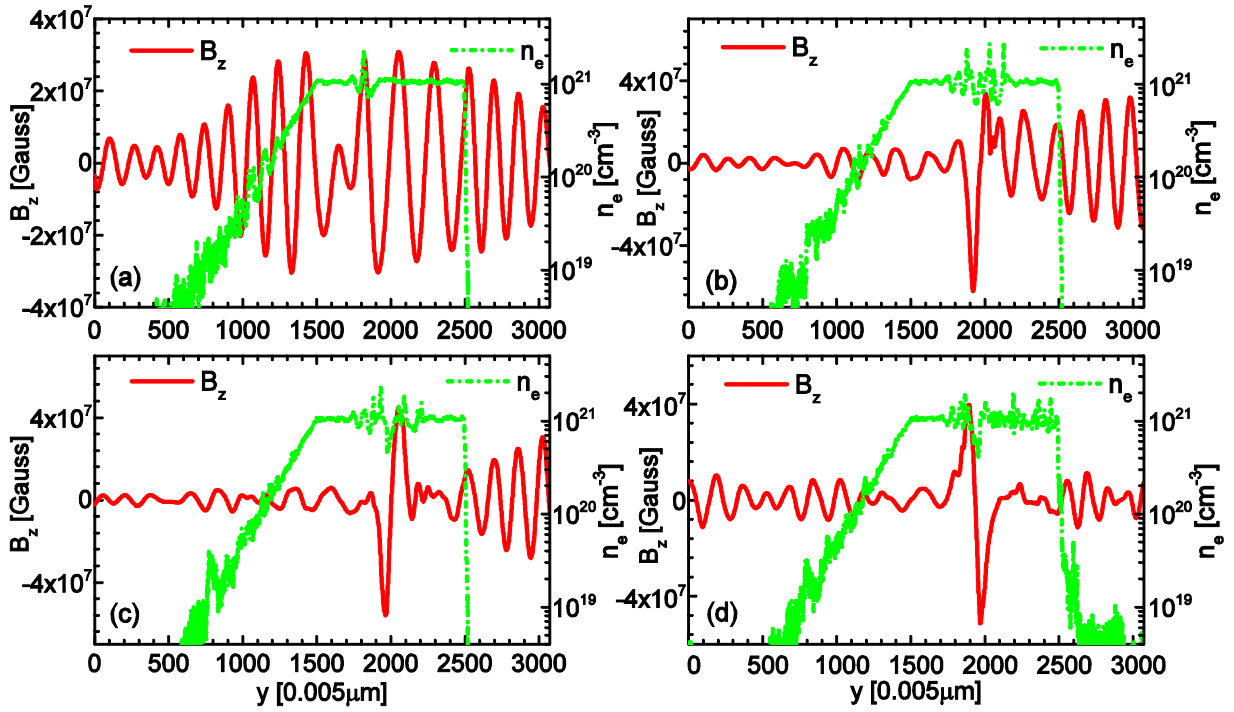

Fig. 3.7. The time evolution of a standing soliton at $t = 119.6fs$ (a), $t = 135.6fs$ (b), $t = 139.1fs$ (c) and $t = 161.1fs$ (d) with $a = 0.5$ and $B_0 = 3.8kT$.

3.3 Nonlinear propagation modes (soliton)

The soliton is generated due to the cancellation between the nonlinearities and the dispersion effects due to the finite electron inertia. Generally, the nonlinearities in laser plasma interactions come from the relativistic correction of particle's mass and the redistribution of plasma density due to the ponderomotive force. In the presence of magnetic field, both of the two nonlinearities are affected by the magnetic field (see Chapter 4). Hence, solitons can be generated at relatively weak laser intensity region.

3.3.1 Soliton generation in magnetized plasma

To clarify the soliton formation mechanism, the spatiotemporal evolution of the soliton is depicted in Fig. 3.7 with $a = 0.5$ and $B_0 = 3.8kT$. It can be seen that a standing soliton is generated at $y = 2000$ with a plasma density cavity. The soliton is long-lived in 1D simulations with almost zero propagation velocity and a quite narrow width, e.g., about one laser wavelength. The mechanism of the soliton generation is as follows [59]. First the density perturbation is generated after the laser pulse due to the ponderomotive force and the laser starts to lose energy. Meanwhile, the laser frequency decreases (see Fig. 3.9) because this

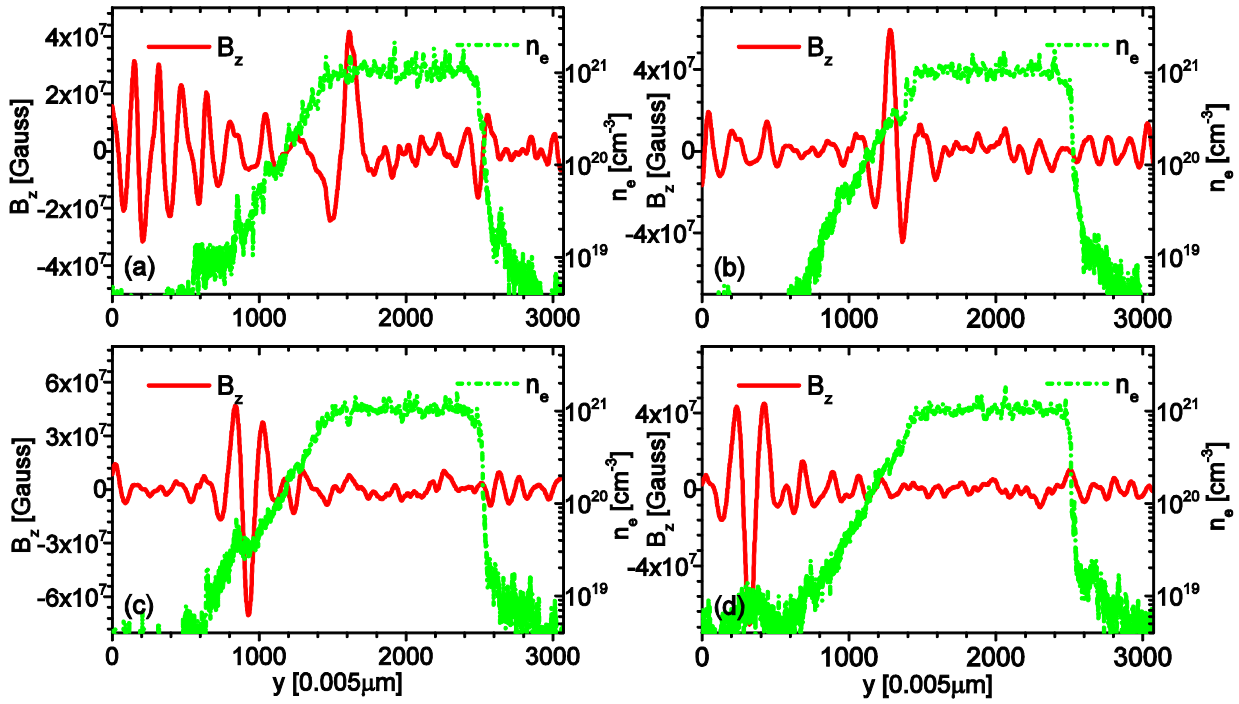

Fig. 3.8. The time evolution of a moving soliton at $t = 164.1fs$ (a), $t = 174.1fs$ (b), $t = 181.1fs$ (c) and $t = 191.1fs$ (d) with $a = 1.0$ and $B_0 = 4.5kT$.

energy transfer is an adiabatic process and the ratio between the wave energy density and the frequency is conserved. Once the laser frequency falls below the plasma frequency, the laser wave becomes trapped in the density cavity, forming a solitary wave. In magnetized plasmas, the group velocity v_g of the laser pulse is,

$$v_g = \frac{d\omega}{dk} = \frac{2kc^2}{2\omega - \omega_{pe}^2\Omega_{ce}/(\omega + \Omega_{ce})^2}. \tag{3.7}$$

In the weak magnetic field regime $|\Omega_{ce}/\omega| \ll 1$, $dv_g/d\omega < 0$, the group velocity decays with the frequency. Hence, the soliton wave propagates with very low velocity. In fact, in the simulations it is almost zero in the uniform plasmas. As a result, the laser can be absorbed efficiently in the standing density well. In the case of weakly relativistic limit, the frequency downshift is approximately proportional to the density perturbation and laser intensity. Meanwhile it has a positive correlation with the magnetic field strength [71]. Hence, as the magnetic field increases, the laser intensity needed for the soliton formation reduces. In some cases, e.g. when the soliton is generated in the inhomogeneous areas, the density perturbation is not large enough to trap the laser wave and the soliton can collapse after its generation or moves away. In this case, the heating efficiency decreases compared to standing soliton cases. In Fig. 3.8, we show an example of the moving soliton generated near the pre-plasma region for $B_0 = 4.5kT$ and $a = 1.0$.

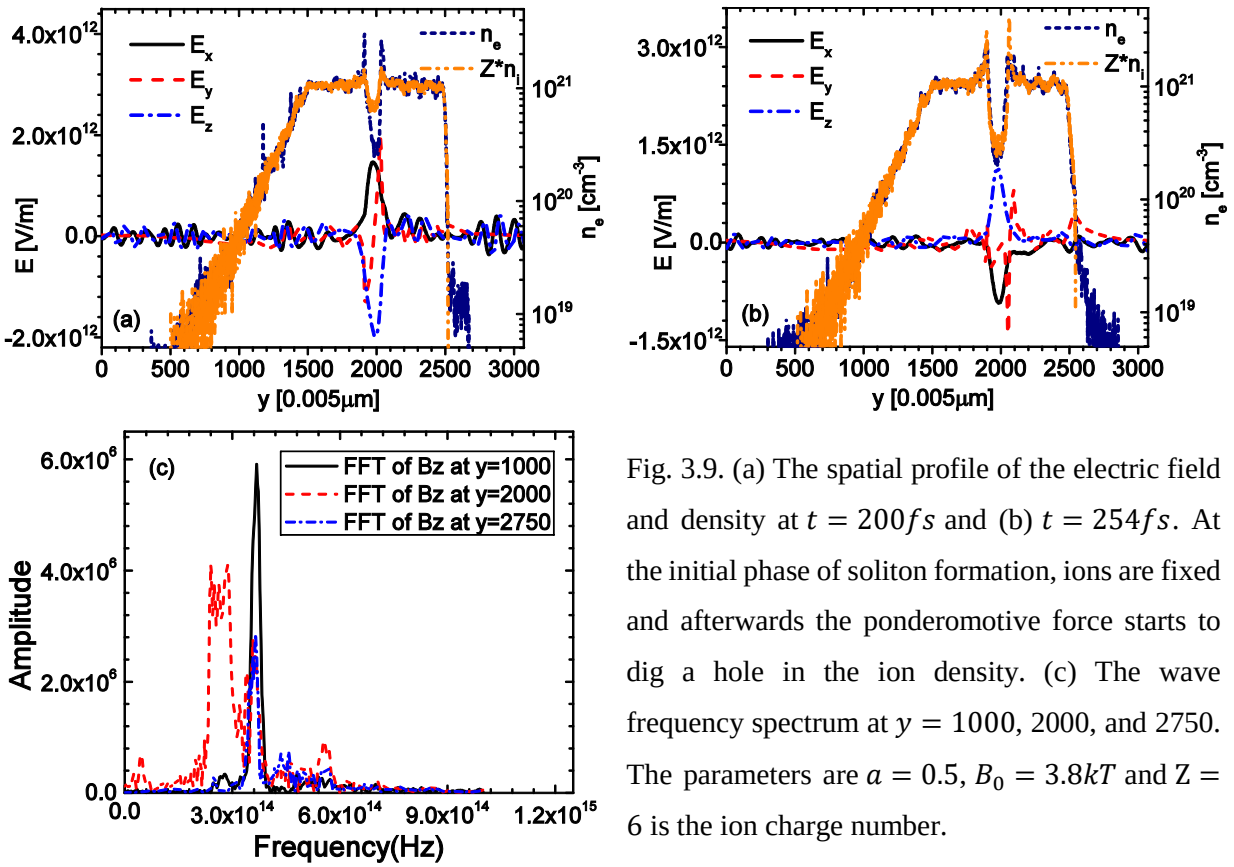

Fig. 3.9. (a) The spatial profile of the electric field and density at $t = 200fs$ and (b) $t = 254fs$. At the initial phase of soliton formation, ions are fixed and afterwards the ponderomotive force starts to dig a hole in the ion density. (c) The wave frequency spectrum at $y = 1000$, 2000, and 2750. The parameters are $a = 0.5$, $B_0 = 3.8kT$ and Z = 6 is the ion charge number.

3.3.2 Soliton spectra

To study in detail about the soliton structures, we have plotted in Fig. 3.9 (a) and (b) the spatial profiles of the electric fields and densities for $a = 0.5$ and $B_0 = 3.8kT$. It can be seen that, at the initial phase of the soliton formation, only the electrons are able to response to the field and there is strong electrostatic field inside the soliton. Afterwards, the ponderomotive force starts to dig a hole in the ion density and the quasi-neutrality state is achieved. In Fig. 3.9(c), the frequency spectra of the laser field at y =1000, 2000 and 2750 are analyzed. At $y = 1000$ and 2750, there is only one peak round the incident laser frequency. However, a broad lower frequency spectrum appears besides the laser frequency at y =2000. Note that the intensity of this low frequency peak is higher than that of the incident laser frequency. Meanwhile, the intensities corresponding to the laser frequency at $y = 2000$ and 2750 have almost the same level. Hence, the results show that while small part of the incident laser propagates through the plasma, the major part is converted into a standing solitary wave. Notice that the solitons have harmonic frequencies.

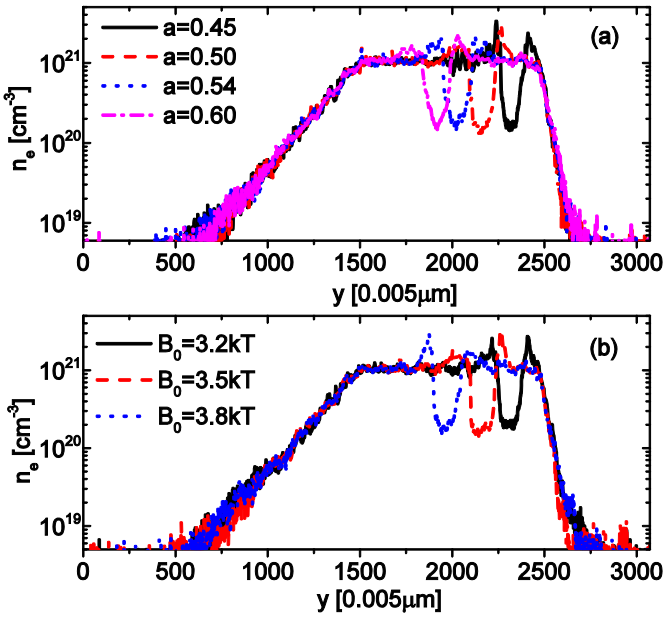

Fig. 3.10. The soliton positon dependence on the laser intensity (a) and magnetic field strength (b). In (a) $B_0 = 3.5kT$, and in (b) $a = 0.5$.

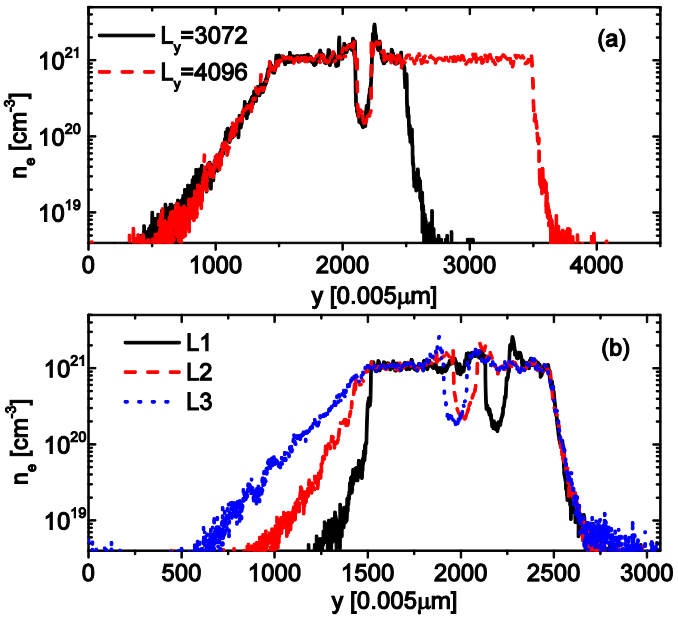

Fig. 3.11. The soliton positon dependence on uniform plasma length (a) and characteristic length of the pre-plasma (b). The parameters are $a = 0.5$, $B_0 = 3.5kT$ for (a) and $B_0 = 3.8kT$ for (b). "L1", "L2" and "L3" in (b) represent the cases without pre-plasma, with pre-plasma of characteristic length 82 and 164, respectively.

3.3.3 Soliton position

The soliton position in the uniform density area is an interesting and meaningful issue, since we may potentially use the soliton generation to control the energy deposition position in the plasmas. Some factors relevant to the soliton position are studied as shown in Fig. 3.10 and Fig. 3.11. Fig. 3.10 shows the soliton position dependence on the laser intensity and magnetic field. The soliton position shifts from the rear boundary to the front one when one increases the laser intensity or magnetic field. This may result from the

dependence of the frequency downshift on the magnetic field and laser intensity, which may be characterized by a threshold for the soliton formation: one of the two factors increases, the other needed for soliton generation decreases. On the other hand, we have extended the system size to $L_y = 4096$ and changed the characteristic length of the pre-plasma, as shown in Fig. 3.11. The "L1", "L2" and "L3" in Fig. 3.11(b) represent the cases without pre-plasma, with pre-plasma of characteristic length 82 and 164, respectively. It is observed that the soliton position is independent of the system size, but shifts towards the front boundary as the characteristic length of the pre-plasma increases. The detailed mechanism of the soliton positon on the density profile still remains unknown and needs to be resolved in the future.

The dependence of soliton position on laser intensity and magnetic field helps us to understand the shape of the curve for $B_0 = 10kT$ in Fig. 3.2(b), where it starts like a soliton induced enhanced heating region but shifts to ECRH. Generally, there are two mechanisms contributing for the heating: ECRH and the soliton induced enhanced heating. When the laser intensity is weak, both the ECRH heating and the enhanced heating is small. (The magnetic field for ECRH is about 13kT, which is larger than 10kT). As the laser intensity increases, the nonlinear effect or soliton induced enhanced heating comes to play. Since the magnetic field is so strong that the soliton position is now expected to be in the pre-plasma area. In fact, we do observe some cavity-like density perturbations in the pre-plasma area around $a = 0.3$ or 0.4 for $B_0 = 10kT$ (which is similar to Fig. 3.8(c)). However, due to the inhomogeneity of pre-plasma, the laser pulse is not well-trapped and these perturbations disappear or move away and they do not develop into the standing cavities as shown in Fig. 3.9(a). Hence, the enhanced soliton heating reduces as the laser intensity increases. However, the ECRH becomes more and more significant since the electron cyclotron frequency decreases due to the relativistic effects.

3.4 Solitons in 2D simulations

We have also studied the soliton dynamics associated with the laser heating efficiency in 2D simulations. The system size in the x direction is extended to 4μm and 8μm to include the transverse effects. The laser pulse is the plane wave and the other parameters are the same as 1D cases. Fig. 3.12 shows the comparison of the heating efficiencies in the 1D and 2D (L_x =4μm) simulations with different magnetic fields for $a = 0.5$. It can be seen that the soliton induced enhanced heating efficiency decreases slightly, however the ECRH efficiency remains the same. In fact, in 2D simulations, the soliton breaks up into some individual small ones soon after its generation. This is different from the 1D case where the soliton can survive for a long time before dissipating in the plasma.

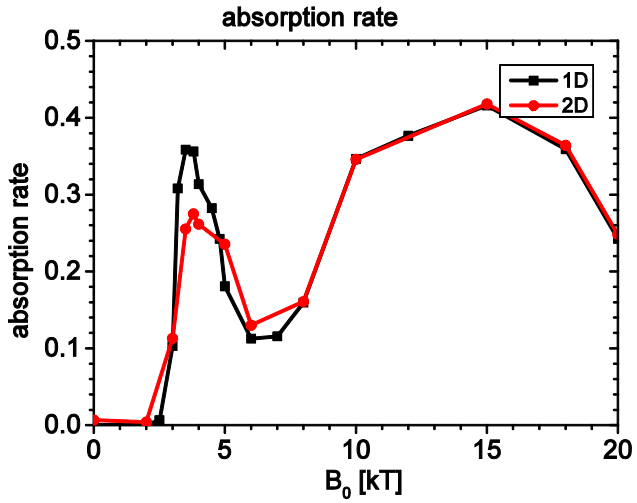

Fig. 3.12. The comparison of heating efficiency in 1D and 2D simulations versus magnetic fields for $a = 0.5$. The system size is 4μm in the x direction for 2D simulations

In Fig. 3.13, we plot the spatiotemporal profiles of the electric field of the solitons for L_x =8μm, where the upper and right subplots correspond to the intersections of the y and x directions, respectively. A strip-like soliton is observed at around $t = 139fs$ at the same positon as in the 1D case (see Fig. 3.7) and after that it breaks into some small ones, as shown by the right subplots in Fig. 3.13(b). The width of these small solitons is about 1.6μm, nearly twice of the laser wavelength and they radiate their energy in the form of electromagnetic wave quickly. Note that, this cloud of soliton formation is different from the solitons in the usual unmagnetized case, where the laser pulse first changes its form due to the nonlinear processes such as self-focusing and energy depletion and afterwards solitons are formed at the position of filaments. In our simulations, a quite uniform strip-like soliton can be obtained at the early time due to the relatively low laser intensity and small solitons are formed probably by some transverse instabilities. Moreover, the 2D simulations with L_x =4μm or 8μm have shown a converged wavelength of the solitons in the *x* direction. Hence, it could be bravely postulated that the 1D model is qualitatively available to explore the soliton dynamics in strongly magnetized plasmas. In the next chapter we will derive the coupled soliton equations in the 1D geometry.

3.5 Summary

In this chapter, the absorption mechanism and various propagation modes of the laser pulse under different laser intensities in strongly magnetized plasma have been studied based on PIC simulations and theoretical analyses. Results generally show that Faraday rotation can take places in weakly magnetized plasmas and the polarized laser wave may convert into an electron cyclotron mode as the magnetic field increases. For linearly polarized incident laser, the polarization changes with both the electron density and magnetic field

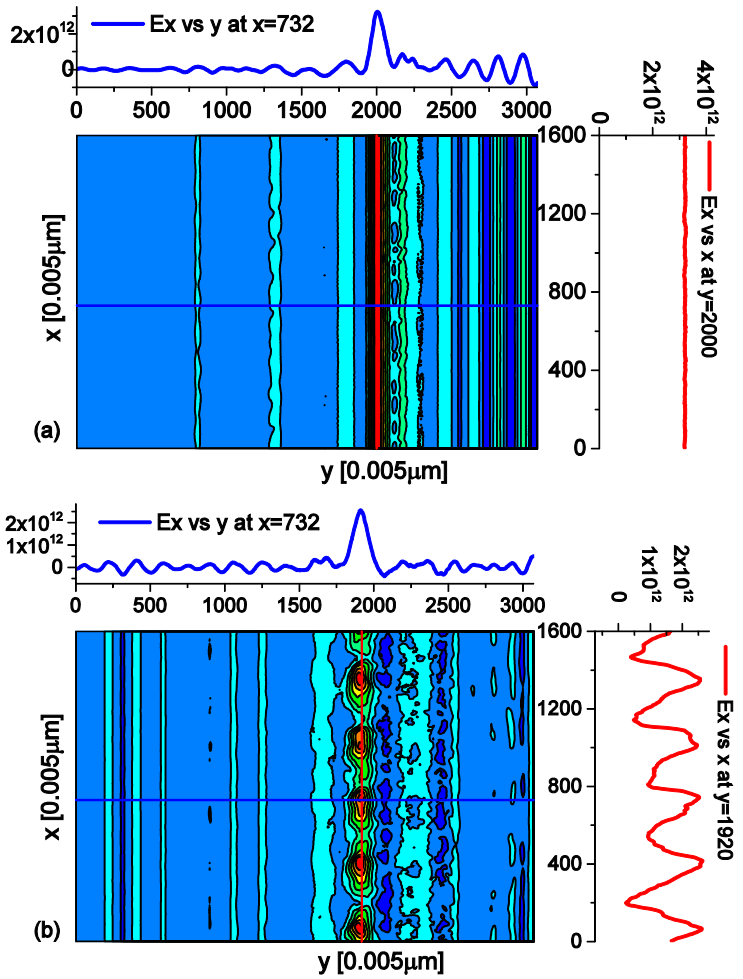

Fig. 3.13. The generation of the solitons with $a = 0.5$ and $B_0 = 3.8kT$ in the 2D simulations for $L_x = 8\mu m$ at (a) $t = 139fs$; and (b) $t = 157fs$. The top suplot in (a) and (b) correspond to $x = 732$ and the right subplot in (a) and (b) correspond to y =2000 and 1920, respectively

due to the different decay rates of the LCP and RCP components. As a result, the laser heating efficiency strongly depends on the magnetic field. Most interestingly, it is found that for some certain magnetic fields and laser intensities, a solitary wave with a very short width and a lower frequency compared to the incident laser may be formed in a density well, which can greatly enhance the absorption of the laser energy. 2D simulations also confirmed this enhancing effect. As the magnetic field increases, the parametric window for the solitons moves towards the lower laser intensity. This may result from the frequency downshift due to the nonlinear effects. Once the laser frequency falls below the plasma frequency, the laser pulse becomes trapped in the density cavity, forming a solitary wave.

The soliton properties and some relevant factors to soliton position are also studied. It is found that the soliton position depends on the characteristic length of the pre-plasma rather than the uniform plasma length. Furthermore, the soliton position moves from the rear boundary to the front one as the laser intensity or magnetic field increases. In 1D simulations, the soliton is of long-living time, however in 2D simulations the soliton can break up into some individual small ones soon after its generation. As a result, the heating

efficiency decreases compared with the 1D simulations. Considering the high efficiency of energy transfer by the solitons, the soliton generation in strongly magnetized plasmas may play an important role in fast ignition, laser-plasma based particle acceleration as well as other potential applications.

4. Soliton equations in magnetized plasmas

In this chapter, we deduce the coupled soliton equations in magnetized plasmas with finite temperature and ion's effects taken into account. The soliton is treated in the framework of relativistic fluid model, where the scalar potential φ, the vector potential $\boldsymbol{A}$ and the phase modulation θ are used to describe the longitudinal and transverse waves with appropriate boundary conditions. The Hamiltonian of the system is obtained and different dispersion relations for the bright and dark solitons are derived according to the boundary conditions. Based on the dynamical systems theory, the soliton solutions in phase space are actually the homoclinic or heteroclinic orbits of the four-dimensional $(A, A', \varphi, \varphi')$ reversible autonomous Hamiltonian system. Since the homoclinic or heteroclinic orbits lie in the intersection of the stable and unstable manifolds of the same or different fixed point(s), the general criterion for the existence of solitons is obtained. In this chapter, the theory of dynamical systems as well as the concepts of some important terminologies, e.g. the fixed point, bifurcation, homoclinic and heteroclinic orbit, stable and unstable manifold, are introduced.

4.1 Coupled soliton equations

The coupled soliton equations can be derived from the Maxwell equations (Coulomb gauge $\nabla \cdot \mathbf{A} = 0$) and the fluid equations,

$$\Delta\varphi = -4\pi(n_e q_e + n_i q_i); \tag{4.1}$$

$$\Delta\boldsymbol{A} - \frac{1}{c^2}\frac{\partial^2 \boldsymbol{A}}{\partial t^2} - \frac{1}{c}\frac{\partial}{\partial t}\nabla\varphi = -\frac{4\pi}{c}(n_e q_e \boldsymbol{v}_e + n_i q_i \boldsymbol{v}_i); \tag{4.2}$$

$$\frac{\partial \boldsymbol{P}_s}{\partial t} = -\nabla(q_s\varphi + \gamma_s m_s c^2) + \boldsymbol{v}_s \times [\nabla \times \boldsymbol{P}_s] + \frac{q_s}{c}\boldsymbol{v}_s \times \boldsymbol{B}_0 - m_s \boldsymbol{v}_{ts}^2 \nabla \ln n_s; \tag{4.3}$$

$$\frac{\partial n_s}{\partial t} + \nabla \cdot (n_s \boldsymbol{v}_s) = 0. \tag{4.4}$$

Here $\boldsymbol{P}_s = \boldsymbol{p}_s + (q_s\boldsymbol{A}) \,/\, c$ is the canonical momentum for s species ($s = e, i$). $\boldsymbol{A}$ and φ are the vector and scalar potential, and n_s, m_s, q_s, γ_s, $\boldsymbol{p}_s$, $\boldsymbol{v}_s$, $\boldsymbol{v}_{ts}$, are the density, mass, electrical quantity, relativistic factor, kinetic momentum, velocity and thermal velocity, respectively. $\boldsymbol{B}_0$ is the ambient magnetic field and c is

the speed of light. $q_e = -e, q_i = e$. Assuming the wave propagation and external magnetic field $\boldsymbol{B}_0$ are along the x direction and in y and z directions the system is uniform, then $\partial_y = \partial_z = 0$. For localized soliton wave, the Coulomb gauge gives $A_x = 0$. The transverse component of Eq. (4.2) becomes,

$$\frac{\partial^2 A_\perp}{\partial x^2} - \frac{1}{c^2}\frac{\partial^2 A_\perp}{\partial t^2} = \frac{4\pi e}{c}(n_e v_{e\perp} - n_i v_{i\perp}). \tag{4.5}$$

The subscript "$\perp$" stands for the transverse components $f_\perp = f_y + if_z$ with $f = A, p_s, v_s$ and P_s. The longitudinal and transverse components of Eq. (4.3) are,

$$\frac{\partial p_{sx}}{\partial t} = -\frac{\partial}{\partial x}(q_s\varphi + \gamma_s m_s c^2) + \frac{1}{2}\left(\frac{p_{s\perp}}{\gamma_s m_s}\frac{\partial P_{s\perp}^*}{\partial x} + \frac{p_{s\perp}^*}{\gamma_s m_s}\frac{\partial P_{s\perp}}{\partial x}\right) - m_s v_{ts}^2\frac{\partial \ln n_s}{\partial x}; \tag{4.6}$$

$$\frac{\partial}{\partial t}\left(p_{s\perp} + \frac{q_s}{c}A_\perp\right) = -v_{sx}\left[\frac{\partial}{\partial x}\left(p_{s\perp} + \frac{q_s}{c}A_\perp\right)\right] - iB_0\frac{q_s}{c}\frac{p_{s\perp}}{\gamma_s m_s}. \tag{4.7}$$

Here the superscript "$*$" represents the conjugate. The soliton solution can be generally expressed as,

$$A_\perp \sim A(\xi)exp[i\omega\tau + i\theta(\xi)], p_{s\perp} \sim p_{s\perp}(\xi)exp[i\omega\tau + i\theta(\xi)]\ and\ \varphi \sim \varphi(\xi)$$

with $\xi = x - Vt$ and $\tau = t - kx/\omega$, where V is a velocity (for bright solitons it is the group velocity however for dark solitons it is not) and k, ω are the soliton wavenumber and frequency and $\theta(\xi)$ is the phase modulation. Note that this kind of solution requests the solitons to be right hand circularly polarized. Eqs. (4.4) and (4.6) give two integrals of motion,

$$\frac{\partial}{\partial \xi}[n_s(-V + v_{sx})] = 0 \tag{4.8}$$

$$\frac{\partial}{\partial \xi}(q_s\varphi + \gamma_s m_s c^2 - Vp_{sx} + m_s v_{ts}^2 ln n_s) - \left|\frac{p_{s\perp}}{\gamma_s m_s}\frac{\partial P_{s\perp}^*}{\partial \xi}\right| = 0 \tag{4.9}$$

The real and imaginary parts of Eq. (4.7) are,

$$(-V + v_{sx})\frac{\partial}{\partial \xi}\left(p_{s\perp} + \frac{q_s}{c}A\right) = 0; \tag{4.10}$$

$$(-V + v_{sx})\left(p_{s\perp} + \frac{q_s}{c}A\right)\frac{\partial \theta}{\partial \xi} + \omega\left(1 - v_{sx}\frac{k}{\omega}\right)\left(p_{s\perp} + \frac{q_s}{c}A\right) = -B_0\frac{q_s}{c}\frac{p_{s\perp}}{\gamma_s m_s} \tag{4.11}$$

For unmagnetized plasma, the canonical momentum in transverse direction is conserved, e.g. $p_{s\perp} + q_s A/c \equiv 0$ and the soliton can have different propagating velocities. However, for magnetized plasma, we choose $V = v_{sx}$ from Eqs. (4.10) and (4.11), which means the particles are traveling with the solitons in the

propagation direction. This condition implies the solitons are of the standing type in the reference frame moving with the plasmas. For static plasmas, $V = 0$. Eqs. (4.9) and (4.11) can be written as,

$$\frac{q_s\varphi}{m_sc^2} + \gamma_s\left(1 - \frac{V^2}{c^2}\right) + \frac{v_{ts}^2}{c^2} ln\frac{n_s}{n_0} + \frac{1}{2}\left(\frac{p_{s\perp}}{\gamma_s m_s c}\right)^2 \frac{q_sB_0/m_sc}{\omega - kV} = const; \tag{4.12}$$

$$\omega\left(1 - V\frac{k}{\omega}\right)\left(p_{s\perp} + \frac{q_s}{c}A\right) = -\frac{q_sB_0}{m_sc}\frac{p_{s\perp}}{\gamma_s}. \tag{4.13}$$

Here n_0 is the unpertubed plasmas density. Eq. (4.12) describes the force balance among the ponderomotive force, the thermal pressure and the electrostatic field in the longitudinal direction. If $V = 0$, it is reduced to Rao's result.[77] Note that the ponderomotive force density in magnetized plasmas is,

$$F = -m_sc^2\nabla\left[\gamma_s(1 - v_{sx}^2/c^2) + \frac{1}{2}\frac{q_sB_0/m_sc}{\omega - kv_{sx}}\left(\frac{p_{s\perp}}{\gamma_s m_s c}\right)^2\right]. \tag{4.14}$$

For $v_{sx} = 0$ and unmagnetized plasmas, it gives the well-known result $F = -m_sc^2\nabla\gamma_s$ as shown in Eq. (1.6). The wave propagation Eq. (4.5) is also separated into the real and imaginary parts,

$$\left(1 - \frac{V^2}{c^2}\right)(2A'\theta' + \theta''A) - 2\omega\left(\frac{k}{\omega} - \frac{V}{c^2}\right)A' = 0; \tag{4.15}$$

$$\left(1 - \frac{V^2}{c^2}\right)(A'' - A\theta'^2) + 2\omega\left(\frac{k}{\omega} - \frac{V}{c^2}\right)\theta'A - \left(\frac{k^2}{\omega^2} - \frac{1}{c^2}\right)\omega^2A = \frac{4\pi e}{c}\left(n_e\frac{p_{e\perp}}{r_em_e} - n_i\frac{p_{i\perp}}{r_im_i}\right). \tag{4.16}$$

Here the superscript " $'$ " denotes the derivation with respect to ξ. Integrating Eqs. (4.15) once, we obtain,

$$\theta' = \bar{k}\left(1 - \frac{A_0^2}{A^2}\right); \tag{4.17}$$

$$\left(1 - \frac{V^2}{c^2}\right)\left\{A'' + \left[\frac{\bar{\omega}^2}{c^2} - \bar{k}^2\left(\frac{A_0^2}{A^2}\right)^2\right]A\right\} = \frac{4\pi e}{c}\left(n_e\frac{p_{e\perp}}{r_em_e} - n_i\frac{p_{i\perp}}{r_im_i}\right). \tag{4.18}$$

with $\bar{k} = \gamma_0^2(k - V\omega/c^2)$, $\bar{\omega} = \gamma_0^2(\omega - kV)$ and $\gamma_0 = (1 - V^2/c^2)^{-1/2}$. Here the boundary conditions $Q_0^{\pm}(A, A', \varphi, \varphi') = (\pm A_0, 0, 0, 0)$ at $\xi \to -\infty$ are adopted. For simplicity, in the following we use the symbol $Q_0^{\pm}$ to represent the boundary conditions. Note that Eq. (4.17) is decoupled from Eq. (4.18) and the phase modulation becomes constant at $\xi \to -\infty$. Using ω_{pe}^{-1}, ω_{pe}^{-1}, n_0, c, m_sc, m_ec^2/e to normalize the time, space, density, velocity, momentum and potential, where $\omega_{pe}^2 = 4\pi n_0e^2/m_e$ is the unperturbed plasma frequency, we rewrite Eqs. (4.1), (4.12), (4.13), (4.17) and (4.18) as,

$$\theta' = \bar{k}\left(1 - \frac{a_0^2}{a^2}\right); \tag{4.19}$$

$$\varphi'' = n_e - n_i; \tag{4.20}$$

$$a'' + \left(\bar{\omega}^2 - \bar{k}^2\frac{a_0^4}{a^4}\right)a = \gamma_0^2\left(n_e\frac{p_{e\perp}}{r_e} - n_i\frac{p_{i\perp}}{r_i}\right); \tag{4.21}$$

$$p_{e\perp} - a = \bar{\alpha}\gamma_0^2\frac{p_{e\perp}}{\gamma_e}; \qquad p_{i\perp} + \rho a = -\rho\bar{\alpha}\gamma_0^2\frac{p_{i\perp}}{\gamma_i} \tag{4.22}$$

$$v_{te}^2\ln n_e = \varphi + \frac{1}{2}\bar{\alpha}\gamma_0^2\frac{p_{e\perp}^2}{\gamma_e^2} - \frac{\gamma_e}{\gamma_0^2} - c_{e0}; \quad v_{ti}^2\ln n_i = -\rho\varphi - \frac{1}{2}\rho\bar{\alpha}\gamma_0^2\frac{p_{i\perp}^2}{\gamma_i^2} - \frac{\gamma_i}{\gamma_0^2} - c_{i0}. \tag{4.23}$$

Here $a = eA/(m_e c^2)$, $a_0 = eA_0/(m_e c^2)$, $\gamma_s = \gamma_0(1 + p_{s\perp}^2)^{-1/2}$, $\bar{\alpha} = \omega_{ce}/\bar{\omega}$, $\omega_{ce} = eB_0/(m_e c)$, $\rho = m_e/m_i$, $c_{e0} = \bar{\alpha}\gamma_0^2 p_{e0\perp}^2/(2\gamma_{e0}^2) - \gamma_{e0}/\gamma_0^2$ and $c_{i0} = -\rho\bar{\alpha}\gamma_0^2 p_{i0\perp}^2/(2\gamma_{i0}^2) - \gamma_{i0}/\gamma_0^2$. γ_{s0} and $p_{s0\perp}$ are the relativistic factor and transverse momentum for the electron and ion at the left boundary $\xi \to -\infty$. Notice that $\bar{\alpha}$ can be negative, which means the magnetic field is opposite to the laser propagation direction. The above equations together with the boundary conditions $Q_0^{\pm}$ give the whole description of soliton formation in magnetized plasmas.

4.2 Dispersion relation for bright and dark soliton

The dispersion relation of the bright and dark soliton is different due to the boundary conditions. For bight solitons $a_0 = 0$, $\theta = \bar{k}\xi + \theta_0$. The total wave phase has the simple form $\exp[i\bar{\omega}(t - xV/c^2) + i\theta_0]$. Hence, the actual wavenumber of the soliton is $k = \bar{\omega}V/c^2$. Using $\bar{\omega} = \gamma_0^2(\omega - kV)$, we find $\bar{\omega} = \omega$, $\bar{k} = 0$ and $\bar{\alpha} = \omega_{ce}/\omega \equiv \alpha$. To distinguish the bright and dark solitons, from now on we use the symbols without "$-$" for bright solitons and symbols with "$-$" for dark solitons. Similarly, the boundary condition Q_0 is for bright solitons and $Q_0^{\pm}$ are for dark solitons. The Maxwell-fluid model only admits bright solitons with normalized dispersion relation,

$$V\omega = k. \tag{4.24}$$

Note that the boundary condition $Q_0(a, a', \varphi, \varphi') = (0,0,0,0)$ is also a trivial solution to the system. Hence Q_0 is the equilibrium or fixed point (determined by $a' = a'' = \varphi = \varphi'' = 0$). In the real space, the soliton envelop goes from zero (left boundary) to a maximum and return to zero (right boundary); correspondingly in the phase space the solution starts from the fixed point Q_0 and returns to Q_0. Mathematically, the bright soliton solution represents a homoclinic orbit which connects the fixed point to itself.

For dark solitons, $a_0 \neq 0$, the soliton can have nonlinear phase modulation given by Eq. (4.19). If we assume the boundary $Q_0^{\pm} = (\pm a_0, 0,0,0)$ is also the fixed point of the system, we have,

$$\bar{\omega}^2 = \bar{k}^2 + \frac{\gamma_0^2}{\gamma_{e0} - \bar{\alpha}\gamma_0^2} + \frac{\rho\gamma_0^2}{\gamma_{i0} + \rho\bar{\alpha}\gamma_0^2} \tag{4.25}$$

The physical meaning of Eq. (4.25) is clear if we write the dispersion relation in the laboratory frame,

$$\omega^2 = k^2 + \frac{1}{\gamma_{e0} - \omega_{ce}/(\omega - kV)} + \frac{\rho}{\gamma_{i0} + \omega_{ci}/(\omega - kV)}. \tag{4.26}$$

Here $\omega_{ci} = \rho\omega_{ce}$ is the ion cyclotron frequency. Hence, Eq. (4.25) describes a right hand circularly polarized wave in magnetized plasmas with relativistic electron and ion effects. Since $\gamma_{e0} > \gamma_0$, if we neglect the ion's effects, Eq. (4.25) implies,

$$\gamma_0 \left(\bar{\alpha} + \frac{1}{\bar{\omega}^2 - \bar{k}^2}\right) > 1. \tag{4.27}$$

Only solitons with $\bar{\omega}$ and $\bar{k}$ satisfying inequality (4.27) are physically meaningful. For the dark soliton, the solution starts from $Q_0^{\pm}$ (left boundary) and ends at $Q_0^{\pm}, Q_0^{\mp}$ or other fixed point (right boundary) which depends on whether the solution is symmetric, antisymmetric or asymmetric. Hence, dark soliton solution represents a homoclinic (or heteroclinic) orbit which connects the same (or different) fixed point(s). Furthermore, it is easy to prove that for each $Q_0^+ - Q_0^-$ connection, there exists a counterpart $Q_0^- - Q_0^+$ one.

4.3 Hamiltonian and dynamical systems theory

To have an overview of the solutions in phase space, it is better to use the Hamiltonian of the system. The Hamiltonian H can be derived by integrating Eqs. (4.20), (4.21) once.

4.3.1 Hamiltonian and symmetry

Integrating Eqs. (4.20) and (4.21), we find the Hamiltonian, (see Appendix A)

$$H(a, a', \varphi, -\gamma_0^2\varphi') = \frac{1}{2}\left(a'^2 + \bar{\omega}^2 a^2 + \bar{k}^2\frac{a_0^4}{a^2} - \gamma_0^2\varphi'^2\right) + \gamma_0^2\left[v_{te}^2(n_e - 1) + \frac{v_{ti}^2}{\rho}(n_i - 1)\right]. \tag{4.28}$$

Here $Q_{a,\varphi} = a, \varphi$ are the generalized coordinates and $P_{a,\varphi} = a', -\gamma_0^2\varphi'$ are the corresponding generalized momenta. They satisfy the Hamilton's equations $dQ/d\xi = \partial H/\partial P$ and $dP/d\xi = -\partial H/\partial Q$. Since H does not depend on ξ explicitly, the system is autonomous or $H \equiv H_0$.

The symmetry of the system can help us to get some information about the soliton solutions. First, H is invariant under the reflection symmetry, $a \to -a$, $a' \to -a'$, $\varphi \to \varphi$ and $\varphi' \to \varphi'$. Hence, if $(a(\xi), \varphi(\xi))$ is a solution, $(-a(\xi), \varphi(\xi))$ is also a solution. In other words, for any homoclinic orbit $Q_0^+ - Q_0^+$ there exists an identically shaped $Q_0^- - Q_0^-$ one. Second, note that H is ξ-reversible, e.g. invariant under simultaneously changing the sign of ξ and the generalized momenta a', $-\gamma_0^2\varphi'$. As a result, $(a(-\xi), \varphi(-\xi))$ is a solution too. Thus, homoclinic orbit $Q_0^\pm - Q_0^\pm$ can either be symmetric $(a(\xi) = a(-\xi), \varphi(\xi) = \varphi(-\xi))$ or come in asymmetric pairs with ξ-reversal; heteroclinic orbit $Q_0^\pm - Q_0^\mp$ can either be antisymmetric $(-a(\xi) = a(-\xi), \varphi(\xi) = \varphi(-\xi))$ or come in asymmetric pairs with ξ-reversal.

For autonomous Hamiltonian systems, it is well known that the trajectories in phase space of the same Hamilton value don't intersect expect at the fixed points. Hence, it is important to figure out the existence and properties of the fixed points.

4.3.2 Fixed points and bifurcations

The soliton equations (4.19) ~ (4.23) can be written in the form of a system of ordinary differential equations,

$$\frac{d\boldsymbol{x}}{d\xi} = f(\boldsymbol{x}). \tag{4.29}$$

Here $\boldsymbol{x} = (a, a', \varphi, \varphi')$. Then the fixed points are determined by $f(\boldsymbol{x}) = 0$, which yields $n_e = n_i = n$ with a, φ, n satisfying,

$$\left(\bar{\omega}^2 - \bar{k}^2\frac{a_0^4}{a^4}\right)a = n\left(\frac{\gamma_0^2}{\gamma_e - \bar{\alpha}\gamma_0^2} + \frac{\rho\gamma_0^2}{\gamma_i + \rho\bar{\alpha}\gamma_0^2}\right)a \tag{4.30}$$

$$\frac{c_s^2}{v_{ti}^2 v_{te}^2}\varphi = -\frac{1}{v_{te}^2}\left(\frac{1}{2}\alpha\gamma_0^2\frac{p_{e\perp}^2}{\gamma_e^2} - \frac{\gamma_e}{\gamma_0^2} - c_{e0}\right) + \frac{1}{v_{ti}^2}\left(-\frac{1}{2}\rho\alpha\gamma_0^2\frac{p_{i\perp}^2}{\gamma_i^2} - \frac{\gamma_i}{\gamma_0^2} - c_{i0}\right) \tag{4.31}$$

$$c_s^2 \ln n = \rho\left(\frac{1}{2}\bar{\alpha}\gamma_0^2\frac{p_{e\perp}^2}{\gamma_e^2} - \frac{\gamma_e}{\gamma_0^2} - c_{e0}\right) + \left(-\frac{1}{2}\rho\bar{\alpha}\gamma_0^2\frac{p_{i\perp}^2}{\gamma_i^2} - \frac{\gamma_i}{\gamma_0^2} - c_{i0}\right) \tag{4.32}$$

Here c_s is the ion acoustic velocity with $c_s^2 = \rho v_{te}^2 + v_{ti}^2$. Obviously Q_0 ($Q_0^\pm$) is the fixed point. Since Eqs. (4.30) - (4.32) are symmetric for a, there may exist other even number solutions and we regard them as $Q_*^\pm(\pm a^*, 0, \varphi^*, 0)$. Note that at the fixed points Q_0 or $Q_*^\pm$, the plasma is neutral. Taking the derivative of Eq. (4.32) with respect of a, we find,

$$\gamma_0^2 c_s^2\frac{\partial n}{\partial a} = -\rho n\gamma_0^2\left(\frac{p_e}{\gamma_e} - \frac{p_i}{\gamma_i}\right) = -\rho\left(\bar{\omega}^2 - \bar{k}^2\frac{a_0^4}{a^4}\right)a.$$

Hence at the fixed points the density is,

$$n = 1 - \frac{\rho}{2\gamma_0^2 c_s^2}\left(\bar{\omega}^2 a^2 + \bar{k}^2 \frac{a_0^4}{a^2}\right) \tag{4.33}$$

Now let's discuss the existence condition for $Q_*^{\pm}$. Assuming ion is nonrelativistic, for the bright soliton we find $Q_*^{\pm}$ exists if $\gamma_0\alpha$ is in the following interval (see Appendix B.1),

$$\begin{cases} -1/\rho < \alpha\gamma_0 < \infty & \text{when } \omega^2 \le \dfrac{4\gamma_0\rho}{1+\rho}; \\ -1/\rho < \alpha\gamma_0 < \beta_-, \quad \beta_+ < \alpha\gamma_0 < \infty & \text{when } \omega^2 > \dfrac{4\gamma_0\rho}{1+\rho}. \end{cases} \tag{4.34}$$

Here $\beta_\pm = \left[\rho - 1 \pm \sqrt{(\rho+1)^2 - 4\rho(\rho+1)\gamma_0/\omega^2}\right]/(2\rho)$. In the limit of immobile ions ($\rho \to 0$), $\beta_+ = 1 - \gamma_0/\omega^2$ and condition (4.34) is reduced to $1 - \gamma_0/\omega^2 < \alpha\gamma_0 < \infty$. Eq. (4.30) has the exact solution for bright solitons,

$$\begin{cases} a^* = \pm\left[\dfrac{\gamma_0^2}{\omega^4} - \dfrac{1}{(1+\alpha\omega^2)^2}\right]^{-1/2} \\ \varphi^* = \dfrac{\alpha}{2} + \dfrac{1}{\omega^2} - \dfrac{1}{\gamma_0} + \dfrac{\alpha\omega^4}{2\gamma_0^2(1+\alpha\omega^2)^2} \end{cases} \tag{4.35}$$

For dark solitons a^* satisfies,

$$a^{*2} = \frac{\gamma_0^2}{\left(\bar{\omega}^2 - \bar{k}^2\, a_0^4/a^{*4}\right)^2} - \frac{1}{\left[\bar{\alpha}\left(\bar{\omega}^2 - \bar{k}^2\, a_0^4/a^{*4}\right) + 1\right]^2} \tag{4.36}$$

Here $a_0^2 = (\gamma_{e0}^2/\gamma_0^2 - 1)(1 - \bar{\alpha}\gamma_0^2/\gamma_{e0})$, $\gamma_{e0} = \gamma_0^2\left[\bar{\alpha} + 1/\left(\bar{\omega}^2 - \bar{k}^2\right)\right]$ and $\bar{\omega}$, $\bar{k}$, $\bar{\alpha}$ should satisfy inequality (4.27). Notice that the dark soliton amplitude at the infinity is totally determined once the magnetic field, soliton frequency and wavenumber are fixed. In Fig. 4.1 we show the fixed points solutions for bright and dark solitons with respect of $\alpha(\bar{\alpha})$, where Q_0 is the blue line and $Q_*^{\pm}$ are the red lines. Mathematically, Fig. 4.1 represents the bifurcation diagram of the system with $\alpha(\bar{\alpha})$ the bifurcation parameter. The bifurcation happens at the point where the number or stability properties of the equilibria change as the system parameters vary [85]. The topology of the phase space is usually different before and after the bifurcation, which will result in dramatic change of the solution structure and properties around the bifurcation. Thus the stability properties or types of the fixed points play an important role in determining the existence of solitons. The fixed point types are determined by the eigenvalues of the Jacobian matrix J at $Q_0, Q_*^{\pm}$,

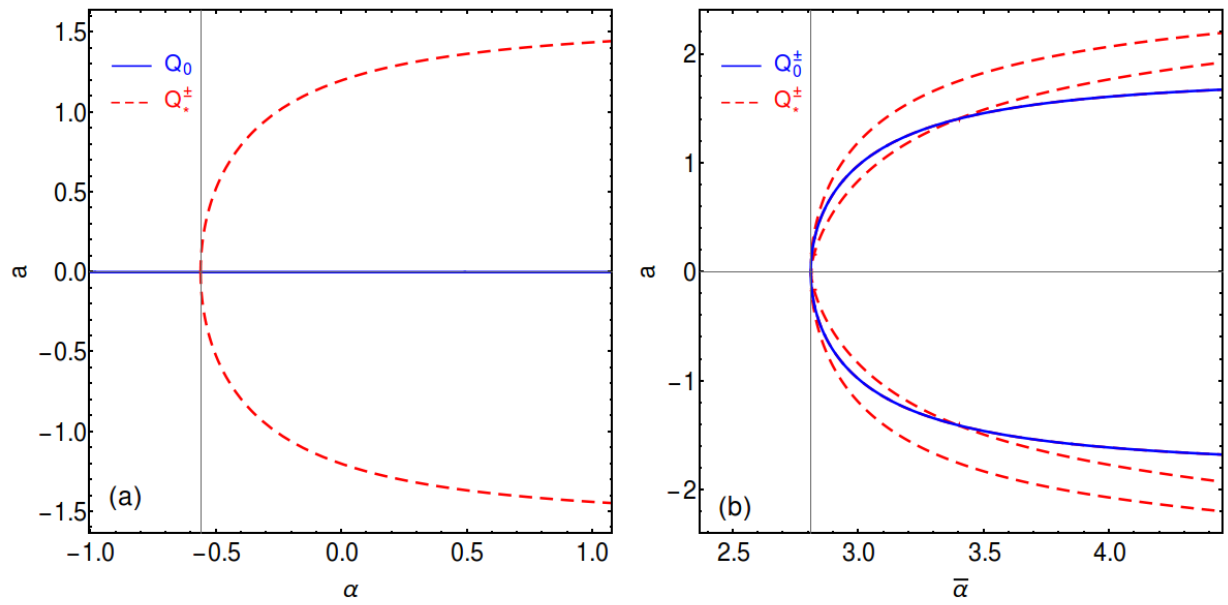

Fig. 4.1. The bifurcation diagram for bright (a) and dark (b) solitons with respect of $\alpha(\bar{\alpha})$ in the immobile ions limit. The parameters are (a) $\omega = 0.8$; (b) $\bar{\omega} = 0.1$, $\bar{k} = 0.75$ and $\gamma_0 = 1$ for all plots.

$$J = \frac{\partial(a', a'', \varphi', \varphi'')}{\partial(a, a', \varphi, \varphi')}_{Q_0, Q_*^{\pm}} = \begin{pmatrix} 0 & 1 & 0 & 0 \\ J_{21} & 0 & J_{23} & 0 \\ 0 & 0 & 0 & 1 \\ J_{41} & 0 & J_{43} & 0 \end{pmatrix} \tag{4.37}$$

Here the nonzero Jacobian matrix components are expressed as,

$$J_{21} = -\left[\left(\bar{\omega}^2 + 3\bar{k}^2 \frac{a_0^4}{a^4}\right) - \frac{n}{\bar{\alpha}}\left(\frac{\gamma_e^3}{\gamma_e^3 - \bar{\alpha}\gamma_0^4} - \frac{\gamma_i^3}{\gamma_i^3 + \rho\bar{\alpha}\gamma_0^4}\right)\right] - n\gamma_0^2\left(\frac{1}{v_{te}^2}\frac{p_{e\perp}^2}{\gamma_e^2} + \frac{\rho}{v_{ti}^2}\frac{p_{i\perp}^2}{\gamma_i^2}\right); \tag{4.38}$$

$$J_{41} = -n\left(\frac{1}{v_{te}^2}\frac{p_{e\perp}}{\gamma_e} + \frac{\rho}{v_{ti}^2}\frac{p_{i\perp}}{\gamma_i}\right); \tag{4.39}$$

$$J_{23} = n\gamma_0^2\left(\frac{1}{v_{te}^2}\frac{p_{e\perp}}{\gamma_e} + \frac{\rho}{v_{ti}^2}\frac{p_{i\perp}}{\gamma_i}\right); \tag{4.40}$$

$$J_{43} = n\left(\frac{1}{v_{te}^2} + \frac{\rho}{v_{ti}^2}\right). \tag{4.41}$$

Note that we have used the condition $a' = 0$ at the fixed points and the relations,

$$
\begin{aligned}
&p'_{e\perp} = \frac{\gamma_e^3}{\gamma_e^3 - \alpha\gamma_0^4}a'; \qquad \gamma'_e = \frac{\gamma_0^2 p_{e\perp}}{\gamma_e}p'_{e\perp}; \qquad \left(\frac{p_{e\perp}}{\gamma_e}\right)' = \frac{\gamma_0^2}{\gamma_e^3}p'_{e\perp}; \\
&p'_{i\perp} = -\frac{\rho\gamma_i^3}{\gamma_i^3 + \rho\alpha\gamma_0^4}a'; \qquad \gamma'_i = \frac{\gamma_0^2 p_{i\perp}}{\gamma_e}p'_{i\perp}; \qquad \left(\frac{p_{i\perp}}{\gamma_i}\right)' = \frac{\gamma_0^2}{\gamma_i^3}p'_{i\perp}.
\end{aligned} \tag{4.42}
$$

The eigenvalues of J are,

$$
\lambda_{1-4}^2 = \pm\sqrt{\frac{1}{2}\left(\delta \pm \sqrt{\Delta}\right)}. \tag{4.43}
$$

with $\delta = J_{21} + J_{43}$, $\Delta = (J_{21} - J_{43})^2 + 4J_{23}J_{41}$. For the convenience of future discussion, we regard $\lambda_{1,3}$ as the eigenvalues with positive real part and $\lambda_{2,4}$ as the eigenvalues with negative real part and $\lambda_1^2 = \lambda_2^2$, $\lambda_3^2 = \lambda_4^2$. The dynamical systems theory [86] states that, 1) when $\Delta > 0$, the fixed point is a focus in the region $\delta < -\sqrt{\Delta} < 0$; a saddle in the region $\delta > \sqrt{\Delta} > 0$; and a saddle-center in the region $|\delta| < \sqrt{\Delta}$; 2) when $\Delta < 0$, the fixed point is a saddle-focus.

4.3.3 Stable and unstable manifolds

In the next, we introduce an important terminology from the theory of dynamical systems: the stable and unstable manifolds. The stable manifold $W^s(Q)$ and unstable manifold $W^u(Q)$ of a fixed point Q is a set of trajectories in phase space which satisfies the following condition,

$$
\begin{aligned}
W^s(Q) &:= \left\{\boldsymbol{x} \in R^4 \middle| \lim_{\xi\to\infty} \phi^\xi(\boldsymbol{x}) = Q\right\} \\
W^u(Q) &:= \left\{\boldsymbol{x} \in R^4 \middle| \lim_{\xi\to-\infty} \phi^\xi(\boldsymbol{x}) = Q\right\}
\end{aligned} \tag{4.44}
$$

Here $\phi^\xi(\boldsymbol{x})$ is the flow of Eq. (4.29) and $\boldsymbol{x} = (a, a', \varphi, \varphi')$**.** Hence, trajectories on the stable or unstable manifold converge to Q at the positive or negative infinity. In our case, the fixed point Q_0 represents the boundary conditions, thus it is obvious that the soliton solutions should on both stable and unstable manifolds. Mathematically, the homoclinic or heteroclinic orbit lies in the intersection of the stable manifold W^s and unstable manifold W^u of the same or different fixed point(s). As a result, from mathematic point of view, solving this set of coupled soliton equation system with boundary conditions $Q_0\left(Q_0^\pm\right)$ is equal to find the homoclinic or heteroclinic orbits of a four-dimensional $(a, a', \varphi, \varphi')$ reversible autonomous Hamiltonian system.

Knowing the manifolds is crucial for understanding the overall dynamics of Eq. (4.29). For example, if the fixed points of are of the saddle type then they come with global stable and unstable manifolds. The

stable manifold may form boundaries of basins of attraction and the intersection of stable and unstable manifold lead to complicated dynamics and chaos.

The stable and unstable manifolds are closely related to the fixed point types. For 4D Hamiltonian system, the stable, unstable and center manifold theorem [85] states that when the fixed point Q is of the saddle or saddle focus types, there is a 2D stable manifold and a 2D unstable manifold in the neighborhood of Q; when Q is of the saddle center type, there is a 1D stable manifold and a 1D unstable manifold; when Q is of the focus type, there is no stable or unstable manifold. Obviously, the existence and dimension of the manifold determine the possibility of the intersection of the stable and unstable manifolds and then the existence of soliton solutions. Since the Hamiltonian is fixed $H(a, a', \varphi, \varphi') = H_0$, the system is actually 3D, e.g. constraint to a 3D energy manifold. Hence, simply counting the dimensions, one find for 2D stable and unstable manifold they are generally expected to intersect in the 3D phase space. Thus soliton solutions are general in the saddle or saddle-focus domain. For 1D stable and unstable manifold, the intersection is rare, e.g. only happens at particular system parameters $(\bar{\alpha}, \bar{\omega}, \bar{k})$. As a result in the saddle-center domain, the solitons will have discrete spectrum $(\bar{\omega}, \bar{k})$ or they do not exist. For the focus domain, it is obvious that there is no soliton solution at all.

For certain conditions as will discussed in the next chapter, the 4D Hamiltonian system can be reduced to 2D. In this case, the fixed point can only be the saddle or center type. There is a 1D stable and unstable manifold in the former case and no stable or unstable manifolds in the latter case. In the saddle regime, the stable and unstable manifolds always intersect in the 2D phase space since they are the same orbit. Hence, for simplified 2D systems, soliton solutions only exist in the saddle regime.

4.4 Summary

In this chapter, the coupled soliton equations (4.19) – (4.23) in magnetized plasmas are derived. The soliton is treated in the framework of relativistic fluid model, where the scalar potential φ, the vector potential $\boldsymbol{A}$ and the phase modulation θ are used to describe the longitudinal and transverse waves with appropriate boundary conditions. In 1D geometry, this model assumes the soliton to be circularly polarized and the amplitude of the potentials $\varphi, \boldsymbol{A}$ and the phase θ only depend on the combination of $\xi = x - Vt$. Substituting this kind of solution into the Maxwell-fluid equations, one can obtain three nonlinear ordinary differential equations for $\varphi, \boldsymbol{A}$ and θ respectively. The equation for θ is decoupled and can be solved once φ and $\boldsymbol{A}$ are known. The potentials $\varphi, \boldsymbol{A}$ are governed by two second order nonlinear differential equations which describe the nonlinear coupling between the longitudinal electrostatic wave and transverse

electromagnetic wave due to the density perturbation and the relativistic effects. This set of equations is solved with zero or non-zero boundary conditions, which correspond to bright or dark solitons, respectively. By assuming appropriate dispersion relations from the boundary conditions, these soliton solutions become the connections between the same or different fixed point(s) of the equation system in the phase space. Using the dynamical systems theory, the existence of soliton solutions to the equations turns out be searching for the homoclinic or heteroclinic orbits of the system. Since these orbits lie in the intersection of the stable and unstable manifolds, the types of the fixed points and associated manifolds play an important role in determining the existence and properties of the solitons. Based on the soliton equations, the general criterion for the existence of solitons is obtained.

5. Bright solitons in magnetized plasmas

From this chapter on, we will systematically analysis the bright and dark soliton formations in cold and warm plasmas, respectively. In this chapter, the bright soliton is studied. The ions are first assumed to be at rest. Based on the discussion in chapter 4, the existence conditions and properties of the bright solitons are investigated. In cold plasmas where the system is reduced to 2-dimensional (2D), an additional restriction on the soliton frequency is obtained from the non-negative condition of the electron density as discussed by Farina et al [78]. However, this restriction disappears in warm plasmas. Then the ion's effects on the soliton properties are investigated through the quasi-neutral approximation. The coupled soliton equations are solved numerically by either the shooting method or the rational spectral algorithm [63, 87]. By the end of the chapter, we describe in detail about the two numerical methods we have employed. For the sake of convenience, we rewrite the bright soliton equations,

$$\varphi'' = n_e - n_i; \tag{5.1}$$

$$a'' + \omega^2 a = \gamma_0^2 \left(n_e \frac{p_{e\perp}}{r_e} - n_i \frac{p_{i\perp}}{r_i} \right) \tag{5.2}$$

$$p_{e\perp} - a = \alpha\gamma_0^2 \frac{p_{e\perp}}{\gamma_e}; \qquad p_{i\perp} + \rho a = -\rho\alpha\gamma_0^2 \frac{p_{i\perp}}{\gamma_i} \tag{5.3}$$

$$v_{te}^2 \ln n_e = \varphi + \frac{1}{2}\alpha\gamma_0^2 \frac{p_{e\perp}^2}{\gamma_e^2} - \frac{\gamma_e}{\gamma_0^2} - c_{e0}; \quad v_{ti}^2 \ln n_i = -\rho\varphi - \frac{1}{2}\rho\alpha\gamma_0^2 \frac{p_{i\perp}^2}{\gamma_i^2} - \frac{\gamma_i}{\gamma_0^2} - c_{i0}. \tag{5.4}$$

Here $\alpha \equiv \omega_{ce}/\omega$ with $\omega_{ce} = eB_0/(m_e c)$ the electron cyclotron frequency and $\rho = m_e/m_i$ the electron-ion mass ratio. $\gamma_0^2 = 1/(1 - V^2/c^2)$. We mention again that ω_{ce} can be negative which means the magnetic field is opposite to the laser propagation direction.

5.1 Bright solitons in cold plasmas

We first discuss the cold plasma case where $v_{te} = 0$. Assuming ion is at rest, then the scalar potential φ and electron density n_e can be eliminated by Eqs. (5.1) and (5.4). The soliton equation and the Hamiltonian $H(a, \gamma_0^2/\gamma_e^2\, a')$ become,

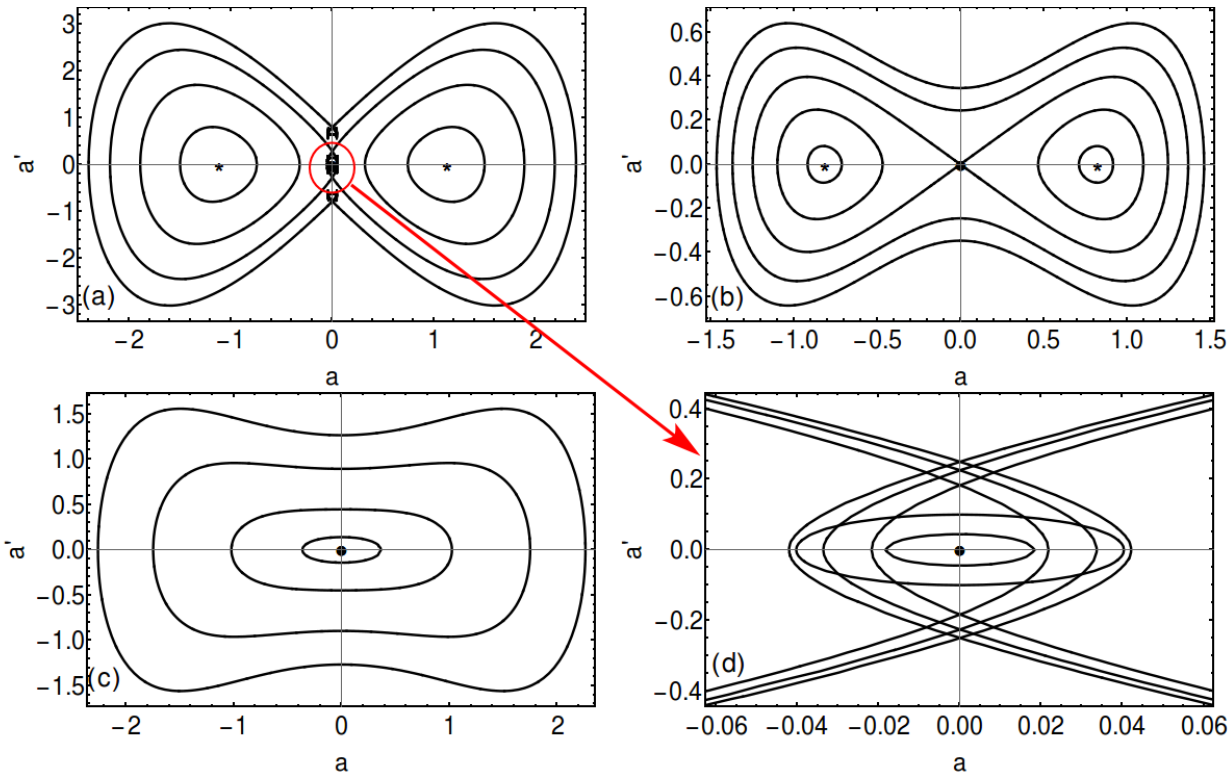

Fig. 5.1: The phase portraits of the system for $\alpha = 1.2$ (a), $\alpha = 0.1$ (b) and $\alpha = -0.5$ (c) with $\omega = 0.9$ and $\gamma_0 = 1$. The enlargement of (a) around Q_0 is shown in (d). The fixed points Q_0 and $Q_*^{\pm}$ are marked by round dot and asterisks, respectively.

$$\frac{\gamma_0^2}{\gamma_e^2}a'' + \omega^2 a = \frac{\gamma_0^2}{r_e - \alpha\gamma_0^2}\left(1 + \frac{\gamma_0^2}{\gamma_e^3 - \alpha\gamma_0^4}a'^2\right)a; \tag{5.5}$$

$$H\left(a, \frac{\gamma_0^2}{\gamma_e^2}a'\right) = \frac{1}{2}\left(\frac{\gamma_0^2}{\gamma_e^2}a'^2 + \omega^2 a^2\right) - \left(\frac{1}{2}\alpha\gamma_0^2\frac{\gamma_0^2}{\gamma_e^2} + \gamma_e\right). \tag{5.6}$$

Here γ_e and a satisfy

$$\gamma_e^2 = \gamma_0^2\left[1 + \frac{\gamma_e^2 a^2}{(\gamma_e - \alpha\gamma_0^2)^2}\right]. \tag{5.7}$$

Now the system is reduced to 2D and the fixed point of the system is either a saddle or a center (see Fig. 5.1). As discussed before, there is a 1D stable and unstable manifold in the former case and a 2D center manifold in the latter case and the solitons only exist in the saddle region.

For unmagnetized plasmas $\alpha = 0$ and $\gamma_e = \gamma_0\sqrt{1 + a^2}$, Eq. (5.5) has an exact standing solution given by [62],

$$a = 2\sqrt{1-\omega^2}\,\frac{\cosh(\sqrt{1-\omega^2}\xi)}{\cosh^2\left(\sqrt{1-\omega^2}\xi\right)+\omega^2-1}. \tag{5.8}$$

For magnetized plasmas, generally it is difficult to solve Eq. (5.5). However, in the ultra-relativistic limit, $\gamma_e \approx \alpha\gamma_0^2 + a\gamma_0$ and in the weakly relativistic limit $\gamma_e^2 \approx \gamma_0^2[1 + a^2/(1-\alpha\gamma_0)^2]$. Hence, Eq. (5.6) can be integrated in terms of the elliptic integrals to obtain an implicit function $\xi = \xi(a)$.

5.1.1 Phase portrait

At the fixed point Q_0 the Jacobian matrix J of the system is,

$$J = \begin{pmatrix} 0 & 1 \\ (\gamma_e^2/\gamma_0^2)\lambda^2 & 0 \end{pmatrix} \text{ with } \lambda^2 = -\omega^2 + \frac{\gamma_0^4}{\gamma_e^3 - \alpha\gamma_0^4} \tag{5.9}$$

Here $\gamma_e = \gamma_0$ at $Q_0(0,0)$ and $\gamma_e = \gamma_0^2(\alpha + 1/\omega^2) > \gamma_0$ at $Q_*^{\pm}(\pm a^*, 0)$ with a^* given by Eq. (4.35).

Notice that $Q_*^{\pm}$ exist only when $\alpha\gamma_0 > 1 - \gamma_0/\omega^2$. In this region, $Q_*^{\pm}$ are always centers since we have $\gamma_e^3 > \gamma_e\gamma_0^2 = \alpha\gamma_0^4 + \gamma_0^4/\omega^2$, thus $\lambda^2 < 0$. On the other hand, for fixed point Q_0 it is either a saddle type ($\lambda^2 > 0$) or a center ($\lambda^2 < 0$) type. Hence, the existence condition for bright soliton is,

$$1 - \frac{\gamma_0}{\omega^2} < \alpha\gamma_0 < 1 \tag{5.10}$$

In Fig. 5.1, we plot the phase portraits of Eq. (5.6) for various magnetic fields, where Q_0 and $Q_*^{\pm}$ are marked by round dot and asterisks, respectively. The structure around the origin in Fig. 5.1(a) is enlarged and displayed in Fig. 5.1(d). Notice that there is a singularity at $\gamma_e = \alpha\gamma_0^2$ in Eq. (5.5) when $\alpha\gamma_0 > 1$, which corresponds to the $a = 0$ axis in Fig. 5.1(a). Table 5.1 summarizes the fixed point types for different magnetic fields.

Table. 5.1. The fixed point types for different magnetic fields.

	Q_0	$Q_*^{\pm}$
$\alpha\gamma_0 > 1$	center	center
$1 - \gamma_0/\omega^2 < \alpha\gamma_0 < 1$	saddle	center
$\alpha\gamma_0 < 1 - \gamma_0/\omega^2$	center	Do not exist

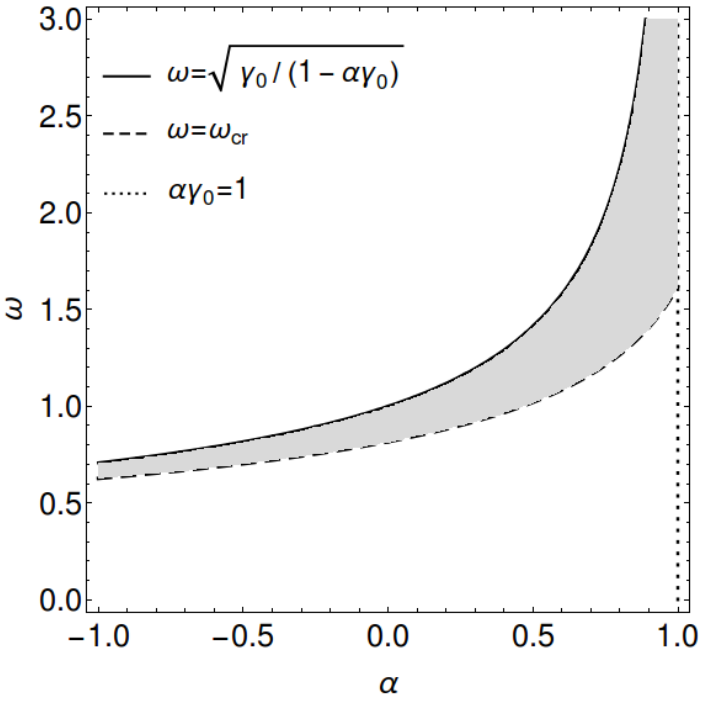

Fig. 5.2: The parametric domain of (α, ω) for the existence of bright solitons for $\gamma_0 = 1$ .The solid and dotted lines come from the saddle condition for the fixed point and the dashed line comes from the non-negative condition for the electron density. Here the negative α means the magnetic field is in the opposite direction of the laser field.

5.1.2 Density constraint

Though expression (5.10) gives the condition for the soliton solution to Eq. (5.5) mathematically, a physical restriction on the magnetic field and soliton frequency can be found from the non-negative condition of the electron density. Using Eqs. (5.1) and (5.4), one finds,

$$n_e = 1 + \varphi'' = 1 + \left(\frac{p_e}{\gamma_e} a'\right)' = 1 + \frac{\gamma_0^2 a'^2}{\gamma_e^3 - \alpha\gamma_0^4} + \frac{a}{\gamma_e - \alpha\gamma_0^2} a''. \tag{5.11}$$

The minimum density of the bright soliton happens at the center where $a' = 0$. Using Eq. (5.5), when the density drops to zero we have,

$$\gamma_e = \alpha\gamma_0^2 + \omega^2 a^2. \tag{5.12}$$

Substituting Eq. (5.12) into Eq. (5.3), we can eliminate a to get the critical γ_e,

$$\gamma_0^2 = \omega^2(\gamma_e - \alpha\gamma_0^2)(1 - \gamma_0^2/\gamma_e^2). \tag{5.13}$$

Meanwhile, the invariance of H gives,

$$\frac{1}{2}(\gamma_e - \alpha\gamma_0^2) - \left(\frac{1}{2}\alpha\gamma_0^2 \frac{\gamma_0^2}{\gamma_e^2} + \gamma_e\right) = -\left(\frac{1}{2}\alpha\gamma_0^2 + \gamma_0\right). \tag{5.14}$$

Combine Eqs. (5.13) and (5.14), we find γ_e and the critical frequency ω_{cr} when the density at the soliton center becomes zero satisfying [78],

$$\gamma_e = \frac{\gamma_0}{2-(\alpha\gamma_0+\gamma_0/\omega_{cr}^2)} \geq \gamma_0; \tag{5.15}$$

$$\alpha\gamma_0\left(\alpha\gamma_0+\frac{\gamma_0}{\omega_{cr}^2}-2\right)^3 = 2\left(\alpha\gamma_0+\frac{\gamma_0}{\omega_{cr}^2}\right)-3. \tag{5.16}$$

Notice that $\alpha\gamma_0 < 1$, hence $\alpha\gamma_0+\gamma_0/\omega_{cr}^2$ are in the range,

$$\frac{5-\sqrt{5}}{2} < \alpha\gamma_0+\frac{\gamma_0}{\omega_{cr}^2} < 2. \tag{5.17}$$

Eq. (5.16) is a cubic equation for γ_0/ω_{cr}^2 and the discriminant is $\alpha^3\gamma_0^3(27\alpha\gamma_0-32)$. When $\alpha\gamma_0<0$, it has one real root and two complex conjugate roots; when $0<\alpha\gamma_0<1$, it has three distinct real roots. Writing explicitly, they are,

$$\frac{\gamma_0}{\omega_{cr}^2} = \begin{cases} 2-\alpha\gamma_0+2\sqrt{\dfrac{2}{3\alpha\gamma_0}}\cos\left[\dfrac{1}{3}\arccos\left(\dfrac{3}{4}\sqrt{\dfrac{3\alpha\gamma_0}{2}}\right)-\dfrac{2\pi}{3}\right] & 0<\alpha\gamma_0<1 \\ 2-\alpha\gamma_0+\left(\sqrt{\dfrac{1}{4\alpha^2\gamma_0^2}-\dfrac{8}{27\alpha^3\gamma_0^3}}+\dfrac{1}{2\alpha\gamma_0}\right)^{\frac{1}{3}}-\left(\sqrt{\dfrac{1}{4\alpha^2\gamma_0^2}-\dfrac{8}{27\alpha^3\gamma_0^3}}-\dfrac{1}{2\alpha\gamma_0}\right)^{\frac{1}{3}} & \alpha\gamma_0<0 \end{cases} \tag{5.18}$$

In Fig. 5.2, we plot the parametric domain of (α,ω) for the existence of bright solitons. The solitons with physical significance can only exist in the shaded area. The solid and dotted lines come from the saddle condition for the fixed point and the dashed line comes from the non-negative condition for the electron density. Here the negative α means the magnetic field is in the opposite direction of the laser field. It can be see that for each magnetic field α, there is a lower limit of the soliton frequency ω_{cr}, beyond which the density at the soliton center is negative. In other words, there exists a maximum of the soliton amplitude. The maximum of the soliton amplitude and other physical quantities can be calculated by Eq. (5.15),

$$p_e = \pm\sqrt{\frac{\gamma_e^2}{\gamma_0^2}-1} = \pm\frac{\sqrt{(\alpha\gamma_0+\gamma_0/\omega_{cr}^2-1)(3-\alpha\gamma_0-\gamma_0/\omega_{cr}^2)}}{2-(\alpha\gamma_0+\gamma_0/\omega_{cr}^2)}; \quad a = p_e\left(1-\frac{\alpha\gamma_0^2}{\gamma_e}\right). \tag{5.19}$$

Let $S=\alpha\gamma_0+\gamma_0/\omega_{cr}^2$ and take the derivative of Eq. (5.16) with respect of $\alpha\gamma_0$, one finds $\partial S/\partial(\alpha\gamma_0) = (S-2)^4/(5-4S)$. It is always smaller than zero in the range of condition (5.17). Hence, S is a

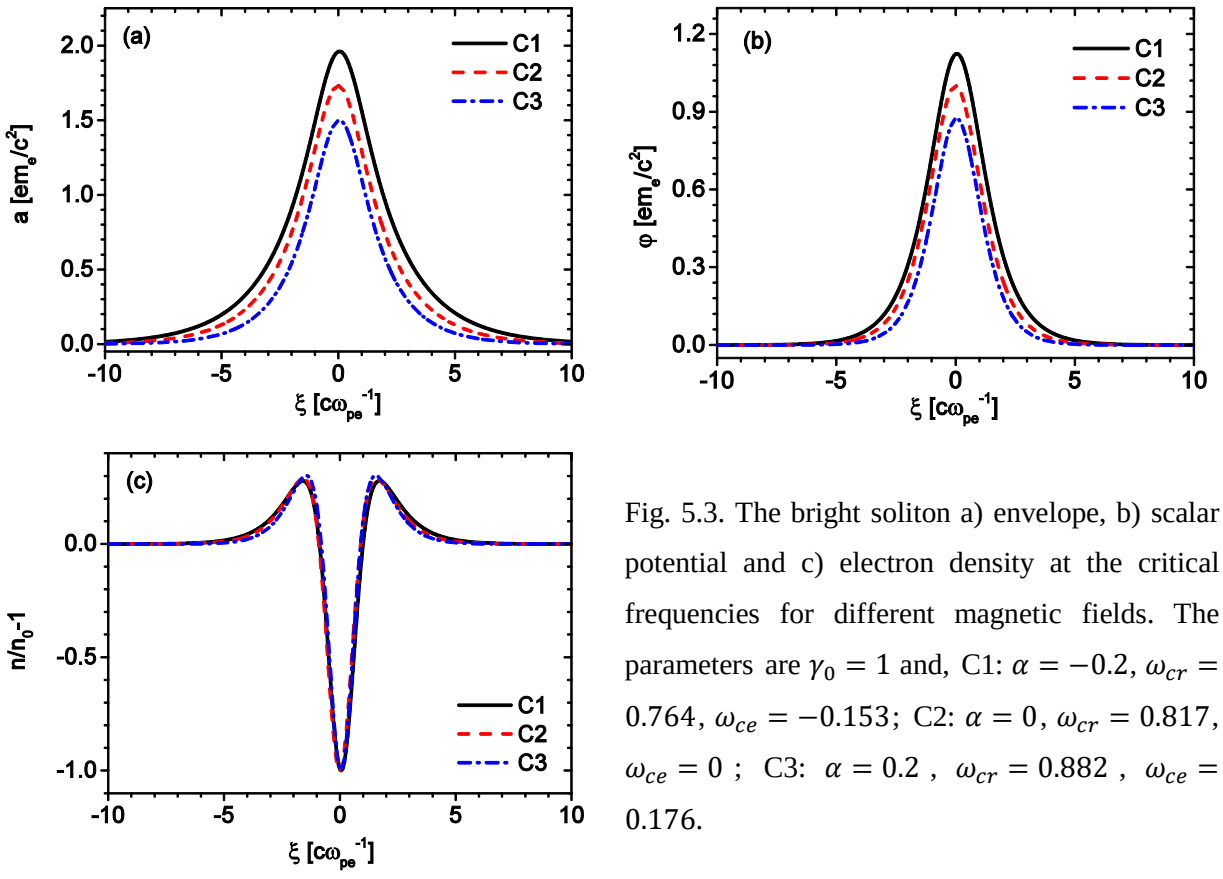

Fig. 5.3. The bright soliton a) envelope, b) scalar potential and c) electron density at the critical frequencies for different magnetic fields. The parameters are $\gamma_0 = 1$ and, C1: $\alpha = -0.2$, $\omega_{cr} = 0.764$, $\omega_{ce} = -0.153$; C2: $\alpha = 0$, $\omega_{cr} = 0.817$, $\omega_{ce} = 0$; C3: $\alpha = 0.2$, $\omega_{cr} = 0.882$, $\omega_{ce} = 0.176$.

decreasing function of $\alpha\gamma_0$ and thus ω_{cr} is an increasing function of $\alpha\gamma_0$. Meanwhile, γ_e, a are both decreasing functions of $\alpha\gamma_0$ and the minimums of them are reached at $\alpha\gamma_0 = 1$. Assuming $\gamma_0 = 1$, we find the minimums of the quantities are $\gamma_e = (\sqrt{5}+1)/2$, $p_e = \pm\sqrt{(\sqrt{5}+1)/2}$ and $a = \sqrt{\sqrt{5}-2}$.

We have numerically solved the soliton Eqs. (5.3) and (5.5) by the shooting method. The procedure is as follows: for fixed α and ω, we integrate Eq. (5.5) in the direction of increasing ξ with boundary condition $a'(-\xi_0) = \epsilon$, where ϵ is sufficiently small and ξ_0 is far away from the soliton center. We vary ϵ until at $\xi = \xi_0$ both a and φ vanish simultaneously. In Fig. 5.3, the soliton amplitude, scalar potential and density at the critical soliton frequencies are shown for different magnetic fields. It can be seen that the maximum soliton amplitude decreases with increasing magnetic field, which is consistent with the analysis.

5.1.3 Soliton envelops

An analytical expression of the soliton solution can be found in the limit of small amplitude. Using the variable transformation $p_{e\perp} = \sinh u$ with $\sinh u$ the hyperbolic sine function and expanding all the physical quantities to the third order of u in the limit of $u \ll 1$, we have,

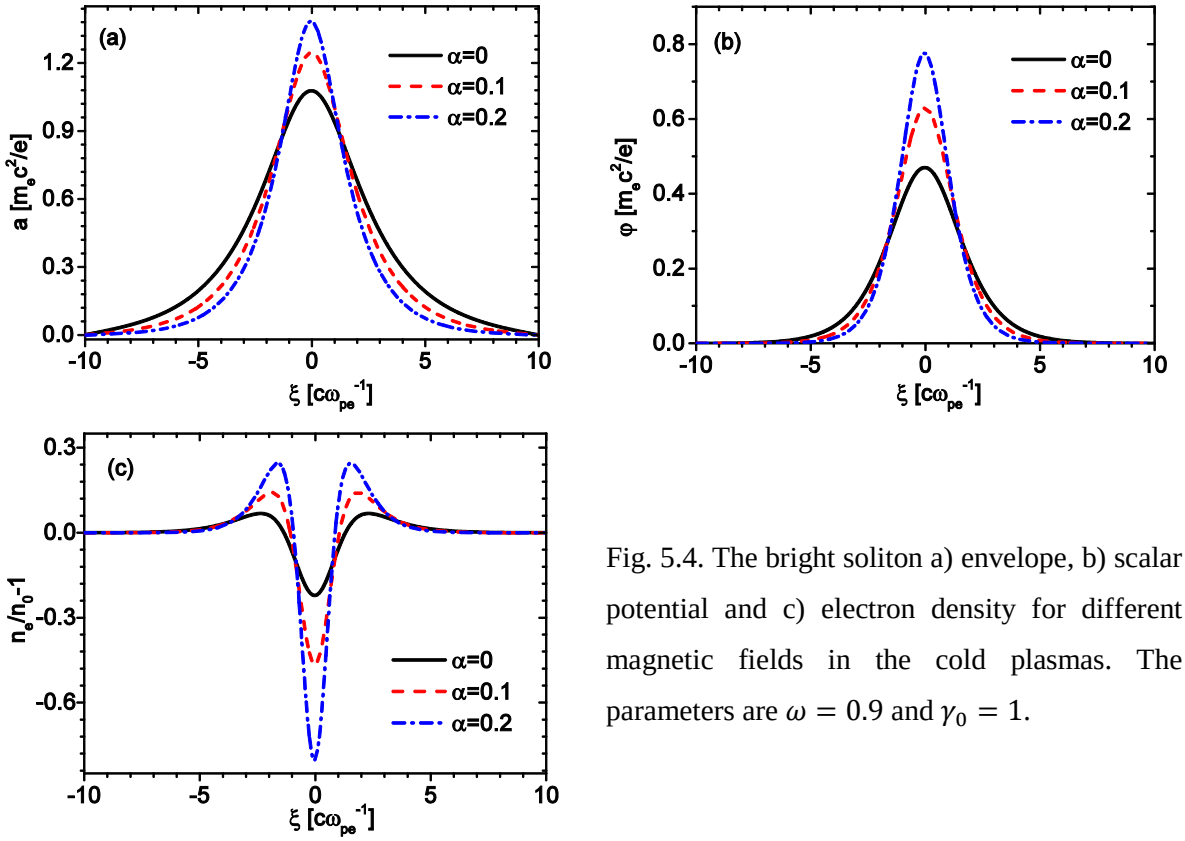

Fig. 5.4. The bright soliton a) envelope, b) scalar potential and c) electron density for different magnetic fields in the cold plasmas. The parameters are $\omega = 0.9$ and $\gamma_0 = 1$.

$$p_e \sim u + \frac{u^3}{6}; \quad \gamma_e \sim \gamma_0\left(1 + \frac{u^2}{2}\right); \qquad a \sim (1 - \alpha\gamma_0)u + \frac{u^3}{6}(1 + 2\alpha\gamma_0);$$
$$a' \sim \left[(1 - \alpha\gamma_0) + \frac{u^2}{2}(1 + 2\alpha\gamma_0)\right]u'; \quad a'' \sim (1 - \alpha\gamma_0)u'' + (1 + 2\alpha\gamma_0)uu'^2. \tag{5.20}$$

The soliton equation (5.5) becomes,

$$u'' + \frac{3\alpha\gamma_0}{1 - \alpha\gamma_0}uu'^2 = \lambda^2 u - \beta u^3. \tag{5.21}$$

Here $\lambda^2 = -\omega^2 + \gamma_0/(1 - \alpha\gamma_0)$ and $\beta = [-4\gamma_0 + \omega^2(7 - 4\alpha\gamma_0)]/[6(1 - \alpha\gamma_0)]$. Notice that λ is exactly the eigenvalue at Q_0. Neglecting the nonlinear term of u'^2, Eq. (5.21) has the solution,

$$u = \lambda\sqrt{2/\beta}\,\mathrm{sech}(\lambda\xi). \tag{5.22}$$

The peak amplitude of the soliton is $\lambda\sqrt{2/\beta}$ and the soliton width is approximately inversely proportional to λ. Since both λ and $\lambda\sqrt{2/\beta}$ are increasing functions of $\alpha\gamma_0$, thus the soliton tends to be peaked as the magnetic field increases. Fig. 5.4 and Fig. 5.5 show the numerical calculations of the soliton amplitude, scalar potential and density profile as a function of space under different magnetic fields and

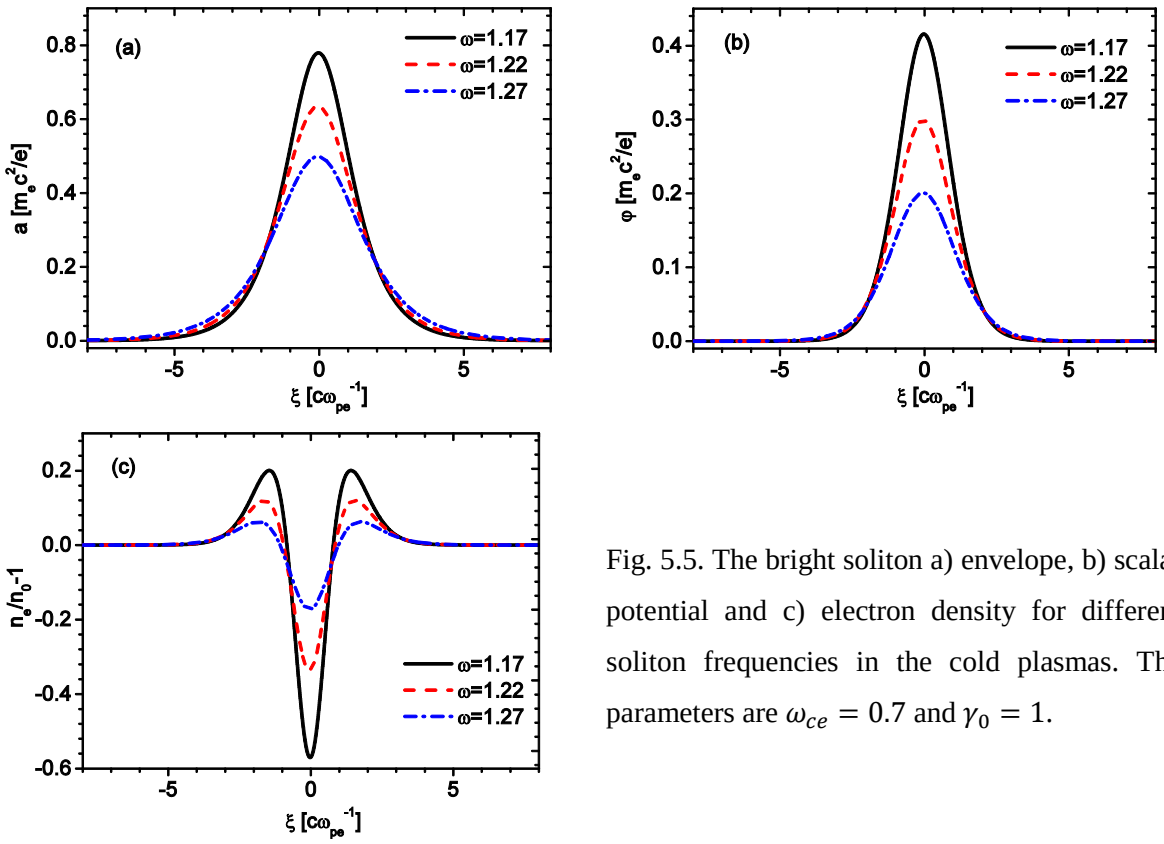

Fig. 5.5. The bright soliton a) envelope, b) scalar potential and c) electron density for different soliton frequencies in the cold plasmas. The parameters are $\omega_{ce} = 0.7$ and $\gamma_0 = 1$.

soliton frequencies. It is observed that the soliton amplitude increases with magnetic field and the soliton width becomes narrower. For fixed magnetic field, the soliton amplitude decreases with increasing soliton frequency. These tendencies are consistent with the analytical predictions. Note that on the soliton wings, density hump appears due to the attraction of fixed background ions.

5.2 Bright solitons in warm plasmas

In warm plasmas, the scalar potential φ cannot be eliminated and the system remains 4D. The Hamiltonian in this case is,

$$H(a, a', \varphi, -\gamma_0^2\varphi') = \frac{1}{2}\left(a'^2 + \omega^2 a^2 - \gamma_0^2\varphi'^2\right) + \gamma_0^2[v_{te}^2(n_e - 1) - \varphi]. \tag{5.23}$$

Note that H does not depend on ξ explictly, it is constant along the orbit in phase space. As discussed in chapter 4, the dynamics of the system are constrained to the 3D energy surface $H \equiv H_0(Q_0)$ and the solitons only exist when the stable and unstable manifolds intersect within this manifold.

5.2.1 Bright solitons with continuous spectra

We first discuss the fixed point Q_0. The eigenvalues are determined by Eq. (4.43), which is

$$\lambda_{1-4}^2 = \pm\sqrt{\frac{1}{2}\left(\delta \pm \sqrt{\Delta}\right)}. \tag{4.43}$$

with $\delta = J_{21} + J_{43}$, $\Delta = (J_{21} - J_{43})^2 + 4J_{23}J_{41}$. $J_{i,j}$ $(i = 2,4; j = 1,3)$ are expressed as,

$$\begin{aligned} J_{21} &= -\left(\omega^2 - \frac{n\gamma_0^4}{\gamma_e^3 - \alpha\gamma_0^4}\right) - \frac{n}{v_{te}^2}\frac{\gamma_0^2 p_{e\perp}^2}{\gamma_e^2}; \qquad & J_{23} &= \gamma_0^2\frac{n}{v_{te}^2}\frac{p_{e\perp}}{\gamma_e}; \\ J_{41} &= -\frac{n}{v_{te}^2}\frac{p_{e\perp}}{\gamma_e}; & J_{43} &= \frac{n}{v_{te}^2}. \end{aligned} \tag{5.24}$$

At Q_0, $p_{e\perp} = 0$, $n_e = n = 1$. Hence $J_{41} = J_{23} = 0$, $J_{21} = -\omega^2 + \gamma_0/(1 - \alpha\gamma_0)$, $J_{43} = 1/v_{te}^2$ and the eigenvalues at Q_0 are,

$$\lambda_{1,2}^2 = -\omega^2 + \frac{\gamma_0}{1 - \alpha\gamma_0}; \qquad \lambda_{3,4}^2 = \frac{1}{v_{te}^2} > 0. \tag{5.25}$$

Q_0 is either a saddle-center ($\lambda_{1,2}^2 < 0$) or a saddle point ($\lambda_{1,2}^2 > 0$). If $\lambda_{1,2}^2 > 0$, both the stable manifold $W_{Q_0}^S$ and unstable manifold $W_{Q_0}^u$ are 2D and they are tangent to the linear subspaces spanned by $X_{1,2}$ and $X_{3,4}$. Here X_{1-4} are the eigenvectors corresponding to λ_{1-4} with expressions given by,

$$\begin{cases} X_{1,2} = \left(1/\left(1 + \lambda_{1,2}^2\right)^{1/2}, \quad \lambda_{1,2}/\left(1 + \lambda_{1,2}^2\right)^{1/2}, \quad 0, \quad 0\right) \\ X_{3,4} = \left(0, \quad 0, \quad 1/\left(1 + \lambda_{3,4}^2\right)^{1/2}, \quad \lambda_{3,4}/\left(1 + \lambda_{3,4}^2\right)^{1/2}\right) \end{cases} \tag{5.26}$$

Notice that $\lambda_1 = -\lambda_2$, $\lambda_3 = -\lambda_4$. In the saddle domain, the soliton solutions are general or they have a continuous ω spectrum since the two manifold generally intersect. In Fig. 5.6, we show a typical plot of the 2D stable and unstable manifolds in the saddle domain for $\omega = 0.9$, $\alpha = 0.1$ and $v_{te} = 0.8$. The manifolds are projected in the (a, a', φ) subspace. The visualization of the stable and unstable manifolds is a challenge and interesting technical task and one can read Ref 88 for a survey of the numerical methods. Here the continuation package AUTO [89,90] is used for the calculation of the manifolds. The method implemented in AUTO is the boundary value problem (BVP) continuation of trajectories, which will be discussed in section 5.4. In the (a, a', φ) subspace, both the stable and unstable manifolds look like the twisted trousers legs with different directions and they intersect at the waist of the trousers to form a closed orbit — the homoclinic orbit. It should be mentioned that these "legs" extend above the waist and in Fig. 5.6 (a) and (b) we only plot the lower halves for clarity. The intersection of the stable and unstable manifolds is further

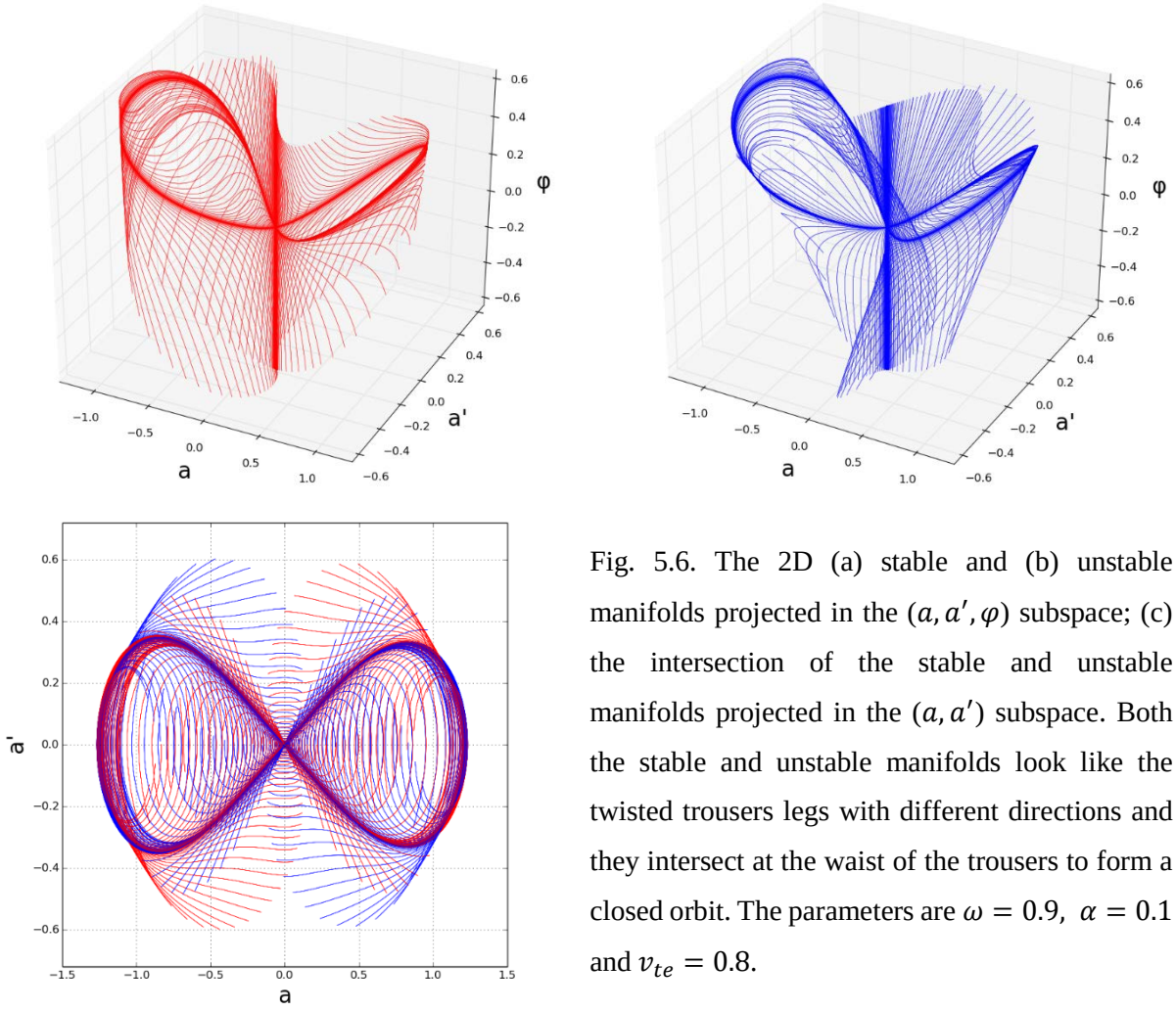

Fig. 5.6. The 2D (a) stable and (b) unstable manifolds projected in the (a, a', φ) subspace; (c) the intersection of the stable and unstable manifolds projected in the (a, a') subspace. Both the stable and unstable manifolds look like the twisted trousers legs with different directions and they intersect at the waist of the trousers to form a closed orbit. The parameters are $\omega = 0.9,\ \alpha = 0.1$ and $v_{te} = 0.8$.

projected in the (a, a') subspace in Fig. 5.6(c). In this subspace, the phase portrait resembles the 2D Hamiltonian with a saddle at the origin, e.g. Fig. 5.1(c). Therefore, the soliton has a continuous spectrum if $\alpha\gamma_0$ and ω satisfy,

$$1 - \gamma_0/\omega^2 < \alpha\gamma_0 < 1 \tag{5.27}$$

It is the same as Eq. (5.10), however due to the finite temperature effects in Eq. (5.4), the restriction Eq. (5.16) on the magnetic field and soliton frequency disappears. If the magnetic field is fixed, then the soliton frequency should satisfy,

$$\begin{cases} \gamma_0\omega_{ce} < \omega < \omega^r_{cut\_e} & \text{when } \omega_{ce} > 0 \\ 0 < \omega < \omega^r_{cut\_e} & \text{when } \omega_{ce} < 0 \end{cases} \tag{5.28}$$

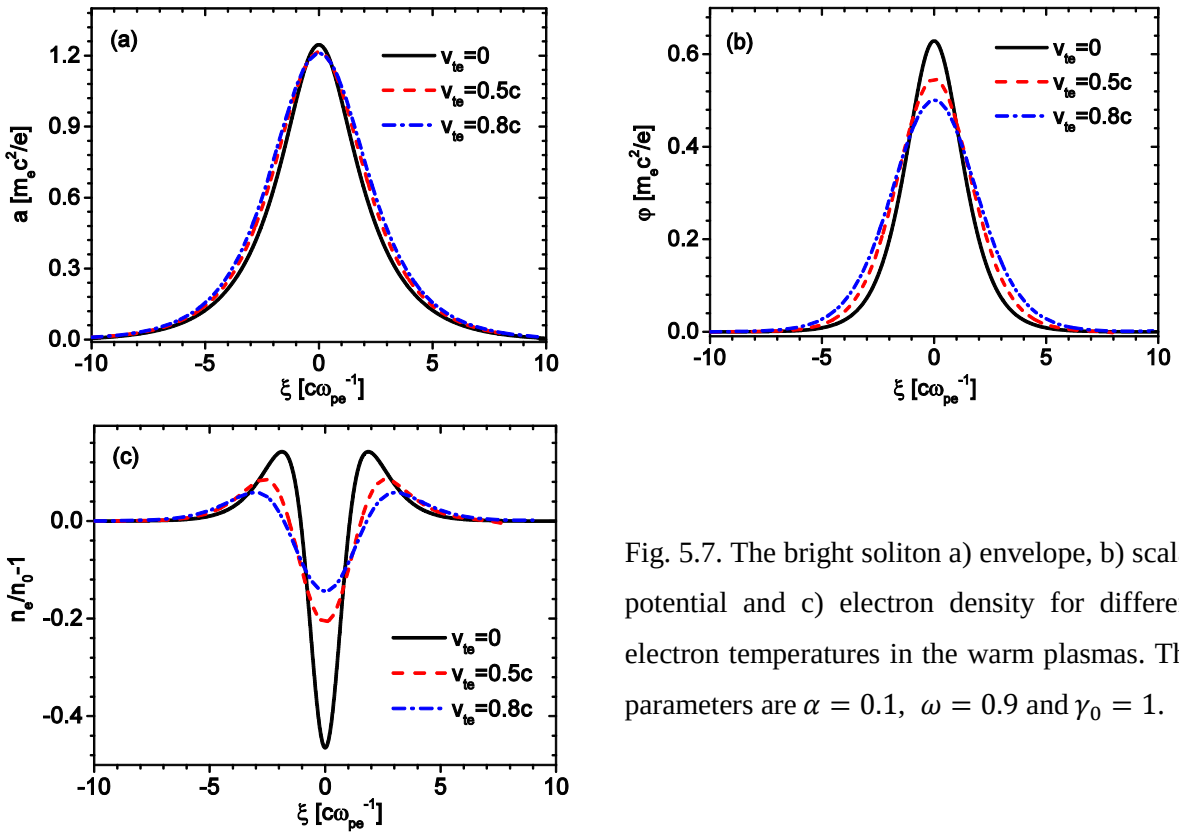

Fig. 5.7. The bright soliton a) envelope, b) scalar potential and c) electron density for different electron temperatures in the warm plasmas. The parameters are $\alpha = 0.1,\ \omega = 0.9$ and $\gamma_0 = 1$.

Here $\omega_{cut\_e}^{r} = \left(\gamma_0\omega_{ce} + \sqrt{\gamma_0^2\omega_{ce}^2 + 4\gamma_0}\right)/2$ is the cutoff frequency for the RCP wave in magnetized plasmas with only electron's effects.

In Fig. 5.7 and Fig. 5.8, we show the bright solitons with different electron temperatures and magnetic fields in the saddle domain. It can be seen that while the soliton amplitude and width vary slightly with temperature, the scalar potential and electron density are much more sensitive to the temperature. As the temperature decreases, the density cavity becomes narrower and deeper. However, it can never become negative due to the thermal pressure term. As the magnetic field increases, the soliton envelop tends to be peaked and stronger, which is the same as the cold plasma case.

5.2.2 Bright solitons with discrete spectra

When $\lambda_{1,2}^2 < 0$, the fixed point Q_0 is a saddle-center. In this case, the stable and unstable manifolds are 1D. They are not generally expected to intersect in the 3D energy manifold. If they interest, one would expect $W_{Q_0}^{s} = W_{Q_0}^{u}$, which could only be satisfied by specific $(\gamma_0, \alpha, \omega)$. In other words, the soliton will have discrete spectrum.

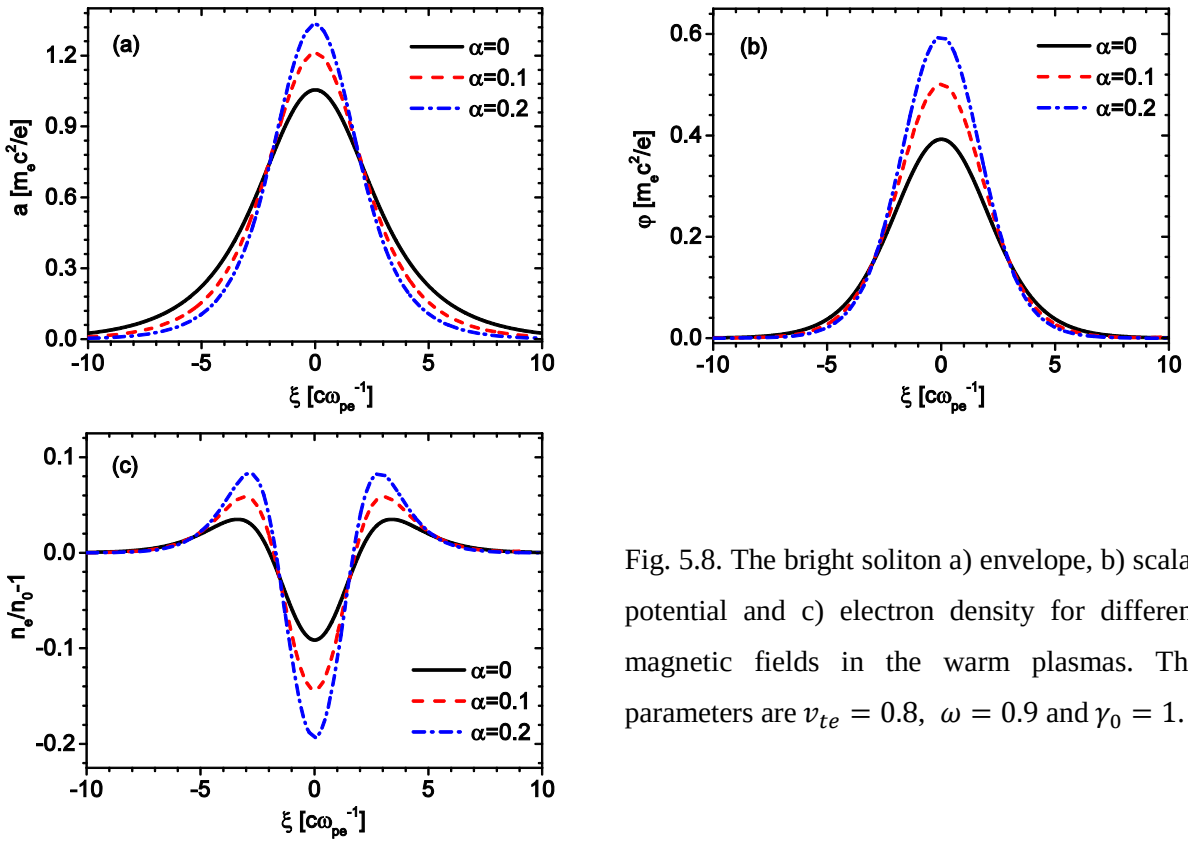

Fig. 5.8. The bright soliton a) envelope, b) scalar potential and c) electron density for different magnetic fields in the warm plasmas. The parameters are $v_{te} = 0.8$, $\omega = 0.9$ and $\gamma_0 = 1$.

We have also used the shooting method to search for the bright solitons in the saddle-focus domain. However, in our detection of parameter regions, the soliton solutions do not exist. Further investigations are needed.

5.2.3 Connection orbit with $Q_*^{\pm}$

The additional fixed points $Q_*^{\pm}(\pm a^*, 0, \varphi^*, 0)$ exist when $\alpha\gamma_0 > 1 - \gamma_0/\omega^2$ with a^* and φ^* given by Eq. (4.35). Thus there is a possibility of a heteroclinic connection between Q_0 and $Q_{\pm}^*$. Since the right boundary ($\xi \to \infty$) $Q_{\pm}^*$ is different from Q_0, the soliton solution is asymmetric. The eigenvalues at $Q_{\pm}^*$ can be calculated by Eqs. (4.43) and (5.24). Note that $\gamma_e = \gamma_0^2(\alpha + 1/\omega^2)$ at $Q_*^{\pm}$. Then $\gamma_e^3 > \gamma_e\gamma_0^2 = \alpha\gamma_0^4 + \gamma_0^4/\omega^2$, or,

$$\lambda^2 = -\omega^2 + \frac{\gamma_0^4}{\gamma_e^3 - \alpha\gamma_0^4} < 0. \tag{5.29}$$

Meanwhile one has,

$$\delta = \lambda^2 + \frac{1-\gamma_0^2 p_{e\perp}^2/\gamma_e^2}{v_{te}^2} \tag{5.30}$$

$$\Delta = \left[\lambda^2 - \frac{(1+\gamma_0 p_{e\perp}/\gamma_e)^2}{v_{te}^2}\right]\left[\lambda^2 - \frac{(1-\gamma_0 p_{e\perp}/\gamma_e)^2}{v_{te}^2}\right] > 0 \tag{5.31}$$

Hence $\delta^2 - \Delta = 4\lambda^2/v_{te}^2 < 0$. The fixed points $Q_*^{\pm}$ are always saddle-centers. The heteroclinic orbits involving Q_0 and $Q_{\pm}^*$ do not generally exist.

5.3 Bright solitons with ion's motion

Now let's discuss the bright solitons with ion's motion. Due to the huge mass difference between ions and electrons, the ions are assumed to be non-relativistic. This approximation is generally applicable for current laser systems.

5.3.1 Ion's effects

At the fixed point Q_0, $p_{e\perp} = p_{i\perp} = 0$, $n_e = n_i = n = 1$, the eigenvalues are,

$$\lambda_{1,2}^2 = -\omega^2 + \frac{\gamma_0(\rho+1)}{(1-\alpha\gamma_0)(1+\rho\alpha\gamma_0)}; \qquad \lambda_{3,4}^2 = \frac{1}{v_{te}^2} + \frac{\rho}{v_{ti}^2} > 0. \tag{5.32}$$

Hence Q_0 can be either a saddle or a saddle-center. The existence of continuous bright solitons requests,

$$\begin{cases} -1/\rho < \alpha\gamma_0 < 1 & \text{when } \omega^2 \le 4\gamma_0\rho/(1+\rho) \\ -1/\rho < \alpha\gamma_0 < \beta_-, \quad \beta_+ < \alpha\gamma_0 < 1 & \text{when } \omega^2 > 4\gamma_0\rho/(1+\rho) \end{cases} \tag{5.33}$$

Here $\beta_{\pm} = \left[\rho - 1 \pm \sqrt{(\rho+1)^2 - 4\rho(\rho+1)\gamma_0/\omega^2}\right]/(2\rho)$. Comparing Eq. (5.27) with Eq. (5.33), it is found that, when ion's motion is taken into consideration, the requirement for magnetic field turns out to be different with soliton frequencies. When soliton has a lower frequency, the range is one whole interval, otherwise it breaks into two small intervals. If $\rho \to 0$, condition (5.33) returns to condition (5.27). On the other hand, if the external magnetic field is given, the soliton frequency can be deduced as,

$$\begin{cases} \gamma_0\omega_{ce} < \omega < \omega_{cut}^r & \text{when } \omega_{ce} > 0 \\ \gamma_0\omega_{ci} < \omega < \omega_{cut}^r & \text{when } \omega_{ce} < 0 \end{cases} \tag{5.34}$$

Here $\omega_{cut}^r = \left[(1-\rho)\gamma_0\omega_{ce} + \sqrt{(\rho+1)^2\gamma_0^2\omega_{ce}^2 + 4\gamma_0(\rho+1)}\right]/2$ is the cut off frequency for RCP wave with ion's motion and ω_{ci} is the ion cyclotron frequency. It returns to condition ((5.28) when $\rho \to 0$. The

physical meaning of inequality (5.34) is clear: when the magnetic field is along the propagation direction the electron's motion plays a role, otherwise ion's contribution is dominant. Once the soliton frequency exceeds ω_{cut}^{r}, the solitary wave can propagate as the usual Whistler mode. Since ρ is much smaller than unity, the soliton can reach rather low frequency when the magnetic field is opposite to the propagation direction.

The additional fixed points $Q_*^{\pm}$ exist when condition (4.34) is satisfied and the stabilities can also be calculated by Eq. (4.43). It can be proved that $Q_*^{\pm}$ are always saddle-centers. Actually let,

$$t \equiv -\omega^2 + \frac{n}{\alpha}\left(\frac{\gamma_e^3}{\gamma_e^3 - \alpha\gamma_0^4} - \frac{\gamma_i^3}{\gamma_i^3 + \rho\alpha\gamma_0^4}\right) = \omega^2 \frac{\gamma_0\gamma_e(1+\rho\alpha\gamma_0)(\gamma_0^2 - \gamma_e^2)}{(\gamma_0 + \rho\gamma_e)(\gamma_e^3 - \alpha\gamma_0^4)} \tag{5.35}$$

Here $\gamma_i = \gamma_0$ and Eq. (4.30) have been used. Then $t < 0$ and the following two inequalities hold,

$$\begin{aligned} |J_{21}^* - J_{43}^*| \quad &= -t + n\left[\frac{1}{v_{te}^2}\left(\frac{\gamma_0^2 p_{e\perp}^2}{\gamma_e^2} + 1\right) + \frac{\rho}{v_{ti}^2}\left(\frac{\gamma_0^2 p_{i\perp}^2}{\gamma_i^2} + 1\right)\right] \\ &> 2n\left(\frac{1}{v_{te}^2}\frac{\gamma_0 p_{e\perp}}{\gamma_e} + \frac{\rho}{v_{ti}^2}\frac{\gamma_0 p_{i\perp}}{\gamma_i}\right) = 2|J_{23}^* J_{41}^*|; \end{aligned} \tag{5.36}$$

$$\begin{aligned} \delta^2 - \Delta \quad &= 4(J_{21}^* J_{43}^* - J_{23}^* J_{41}^*) \\ &= 4\left[tn\left(\frac{1}{v_{te}^2} + \frac{\rho}{v_{ti}^2}\right) - n^2\gamma_0^2 \frac{1}{v_{te}^2}\frac{\rho}{v_{ti}^2}\left(\frac{p_{e\perp}}{\gamma_e} - \frac{p_{i\perp}}{\gamma_i}\right)^2\right] < 0 \end{aligned} \tag{5.37}$$

Here the superscript "*" represents the value taken at $Q_*^{\pm}$. So $\Delta = (J_{21}^* - J_{43}^*)^2 + 4J_{23}^* J_{41}^* > 0$ and $|\delta| < \sqrt{\Delta}$. The fixed points $Q_*^{\pm}$ are always saddle-centers. Hence, heteroclinic connections with $Q_*^{\pm}$ are not general.

5.3.2 Quasi-neutral approximation

If we assume in the neighborhood of the fixed points the quasi-neutral approximation holds. Then the 4D Hamiltonian is reduced to 2D. Using the transformation $p_{e\perp} = \sinh u$, then $a = \sinh u - \alpha\gamma_0 \tanh u$ and $p_{i\perp} = -\rho a/(1 + \rho\alpha\gamma_0)$. The Hamiltonian becomes,

$$H(u, u') = \frac{1}{2}[(\cosh u - \alpha\gamma_0 \operatorname{sech}^2 u)^2 u'^2 + \omega^2(\sinh u - \alpha\gamma_0 \tanh u)^2] + \frac{c_s^2\gamma_0^2}{\rho}(n-1) \tag{5.38}$$

Here n is given by,

$$\gamma_0 c_s^2 \ln n \approx \rho(1 - \cosh u) + \frac{1}{2}\rho\alpha\gamma_0 \tanh^2 u - \frac{1 + \rho\alpha\gamma_0}{2} p_{i\perp}^2 \tag{5.39}$$

We mention that (u, u') are not the canonical variables. The soliton equation is,

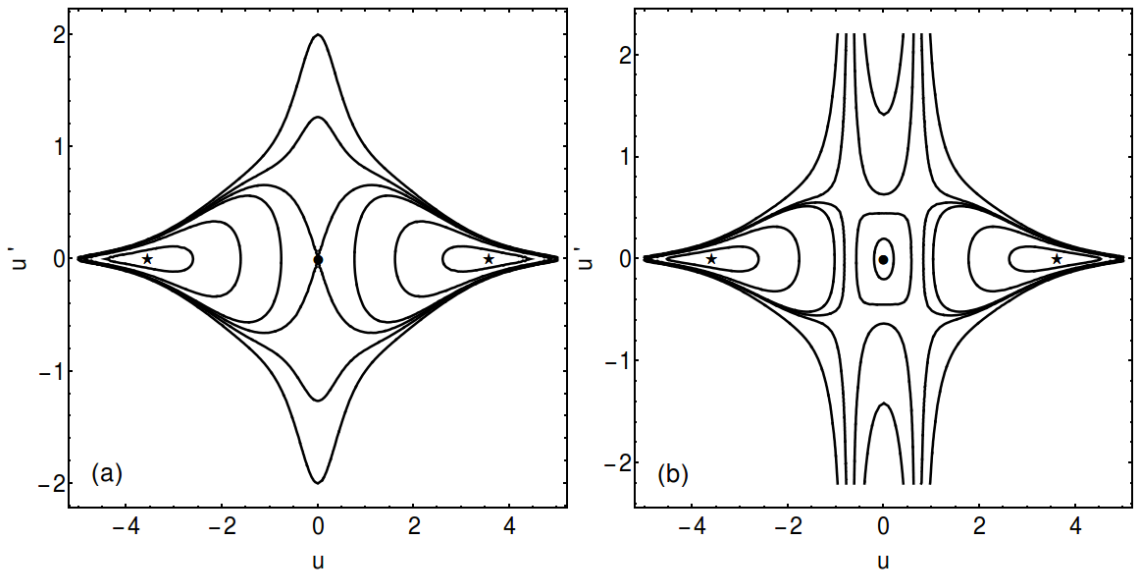

Fig. 5.9 Phase portraits of Eq. (5.38) in the (u, u') plane when $\omega^2 < 4\rho\gamma_0/(\rho+1)$ with a) $\alpha = 0.5$ and b) $\alpha = 2$. The parameters are $\omega = 0.04, \rho = 1/1836, c_s = 0.05$ and $\gamma_0 = 1$. The fixed points Q_0 and $Q_*^{\pm}$ are marked by round dot and asterisks, respectively. In (a) and (b), $Q_*^{\pm}$ always exist since $\alpha\gamma_0 > -1/\rho$.

$$(\sinh u - \alpha\gamma_0 \tanh u)'' + \omega^2(\sinh u - \alpha\gamma_0 \tanh u) = \frac{n\gamma_0}{1+\rho\alpha\gamma_0}(\tanh u + \rho \sinh u) \qquad (5.40)$$

The fixed points Q_0 and $Q_*^{\pm}$ are the same as before. Furthermore, the existence condition for bright solitons remains the same as inequality (5.33). However, $Q_{\pm}^*$ change to centers.

In Fig. 5.9 and Fig. 5.10, we give the phase portraits of Eq. (5.38) in the (u, u') plane for different magnetic fields and soliton frequencies. The fixed points Q_0 and $Q_*^{\pm}$ are marked by round dot and asterisks, respectively. Note that in Fig. 5.9 $\omega < [4\rho\gamma_0/(\rho+1)]^{1/2} = 0.047$ and in Fig. 5.10 $\omega > 0.047$, which corresponds to different conditions in (5.33). In Fig. 5.9, there are always 3 fixed points since $\alpha\gamma_0 > -1/\rho$; in Fig. 5.9(a), Q_0 is a saddle point since $\alpha\gamma_0 < 1$ and in Fig. 5.9(b) Q_0 is a center. In Fig. 5.10(a), $-1/\rho < \alpha\gamma_0 < \beta_- = -1834.4$, there are 3 fixed points and Q_0 is the saddle; in Fig. 5.10(b), $\beta_- < \alpha\gamma_0 < \beta_+ = -0.563$, there is only one fixed point Q_0 and it is a center; in Fig. 5.10(c), $\beta_+ < \alpha\gamma_0 < 1$, there are 3 fixed points and Q_0 changes to a saddle point; in Fig. 5.9(d), $\alpha\gamma_0 > 1 > \beta_+$, there are 3 fixed points and Q_0 is a center. In all the plots $Q_*^{\pm}$ are always centers. Soliton solutions can be found in Fig. 5.9(a), Fig. 5.10(a) and (c).

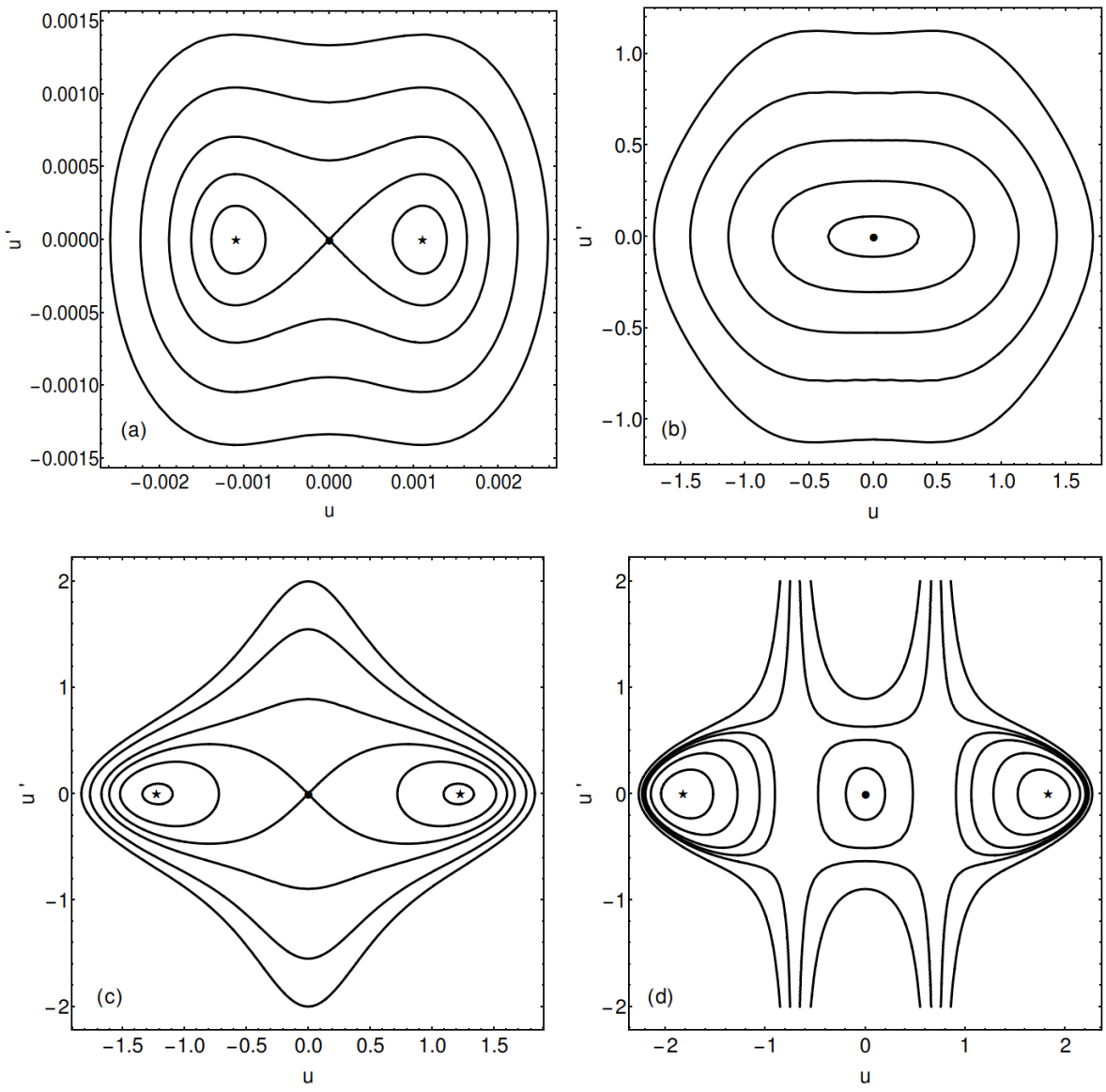

Fig. 5.10. Phase portraits of Eq. (5.38) in the (u, u') plane when $\omega^2 > 4\rho\gamma_0/(\rho+1)$ with a) $\alpha = -1835$; b) $\alpha = -0.8$; c) $\alpha = 0.5$ and d) $\alpha = 2$. The parameters are $\omega = 0.8, \rho = 1/1836, c_s = 0.05$ and $\gamma_0 = 1$. The fixed points Q_0 and $Q_*^{\pm}$ are marked by round dot and asterisks, respectively. In (a) $-1/\rho < \alpha\gamma_0 < \beta_-$, $Q_*^{\pm}$ exist; in (b) $\beta_- < \alpha\gamma_0 < \beta_+$, $Q_*^{\pm}$ do not exist; in (c) and (d) $\alpha\gamma_0 > \beta_+$, $Q_*^{\pm}$ exist.

5.3.3 Soliton envelops under quasi-neutral approximation

The small amplitude soliton solutions under quasi-neutral approximation can be derived following steps in section 5.1.3,

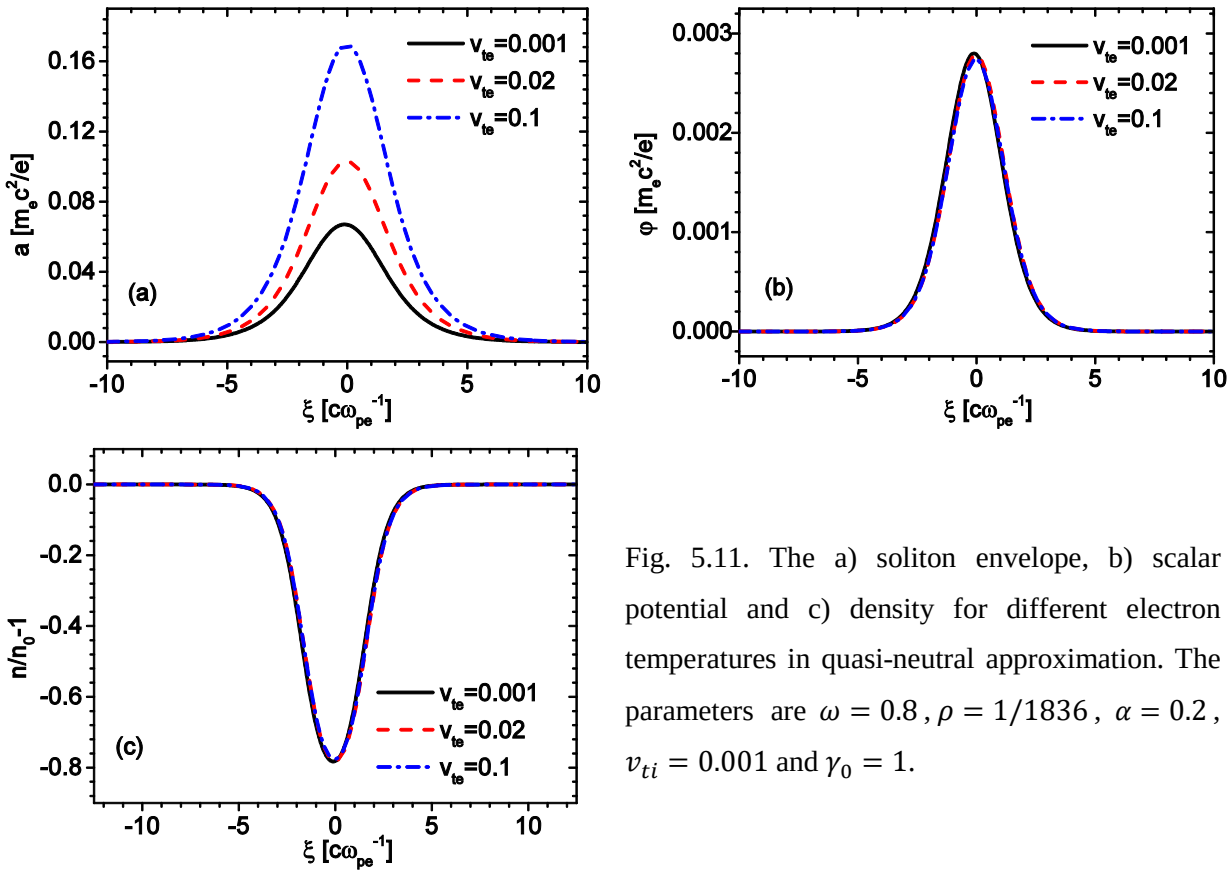

Fig. 5.11. The a) soliton envelope, b) scalar potential and c) density for different electron temperatures in quasi-neutral approximation. The parameters are $\omega = 0.8$, $\rho = 1/1836$, $\alpha = 0.2$, $v_{ti} = 0.001$ and $\gamma_0 = 1$.

$$p_i \sim -\left(\frac{\rho - \rho\alpha\gamma_0}{1+\rho\alpha\gamma_0}u + \frac{\rho u^3}{6}\frac{1+2\alpha\gamma_0}{1+\rho\alpha\gamma_0}\right); \qquad \gamma_i \sim \gamma_0\left[1 + \frac{1}{2}\left(\frac{\rho - \rho\alpha\gamma_0}{1+\rho\alpha\gamma_0}\right)^2 u^2\right]. \tag{5.41}$$

Then the density can be calculated from Eq. (5.39),

$$n \approx 1 - \frac{1+\rho}{2\gamma_0 c_s^2}\frac{\rho - \rho\alpha\gamma_0}{1+\rho\alpha\gamma_0}u^2. \tag{5.42}$$

Substitute n into Eq. (5.40), we obtain,

$$u'' + u\frac{1+2\alpha\gamma_0}{1-\alpha\gamma_0}u'^2 = \lambda^2 u - \beta u^3. \tag{5.43}$$

Here $\lambda^2 = \frac{\gamma_0+\rho\gamma_0}{(1+\rho\alpha\gamma_0)(1-\alpha\gamma_0)} - \omega^2$ and $\beta = \frac{\gamma_0(2-\rho)}{6(1+\rho\alpha\gamma_0)(1-\alpha\gamma_0)} + \frac{\gamma_0\rho}{2\gamma_0 c_s^2}\frac{(1+\rho)^2}{(1+\rho\alpha\gamma_0)^2} + \frac{\omega^2(1+2\alpha\gamma_0)}{6(1-\alpha\gamma_0)}$. Note that the existence condition for localized soliton solution requires $\lambda^2 > 0$, which returns to condition (5.33). If we neglect the nonlinear term of the first derivative of u, Eq. (5.43) can be integrated to get,

$$u(\xi) = \lambda\sqrt{2/\beta}\,\mathrm{sech}(\lambda\xi) \tag{5.44}$$

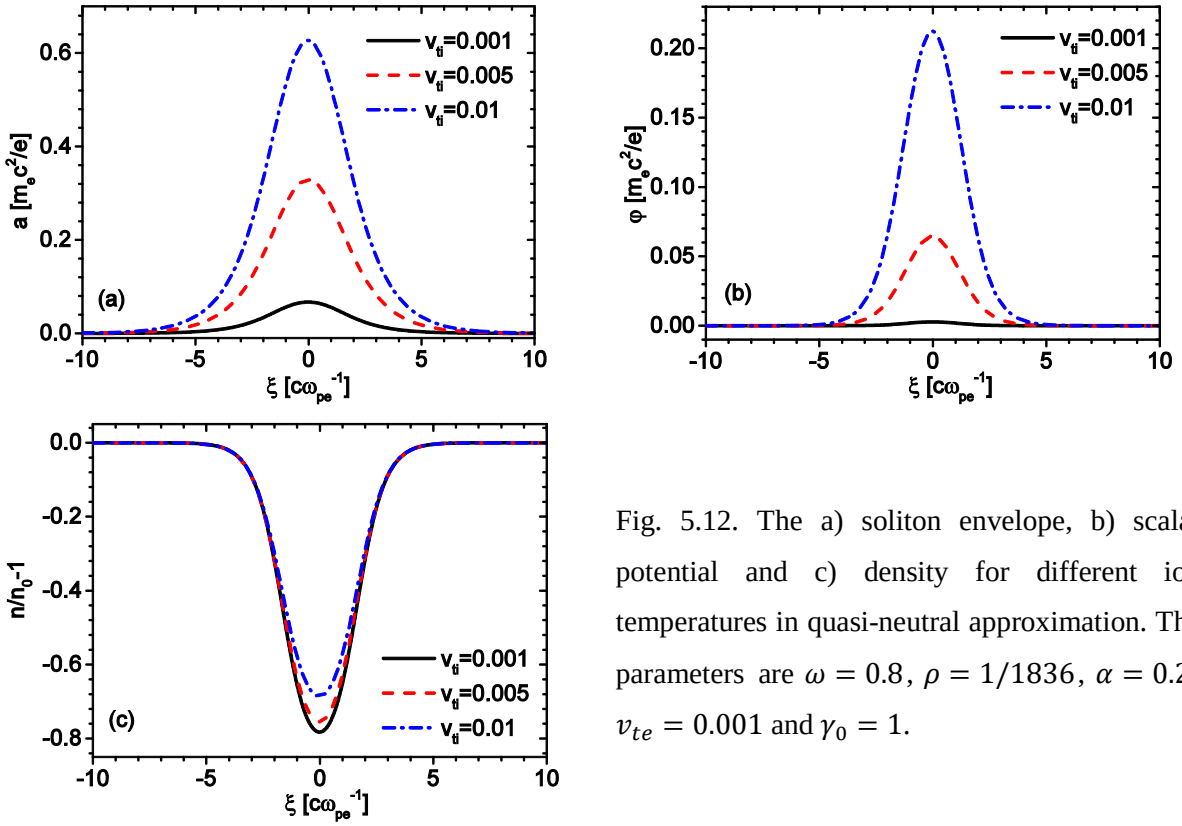

Fig. 5.12. The a) soliton envelope, b) scalar potential and c) density for different ion temperatures in quasi-neutral approximation. The parameters are $\omega = 0.8$, $\rho = 1/1836$, $\alpha = 0.2$, $v_{te} = 0.001$ and $\gamma_0 = 1$.

The soliton width is approximately inversely proportional to λ which is an increasing function of $\alpha\gamma_0$ in the region $[-1/\rho\,, (2\rho-1)/2\rho]$ and a decreasing function of $\alpha\gamma_0$ in the region $[(2\rho-1)/2\rho\,, 1]$. The peak of soliton amplitude is $\lambda\sqrt{2/\beta}$. Notice that it increases with increasing temperature, which is different from the ion fixed case, where the temperature effects suppress the soliton amplitude. In Fig. 5.11 and Fig. 5.12, we show the effects of electron and ion temperature on the solitons properties. It is found that compared with the soliton amplitude, the density and scalar potential profiles are more closely related to ion's temperature than electron's temperature. This is due to the quasi-neutral approximation, where electron's motion follows with ion's motion. Moreover, the density hump on the soliton wings disappears compared to the ion fixed case. It is interesting to notice that the scalar potential increases with temperature, however the density cavity becomes slightly smaller. This can be verified by Eq. (5.42), where the density perturbation is about $\delta n \sim u^2(1+\rho)(\rho-\rho\alpha\gamma_0)/[(2\gamma_0\, c_s^2\,)(1+\rho\alpha\gamma_0\,)]$. It is a decreasing function of temperature. Fig. 5.13 and Fig. 5.14 show the soliton profiles under different magnetic fields and soliton frequencies. Similar to the ion fixed case, under our numerical parameter ($\rho = 1/1836 \to 0$) the soliton becomes more peaked and stronger as the magnetic field increases and it decreases with increasing soliton frequency.

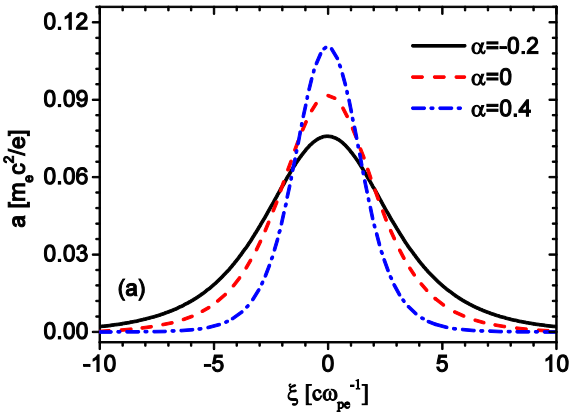

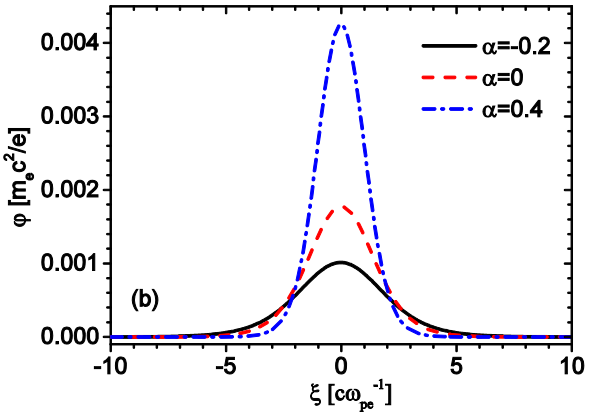

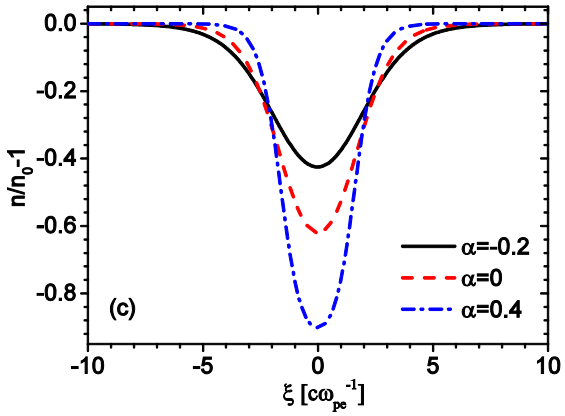

Fig. 5.13. The a) soliton envelope, b) scalar potential and c) density for different magnetic fields in quasi-neutral approximation. The parameters are $\omega = 0.8$, $\rho = 1/1836$, $v_{te} = 0.05$, $v_{ti} = 0.001$ and $\gamma_0 = 1$;

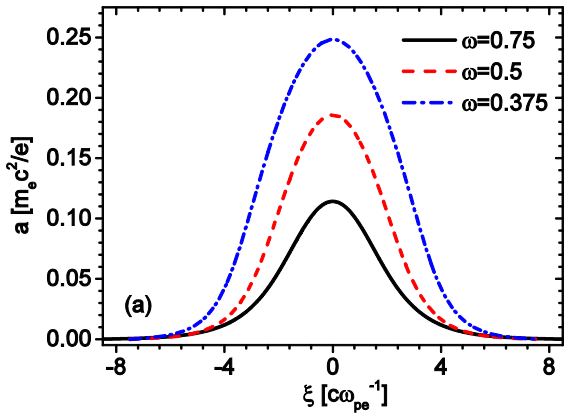

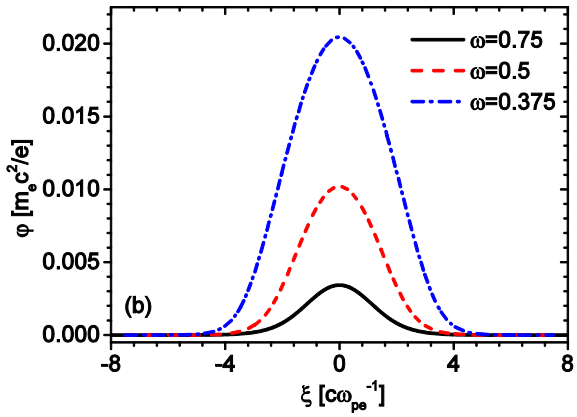

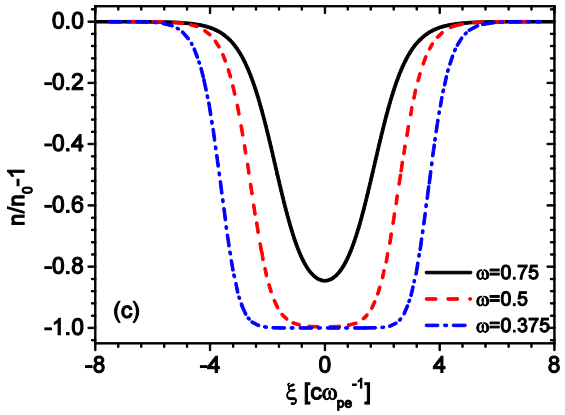

Fig. 5.14. The a) soliton envelope, b) scalar potential and c) density for different soliton frequencies in quasi-neutral approximation. The parameters are $\omega_{ce} = 0.15$, $\rho = 1/1836$, $v_{te} = 0.05$, $v_{ti} = 0.001$ and $\gamma_0 = 1$.

5.4 Numerical methods

In this section, we introduce the numerical methods we have used in solving the soliton equations and computing the manifolds: shooting and rational spectral methods Basically, for simplified 2D Hamiltonian system, the shooting method can give a sufficiently accurate result; however for 4D systems the accuracy decreases due to the temperature effects. As a result, the electron density is usually difficult to calculate correctly. Hence, in 4D systems, we adopt the combination of shooting and rational spectral methods to get a high accuracy. In addition, when the temperature is low, the initial guesses for the shooting method should be close enough to the real values to ensure convergence, which is generally too difficult to get. In this case, we use the numerical continuation of temperature based on the implicit function theorem.

5.4.1 Numerical continuation of temperature for shooting method

Mathematically, computing the homoclinic or heteroclinic orbits involves solving the nonlinear differential equations (4.19) – (4.23) with boundary conditions at the infinity space. It is frequently replaced by one on a finite domain and then the system is solved by the standard method such as multiple shooting methods or the spline collocation methods. In this work, we reduce the system to the solution of an initial value problem by the shooting method. Let $\boldsymbol{Y} = (\varphi, a)$ then $\boldsymbol{Y}$ satisfies,

$$\boldsymbol{Y}''(\xi) = \begin{bmatrix} n_e - n_i \\ -\left(\bar{\omega}^2 - \bar{k}^2 \frac{a_0^4}{a^4}\right) a + \gamma_0^2 \left(n_e \frac{p_{e\perp}}{r_e} - n_i \frac{p_{i\perp}}{r_i}\right) \end{bmatrix} \tag{5.45}$$

with boundary conditions,

$$\boldsymbol{Y}(\xi_1) = \boldsymbol{A}; \qquad \boldsymbol{Y}(\xi_2) = \boldsymbol{B}. \tag{5.46}$$

If the solution is symmetric, $\xi_{1,2} \to \pm\infty$, $\boldsymbol{A}, \boldsymbol{B} \to (0, a_0)$; If the solution is antisymmetric, $\xi_1 \to -\infty$, $\boldsymbol{A} \to (0, -a_0)$ and $\xi_2 \to +\infty$, $\boldsymbol{B} \to (0, a_0)$. Now we assume $\widetilde{\boldsymbol{Y}}$ is the solution of Eq. (5.45) with initial conditions,

$$\widetilde{\boldsymbol{Y}}(\xi_1) = \boldsymbol{A}; \qquad \widetilde{\boldsymbol{Y}}'(\xi_1) = \boldsymbol{C}. \tag{5.47}$$

Let $\boldsymbol{F}(\boldsymbol{C}) = \widetilde{\boldsymbol{Y}}(\xi_2; \boldsymbol{C}) - \boldsymbol{B}$. Then if $\boldsymbol{F}(\boldsymbol{C}^*) = 0$, $\tilde{Y}$ is the also solution of Eq. (5.45) with boundary condition (5.46). The $\boldsymbol{C}^*$ can be found through the Newton's method,

$$\boldsymbol{C}^{n+1} = \boldsymbol{C}^n - [\boldsymbol{F}'(\boldsymbol{C}^n)]^{-1} \boldsymbol{F}(\boldsymbol{C}^n) \tag{5.48}$$

This is the general idea for shooting method. For 2D Hamiltonian systems, e.g. Eq. (5.5) or Eq. (5.40), this scheme works well since the requirement for the initial guess $\boldsymbol{C}^0$ is undemanding. However, for 4D systems, the guess $\boldsymbol{C}^0$ becomes rigorous due to the presence of temperature term, e.g. $v_{te}^2 \ln n_e$ in Eq. (4.23).

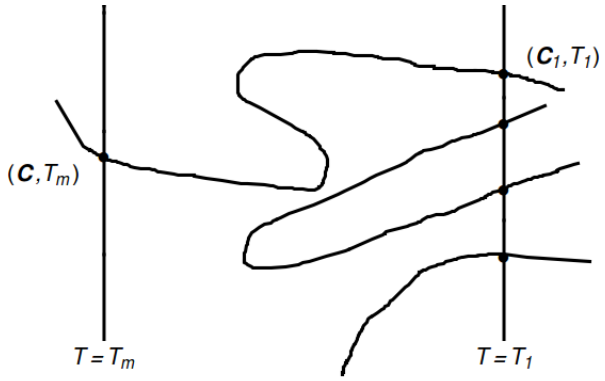

Fig. 5.15. Sketches for different possibilities for the curve $c(s)$. Along the curve $\boldsymbol{K}(\boldsymbol{C}, T) \equiv 0$.

Any numerical error induced on the right hand side of Eq. (4.23) will be amplified by v_{te}^2 and the exponential function. Hence, $\boldsymbol{C}^0$ should be close enough to the real values to ensure convergence. To find a good guess of $\boldsymbol{C}^0$, we use the method of numerical continuation of temperature [91]. The basic idea is simple: we first use a large enough temperature T_1 to get the $\boldsymbol{C}_1^n$; then the temperature is decreased step by step to the desired value T_2; we search $\boldsymbol{C}_{k+1}^0$ in the neighbor of $\boldsymbol{C}_k^n$ accordingly. Mathematically, we can choose the global homotopy,

$$\boldsymbol{K}(\boldsymbol{C}, T) = \boldsymbol{F}(\boldsymbol{C}) - \frac{T - T_m}{T_1 - T_m}\boldsymbol{F}(\boldsymbol{C_1}) \tag{5.49}$$

Here $\boldsymbol{C_1}$ is the initial conditions for temperature T_1 and the desired temperature is T_m. Notice that $\boldsymbol{K}(\boldsymbol{C_1}, T_1) = 0$ and $\boldsymbol{K}(\boldsymbol{C}, T_m) = \boldsymbol{F}(\boldsymbol{C})$. Hence we can trace the implicitly defined curve $c(s)$ by $\boldsymbol{K}(\boldsymbol{C}, T) = 0$ from $(\boldsymbol{C_1}, T_1)$ to $(\boldsymbol{C}, \boldsymbol{T_m})$. The existence of $c(s)$ is ensured by the Implicit Function Theorem, namely if $(\boldsymbol{C_1}, T_1)$ is a regular zero point of $\boldsymbol{K}$, then a curve $c(s)$ with initial value $c(0) = (\boldsymbol{C_1}, T_1)$ and tangent $\dot{c}(0) \neq 0$ will exist at least locally on some open interval around zero. Here the curve $c(s)$ is parametrized with respect to the parameter s, e.g. the temperature T. At each temperature step T_{k+1}, the value of $\boldsymbol{C}_{k+1}$ can be calculated by the Newton's method using $\boldsymbol{C}_k$ as starting values,

$$\boldsymbol{C}_{k+1} = \boldsymbol{C}_k - [\boldsymbol{K}'(\boldsymbol{C}_k, T_{k+1})]^{-1}\boldsymbol{K}(\boldsymbol{C}_k) \tag{5.50}$$

Some sketches of the curve $c(s)$ are shown in Fig. 5.15. Along the curve $\boldsymbol{K}(\boldsymbol{C}, T) \equiv 0$. Generally, there should be some boundary conditions which prevent the curve from running to infinity before intersecting the homotopy level $T = T_m$, or returning back to level $T = T_1$. Furthermore, this scheme will fail when the turning points of the curve with respect to the parameter T are encountered. This is attributed to the fact that the parameterizable with respect to T is not good enough. In this case, other suitable parameters e.g. the arclength of the curve s, may be chosen. However, in this work, we find the parameterizable with respect to T works well even without any boundary conditions.

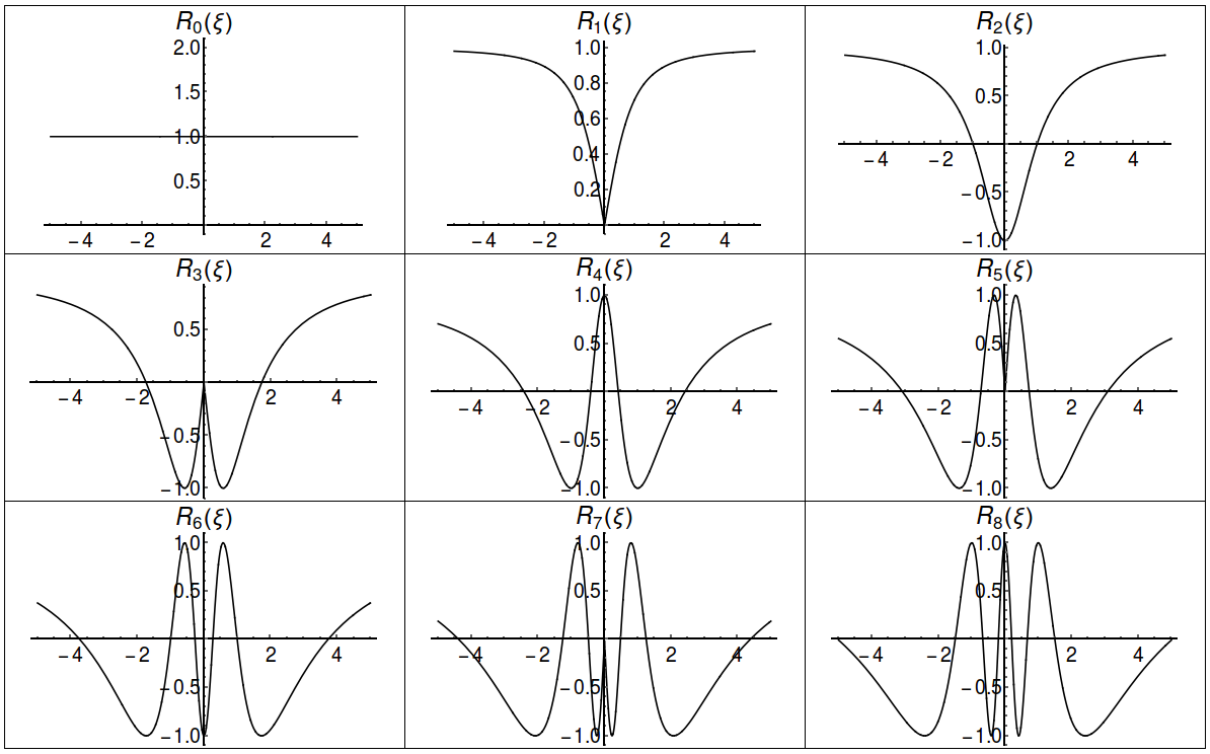

Fig. 5.16. The first nine plots of $R_k(\xi)$. $k = 0,1,\cdots 8$.

5.4.2 Rational spectral method

Though we have used the continuation of temperature to find the good guess of $\boldsymbol{C}^0$, sometimes the density is still difficult to calculate accurately, specifically at the shooting boundary where the scalar potential is usually small. (E.g. see Fig. C. 1 in Appendix C) In this case, the rational spectral methods are used and the shooting result is used to build up an initial input for the rational spectral scheme. The rational spectral scheme can transfer the two coupled second order nonlinear differential equations into nonlinear algebraic equations. The nonlinear algebraic equations are then solved by the Newton's method. The principles of the rational spectral method are as follows: assuming at certain collocation points ξ_j ($0 \le j \le M+1$, where M is an integer), the solutions can be expressed as, (we have neglected the ion's motion)

$$\varphi(\xi) = \sum_{k=0}^{M+1} c_k R_k(\xi); \qquad a(\xi) = \sum_{k=0}^{M+1} d_k R_k(\xi). \tag{5.51a}$$

$$p_{e\perp}(\xi) = \sum_{k=0}^{M+1} e_k R_k(\xi); \qquad \gamma_e(\xi) = \sum_{k=0}^{M+1} f_k R_k(\xi). \tag{5.51b}$$

Here $R_k(\xi)$ is basis, e.g. the mapped Chebyshev polynomials,

$$R_k(\xi) = \cos(k \cot^{-1} \xi); \qquad k = 0,1,2, \ldots M+1 \tag{5.52}$$

It can return to the usual Chebyshev polynomials $T_k(t)$ through the transformation $t = \xi/\sqrt{1+\xi^2}$. $R_k(\xi)$ is orthogonal since,

$$\int_{-\infty}^{+\infty} \frac{1}{1+\xi^2} R_m(\xi) R_n(\xi) d\xi = \frac{\pi}{2} d_n \delta_{m,n}; \qquad \text{with } d_n = \begin{cases} 2 & n = 0 \\ 1 & n \geq 1 \end{cases} \tag{5.53}$$

Here $\delta_{m,n}$ is the Kronecker delta. The first nine plots of $R_k(\xi)$ are shown in Fig. 5.16. It can be seen that $R_k(\xi)$ well reproduce the soliton structures and that is the reason why we use them as the bases. The collocation points are chosen as,

$$\xi_j = \cot\left(\frac{j\pi}{M+1}\right); \qquad 1 \leq j \leq M \tag{5.54}$$

Note that $\xi_0 = +\infty$ and $\xi_{M+1} = -\infty$; $R_k(\xi_0) = 1$ and $R_k(\xi_{M+1}) = (-1)^k$. Hence, by choosing this kind of collocation points, we do not need to truncate the differential equations into finite intervals. Using Eqs. (5.51) and (5.54), we find,

$$\begin{aligned} &\varphi(\xi_j) = \sum_{k=0}^{M+1} c_k m_{jk}; \qquad a(\xi_j) = \sum_{k=0}^{M+1} d_k m_{jk}; \qquad p_{e\perp}(\xi_j) = \sum_{k=0}^{M+1} e_k m_{jk}; \\ &\gamma_e(\xi_j) = \sum_{k=0}^{M+1} f_k m_{jk}; \qquad \varphi''(\xi_j) = -\sum_{k=0}^{M+1} c_k D_{jk}; \qquad a''(\xi_j) = -\sum_{k=0}^{M+1} d_k D_{jk}. \end{aligned} \tag{5.55}$$

Here m_{jk} and D_{jk} are expressed as,

$$\begin{cases} m_{jk} = \cos\left(\dfrac{kj\pi}{M+1}\right) \\ D_{jk} = k\left[k\cos\left(\dfrac{kj\pi}{M+1}\right) + 2\cot\left(\dfrac{j\pi}{M+1}\right)\sin\left(\dfrac{kj\pi}{M+1}\right)\right]\sin^4\left(\dfrac{j\pi}{M+1}\right) \end{cases} \tag{5.56}$$

Substituting the above equations into Eqs. (4.20) - (4.23) and use the boundary conditions, we can change the second order nonlinear differential equations into $4(M+2)$ nonlinear algebraic equations,

$$\mathbf{0}=\boldsymbol{G}\equiv\begin{cases}\varphi(+\infty)=\sum_{k=0}^{M+1}c_k\\ \sum_{k=0}^{M+1}d_k\,D_{jk}-\left[\bar{\omega}^2\left(\sum_{k=0}^{M+1}d_k\,m_{jk}\right)-\frac{\bar{k}^2a_0^4}{\left(\sum_{k=0}^{M+1}d_k\,m_{jk}\right)^3}\right]+\gamma_0^2\left(1-\sum_{k=0}^{M+1}c_k\,D_{jk}\right)\frac{\sum_{k=0}^{M+1}e_km_{jk}}{\sum_{k=0}^{M+1}f_km_{jk}}\\ \varphi(-\infty)=\sum_{k=0}^{M+1}(-1)^kc_k\\ a(+\infty)-a_0=\sum_{k=0}^{M+1}d_{ik}-a_0\\ \sum_{k=0}^{M+1}e_km_{jk}-\sum_{k=0}^{M+1}d_k\,m_{jk}-\bar{\alpha}\gamma_0^2\frac{\sum_{k=0}^{M+1}e_km_{jk}}{\sum_{k=0}^{M+1}f_km_{jk}}\\ a(-\infty)-a_0=\sum_{k=0}^{M+1}(-1)^kd_{ik}-a_0\\ p_{e\perp}(+\infty)-p_{e0}=\sum_{k=0}^{M+1}e_k-p_{e0}\\ v_{te}^2\ln\left(1-\sum_{k=0}^{M+1}c_k\,D_{jk}\right)-\sum_{k=0}^{M+1}c_k\,m_{jk}-\frac{1}{2}\bar{\alpha}\gamma_0^2\left(\frac{\sum_{k=0}^{M+1}e_km_{jk}}{\sum_{k=0}^{M+1}f_km_{jk}}\right)^2+\frac{\sum_{k=0}^{M+1}f_km_{jk}}{\gamma_0^2}+c_{e0}\\ p_{e\perp}(-\infty)-p_{e0}=\sum_{k=0}^{M+1}(-1)^ke_k-p_{e0}\\ \gamma_e(+\infty)-\gamma_{e0}=\sum_{k=0}^{M+1}f_{ik}-\gamma_{e0}\\ \gamma_0^2\left[1+\left(\sum_{k=0}^{M+1}e_km_{jk}\right)^2\right]-\left(\sum_{k=0}^{M+1}f_km_{jk}\right)^2\\ \gamma_e(-\infty)-\gamma_{e0}=\sum_{k=0}^{M+1}(-1)^kf_{ik}-\gamma_{e0}\end{cases}\tag{5.57}$$

Here $1\le j\le M$ and a_0,p_{e0},γ_{e0} are the boundary values. The last but one equation in Eq. (5.57) comes from the identity $\gamma_0^2(1+p_{e\perp}^2)\equiv\gamma_e^2$. Eq. (5.57) consists of $4(M+2)$ nonlinear algebraic equations with $4(M+2)$ unknowns $\boldsymbol{x_k}=(c_k,d_k,e_k,f_k)$ $(0\le k\le M+1)$. It can be solved by the Newton's iteration,

$$\boldsymbol{x_k^{(n+1)}}=\boldsymbol{x_k^{(n)}}-\left[\boldsymbol{G}'\left(\boldsymbol{x_k^{(n)}}\right)\right]^{-1}\boldsymbol{G}\left(\boldsymbol{x_k^{(n)}}\right)\tag{5.58}$$

Notice that we have imposed the symmetric boundary conditions $\varphi(\pm\infty)=0,a(\pm\infty)=a_0$ and the symmetry of the solutions can help us to reduce the coefficients by a factor of two. For example, for symmetric solutions, the coefficients with odd indexes are zero; for asymmetric solutions all the coefficients should be calculated. The Jacobi matrix is,

$G'(\boldsymbol{x_k}) =$

$$\begin{bmatrix}
1 & 0 & 0 & 0 \\
-\frac{[\sum(e_k-d_k)m_{jk}]}{\bar{\alpha}}D_{ji} & D_{ji}-\left(\bar{\omega}^2+\frac{3\bar{k}^2a_0^4}{\left(\sum d_k m_{jk}\right)^4}+\frac{1-\sum c_k D_{jk}}{\bar{\alpha}}\right)m_{ji} & \frac{1-\sum c_k D_{jk}}{\bar{\alpha}}m_{ji} & 0 \\
(-1)^i & 0 & 0 & 0 \\
0 & 1 & 0 & 0 \\
0 & -m_{ji} & \left(1-\frac{\bar{\alpha}\gamma_0}{\sum f_k m_{jk}}\right)m_{ji} & \frac{\bar{\alpha}\gamma_0\sum e_k m_{jk}}{\left(\sum f_k m_{jk}\right)^2}m_{ji} \\
0 & (-1)^i & 0 & 0 \\
0 & 0 & 1 & 0 \\
\frac{-v_{te}^2 D_{ji}}{1-\sum c_k D_{jk}}-m_{ji} & \frac{\sum(e_k-d_k)m_{jk}}{\bar{\alpha}\gamma_0^2}m_{ji} & -\frac{\sum(e_k-d_k)m_{jk}}{\bar{\alpha}\gamma_0^2}m_{ji} & \frac{m_{ji}}{\gamma_0} \\
0 & 0 & (-1)^i & 0 \\
0 & 0 & 0 & 1 \\
0 & 0 & 2\left(\sum e_k m_{jk}\right)m_{ji} & -2\left(\sum f_k m_{jk}\right)m_{ji} \\
0 & 0 & 0 & (-1)^i
\end{bmatrix} \tag{5.59}$$

Here the summation is on k $(0 \le k \le M+1)$ and $0 \le i \le M+1$, $1 \le j \le M$. In our calculations, we found M around 200~250 can give a good result.

As discussed before, using the Newton's method needs a good initial guess of the solution to ensure convergence. In this scheme, the initial guess for single hump solitons is built up by the shooting results and throwing away high order coefficients; for multi-hump solitons (which will be discussed in chapter 6), the initial guess is built up by single hump soliton results. Once we have a good initial guess, this scheme gives an accurate solution that can be used to build up guesses for other parameters. (See Appendix C)

5.4.3 Computing the manifolds

In section 4.3.3 and Fig. (Fig. 5.6), we have shown the definition and examples of the stable and unstable manifolds. In this section, we introduce the general method for the numerical calculation of these manifolds. For illustrative purpose, we consider the case of the manifolds of a saddle point. Furthermore, we only present the calculation of the unstable manifold. The stable manifold can be computed as an unstable manifold when ξ is reversed. The definition of unstable manifolds Eq. (4.44) suggests a direct method for computing $W^u(Q_0)$. That is integrating Eq. (4.29) by the initial conditions,

$$(a, a', \varphi, \varphi') = Q_0 + \varepsilon_1 X_1 + \varepsilon_2 X_3 \tag{5.60}$$

Here $X_{1,3}$ are the unstable eigenvectors of Q_0 corresponding to the positive eigenvalues $\lambda_{1,3}$ given by Eq. (5.26). ε_1, ε_2 are small parameters controlling the distance of the initial position to the fixed point in the linear subspace spanned by $X_{1,3}$. ε_1, ε_2 are usually taken as $\varepsilon_1 = \varepsilon \sin\theta$ and $\varepsilon_2 = \varepsilon \cos\theta$ with ε a small parameter. Then the initial points form a circle around Q_0. In principle, computing solutions for a sufficient number of θ will result in an approximation of the unstable manifolds. For 1D manifold, e.g. $X_3 \equiv 0$, this method works well since it boils down to evolving two points at distance ε from Q_0 under the flow $\boldsymbol{\phi}^{\xi}(\boldsymbol{x})$. However, for 2D or higher dimensional manifold, the above method usually gives very poor results. This is because the initial points will typically deform dramatically under $\boldsymbol{\phi}^{\xi}(\boldsymbol{x})$, specifically they will stretch out along the strong unstable directions. Hence, spacing the initial points around the circle is important. In this case the pseudo arclength continuation is adopted and one can read Ref88 for the details.

5.5 Summary

In this chapter, we have systematically studied the bright soliton formation in strongly magnetized plasmas. Based on the dynamical systems theory, the parametric regions of magnetic field and soliton frequency for the existence of solitons in both cold and warm plasmas are identified. In cold plasmas, where the system is reduced to 2D, an additional restriction on the magnetic field and soliton frequency arises from the non-negative condition of the density. This condition disappears in warm plasmas. The ion's effects on the soliton formation are also investigated. It is found that for the RCP soliton, the ion's motion plays an important role in determining the lower limit of the soliton frequency, especially when the magnetic field is opposite to the laser propagation direction.

The coupled soliton equations are then solved numerically by the shooting method in the cold plasmas and the combination of shooting and rational spectral algorithm in the warm plasmas. The numerical calculations show that in the limit of immobile ions, the soliton tends to be peaked and stronger as the magnetic field increases and it becomes broader and smaller as the temperature increases. However, under the quasi-neutral approximation, it is found that the soliton increases with increasing temperature. Moreover, the quasi-neutral approximation removes the density humps on the soliton wings appeared in the ion fixed case.

6. Dark solitons in magnetized plasmas

Unlike the bright solitons which are spontaneously excited during the laser plasmas interactions, the generation of dark solitons remains an open problem. However, the Maxwell-fluid model presented in chapter 4 also supports the dark soliton solutions, which could give us some clues for the excitation of dark solitons in experiments. Sanchez et al [64] suggested that dark solitons could be generated by the interactions between a long pulse laser and a bright soliton excited by a short pulse laser. In theory, the dark solitons have been studied by several authors in unmagnetized plasmas, where the small amplitude dark soliton solutions [57] are obtained and solitons with one hump in the scalar potential profile and multi humps in the vector potential profile are observed [64]. However, to the author's best knowledge, the dark solitons in magnetized plasmas appear here for the first time. In this chapter, the dark solitons without ion's motion in cold plasmas are first discussed. In this case the system is simplified to 2D. The parametric region of magnetic field and soliton frequency and wavenumber for the existence of dark solitons is identified. The discussion is then extended to the warm plasmas case, where dark solitons with multiple humps in both the scalar and vector potential profiles are observed. We rewrite the dark soliton equations,

$$\theta' = \bar{k}\left(1 - \frac{a_0^2}{a^2}\right); \tag{6.1}$$

$$\varphi'' = n_e - n_i; \tag{6.2}$$

$$a'' + \left(\bar{\omega}^2 - \bar{k}^2\frac{a_0^4}{a^4}\right)a = \gamma_0^2\left(n_e\frac{p_{e\perp}}{r_e} - n_i\frac{p_{i\perp}}{r_i}\right); \tag{6.3}$$

$$p_{e\perp} - a = \bar{\alpha}\gamma_0^2\frac{p_{e\perp}}{\gamma_e}; \qquad p_{i\perp} + \rho a = -\rho\bar{\alpha}\gamma_0^2\frac{p_{i\perp}}{\gamma_i} \tag{6.4}$$

$$v_{te}^2\ln n_e = \varphi + \frac{1}{2}\bar{\alpha}\gamma_0^2\frac{p_{e\perp}^2}{\gamma_e^2} - \frac{\gamma_e}{\gamma_0^2} - c_{e0}; \quad v_{ti}^2\ln n_i = -\rho\varphi - \frac{1}{2}\rho\bar{\alpha}\gamma_0^2\frac{p_{i\perp}^2}{\gamma_i^2} - \frac{\gamma_i}{\gamma_0^2} - c_{i0}. \tag{6.5}$$

Here $\bar{\alpha} = \omega_{ce}/\bar{\omega}$ with $\omega_{ce} = eB_0/(m_e c)$ the electron cyclotron frequency; $\bar{\omega} = \gamma_0^2(\omega - kV)$, $\bar{k} = \gamma_0^2(k - V\omega/c^2)$ are the modified soliton frequency and wavenumber; $\rho = m_e/m_i$ is the electron-ion mass ratio; a_0, γ_{s0} and $p_{s0\perp}$are the soliton amplitude, relativistic factor and transverse momentum for s[th] particle $(s = e, i)$ at the left boundary $\xi \to -\infty$. $c_{e0} = \bar{\alpha}\gamma_0^2 p_{e0\perp}^2/(2\gamma_{e0}^2) - \gamma_{e0}/\gamma_0^2$, $c_{i0} = -\rho\bar{\alpha}\gamma_0^2 p_{i0\perp}^2/(2\gamma_{i0}^2) -$

γ_{i0}/γ_0^2 and $\gamma_0^2 = 1/(1 - V^2/c^2)$. Notice that for dark solitons V is not the group velocity since the phase modulation θ is non-trivial.

6.1 Dark solitons in cold plasmas

In cold plasmas, neglecting the ions the scalar potential φ and electron density n_e can be eliminated and the dark soliton equations are simplified to,

$$\frac{\gamma_0^2}{\gamma_e^2}a'' + \left(\bar{\omega}^2 - \bar{k}^2\frac{a_0^4}{a^4}\right)a = \frac{\gamma_0^2}{r_e - \bar{\alpha}\gamma_0^2}\left(1 + \frac{\gamma_0^2}{\gamma_e^3 - \bar{\alpha}\gamma_0^4}a'^2\right)a. \tag{6.6}$$

The Hamiltonian $H(a, a'\gamma_0^2/\gamma_e^2)$ is,

$$H\left(a, \frac{\gamma_0^2}{\gamma_e^2}a'\right) = \frac{1}{2}\left(\frac{\gamma_0^2}{\gamma_e^2}a'^2 + \bar{\omega}^2a^2 + \bar{k}^2\frac{a_0^4}{a^2}\right) - \left(\frac{1}{2}\bar{\alpha}\gamma_0^2\frac{\gamma_0^2}{\gamma_e^2} + \gamma_e\right). \tag{6.7}$$

6.1.1 Parametric domain for the existence of dark solitons

Since the system is 2D, the existence of dark solitons requests the fixed points $Q_0^{\pm}, Q_*^{\pm}$ to be saddles. The corresponding eigenvalues are,

$$\lambda^2 = \frac{\gamma_e^2}{\gamma_0^2}\left[\frac{\gamma_0^4}{\gamma_e^3 - \bar{\alpha}\gamma_0^4} - \left(\bar{\omega}^2 + 3\bar{k}^2\right)\right]\Bigg|_{Q_0^{\pm}, Q_*^{\pm}} \tag{6.8}$$

At $Q_0^{\pm}$, $\gamma_e = \gamma_{e0} = \gamma_0^2\left[\bar{\alpha} + 1/\left(\bar{\omega}^2 - \bar{k}^2\right)\right]$; at $Q_*^{\pm}$, $\gamma_e^2 = \gamma_0^2[1 + a^{*2}\gamma_e^2/(\gamma_e - \bar{\alpha}\gamma_0^2)]$ with a^* satisfies Eq. (4.36).

First let's discuss the fixed point $Q_0^{\pm}$. The saddle condition requests,

$$\frac{1}{\gamma_0^2\left[\bar{\alpha} + 1/\left(\bar{\omega}^2 - \bar{k}^2\right)\right]^3 - \bar{\alpha}} > \left(\bar{\omega}^2 + 3\bar{k}^2\right) > 0. \tag{6.9}$$

Notice that for unmagnetized plasmas, condition (6.9) is never satisfied. This can be verified by setting $\bar{\alpha} = 0$ in Eq. (6.8). Since $\bar{\omega}^2 = \bar{k}^2 + \gamma_0^2/\gamma_{e0}$ in this case, we find at $Q_0^{\pm}$,

$$\lambda^2 = \frac{\gamma_{e0}^2}{\gamma_0^2}\left[\frac{\gamma_0^2}{\gamma_{e0}}\left(\frac{\gamma_0^2}{\gamma_{e0}^2} - 1\right) - 4\bar{k}^2\right] < 0 \tag{6.10}$$

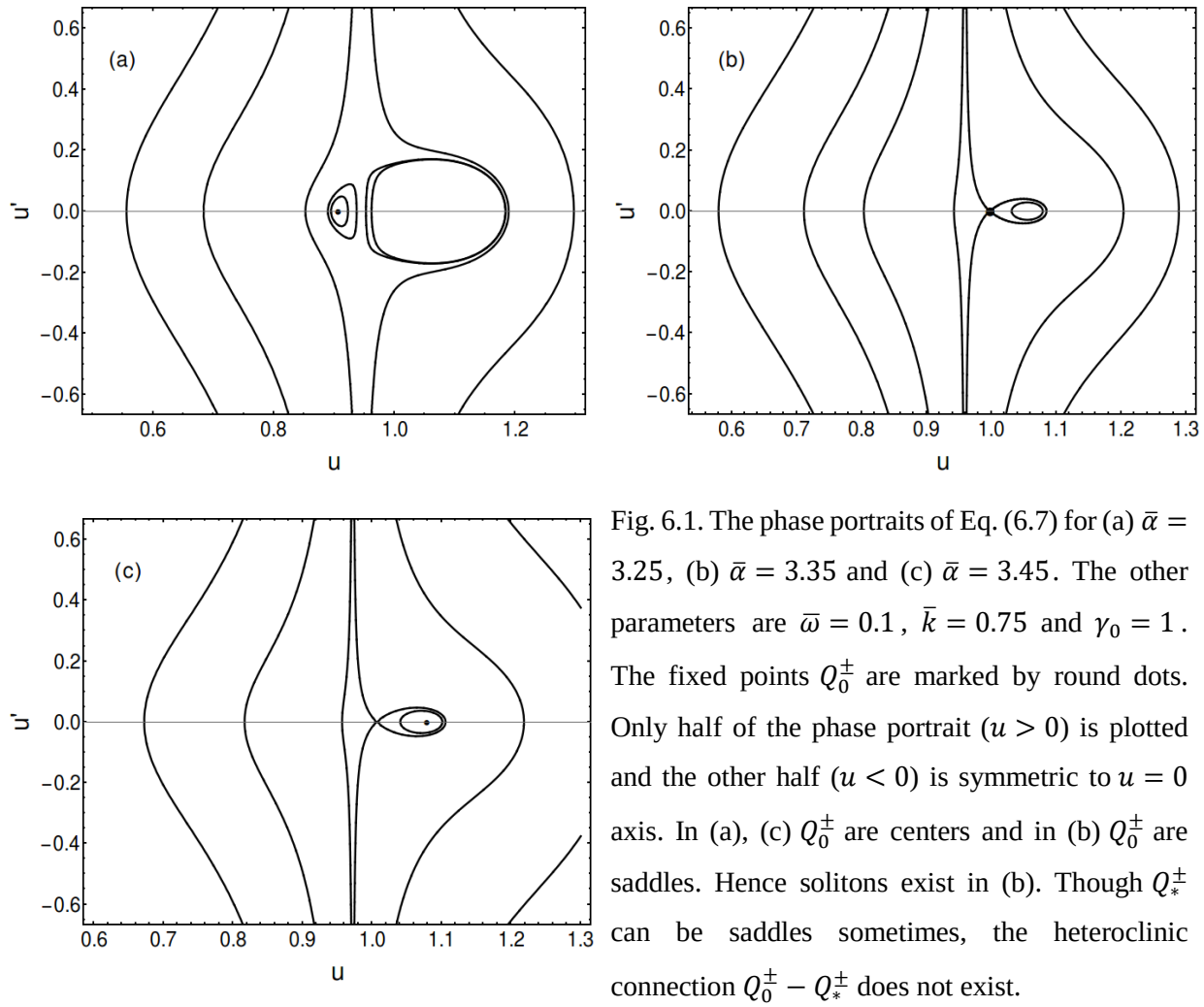

Fig. 6.1. The phase portraits of Eq. (6.7) for (a) $\bar{\alpha} = 3.25$, (b) $\bar{\alpha} = 3.35$ and (c) $\bar{\alpha} = 3.45$. The other parameters are $\bar{\omega} = 0.1$, $\bar{k} = 0.75$ and $\gamma_0 = 1$. The fixed points $Q_0^{\pm}$ are marked by round dots. Only half of the phase portrait ($u > 0$) is plotted and the other half ($u < 0$) is symmetric to $u = 0$ axis. In (a), (c) $Q_0^{\pm}$ are centers and in (b) $Q_0^{\pm}$ are saddles. Hence solitons exist in (b). Though $Q_*^{\pm}$ can be saddles sometimes, the heteroclinic connection $Q_0^{\pm} - Q_*^{\pm}$ does not exist.

Hence dark solitons in unmagnetized cold plasmas do not exist. For magnetized plasmas, it can be proved that if $\bar{k} = 0$ the dark soliton solution also does not exist. In this case $\gamma_e^3 > \gamma_e\gamma_0^2 = \bar{\alpha}\gamma_0^4 + \gamma_0^4/\bar{\omega}^2$, thus,

$$\lambda^2 = \frac{\gamma_e^2}{\gamma_0^2}\left[\frac{\gamma_0^4}{\gamma_e^3 - \bar{\alpha}\gamma_0^2} - \bar{\omega}^2\right] < 0. \tag{6.11}$$

Therefore, in cold plasmas with immobile ions dark solitons only happen with $\bar{k} \neq 0$ and $\bar{\alpha} \neq 0$.

For the fixed points $Q_*^{\pm}$, it is difficult to determine their types directly from Eqs. (4.36) and (6.8), however we judge their types from the phase portraits (see Fig. 6.1). In Fig. 6.1, we show the phase portraits around $Q_0^{\pm}$ when $Q_0^{\pm}$ are centers (Fig. 6.1(a), (c)) and saddles (Fig. 6.1(b)). Here the transformation $a = \sinh u - \bar{\alpha}\gamma_0 \tanh u$ has been used and $Q_0^{\pm}$ are marked by round dots. Notice that only half of the phase portrait ($u > 0$) is plotted and the other half ($u < 0$) is symmetric to $u = 0$ axis. Also it should be

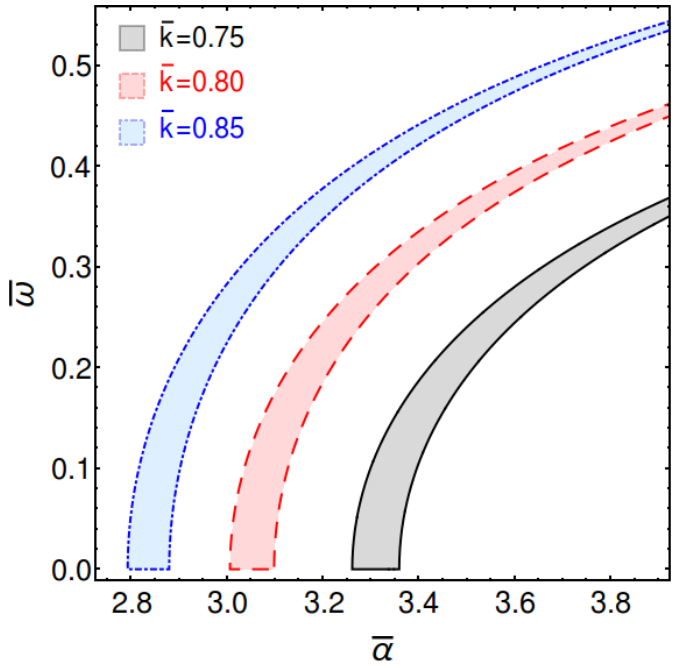

Fig. 6.2. The parametric domain of $(\bar{\alpha}, \bar{\omega})$ for the existence of dark solitons in cold plasmas with different wavenumbers. $\gamma_0 = 1$. As $\bar{k}$ decreases, the shaded area moves towards the right. When $\bar{k} \to 0$, the dark soliton does not exist.

mentioned that there are more than two additional fixed points $Q_*^{\pm}$ (see Fig. 4.1) and we only plot the phase structures near $Q_0^{\pm}$. This is fine since we are expecting to find the heteroclinic connections $Q_0^{\pm} - Q_*^{\pm}$ which request both $Q_0^{\pm}$ and $Q_*^{\pm}$ to be saddles at the same time. It can be seen that though $Q_*^{\pm}$ can be saddles sometimes (Fig. 6.1(c)), the heteroclinic connection $Q_0^{\pm} - Q_*^{\pm}$ does not exist. The soliton can only exist in Fig. 6.1(b).

In Fig. 6.2, we plot the parametric domain of $(\bar{\alpha}, \bar{\omega})$ for the existence of dark solitons in cold plasmas with different wavenumbers $\bar{k}$. The dark solitons can only exist in the shaded areas. Compared with Fig. 5.2 where the bright solitons have large volume in the parametric domain, the parametric volume for dark solitons is relatively small. For fixed soliton frequency $\bar{\omega}$, the magnetic field required for dark solitons increases as $\bar{k}$ decreases. If $\bar{k} \to 0$, the dark soliton does not exist which is consistent with Eq. (6.11).

6.1.2 Soliton envelops

In Fig. 6.3 and Fig. 6.4, we show the dark soliton envelop, scalar potential, density profile and the phase under different magnetic fields and soliton frequencies. The dark soliton amplitude at the infinity (background amplitude a_0) is totally determined by the magnetic field, soliton frequency and wavenumber through the relations $a_0^2 = (\gamma_{e0}^2/\gamma_0^2 - 1)(1 - \bar{\alpha}\gamma_0^2/\gamma_{e0})$ with $\gamma_{e0} = \gamma_0^2[1 + 1/(\bar{\omega}^2 - \bar{k}^2)]$. It can be seen that the dark soliton "amplitude" decreases with increasing magnetic field and decreasing soliton frequency. These tendencies are the opposite to the bright soliton case. Here the soliton "amplitude" is referred as the

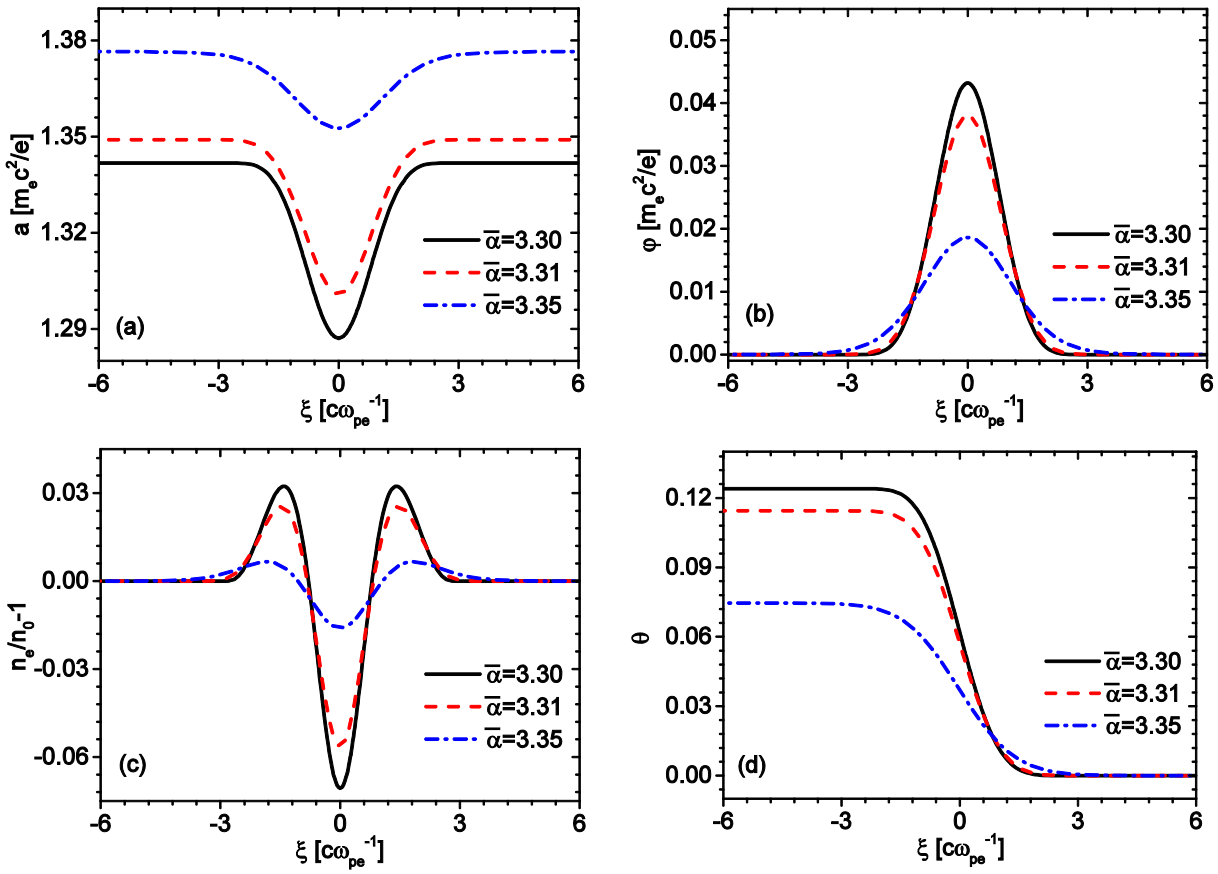

Fig. 6.3. The dark soliton a) envelope, b) scalar potential, c) electron density and d) phase for different magnetic fields in the cold plasmas. The parameters are $\bar{\omega} = 0.1$, $\bar{k} = 0.75$ and $\gamma_0 = 1$. Notice that though dark soliton with larger magnetic field has a smaller soliton amplitude, it has a higher background amplitude. Here the soliton amplitude is referred as the difference between the background amplitude at the infinity and the minimum at the center.

difference between the background amplitude at the infinity and the minimum amplitude at the center. The dependences of the soliton "amplitude" and background amplitude on the magnetic field are different, .e.g. though solitons with larger magnetic fields have smaller soliton "amplitudes", they possess higher background amplitudes.

In the presence of magnetic field, the ponderomotive force is $F \approx -[(\gamma_e^3 - \bar{\alpha}\gamma_0^4)/(\gamma_0^2\gamma_e^3)]\nabla\gamma_e$ (see Eq. (4.14)). In the weakly relativistic approximation $\gamma_e^2 \sim \gamma_0^2\left[1 + a^2/(1-\bar{\alpha}\gamma_0)^2\right]$. Hence,

$$F \approx -\frac{\gamma_e^3 - \bar{\alpha}\gamma_0^4}{2\gamma_e^4(1-\bar{\alpha}\gamma_0)^2}\nabla a^2$$

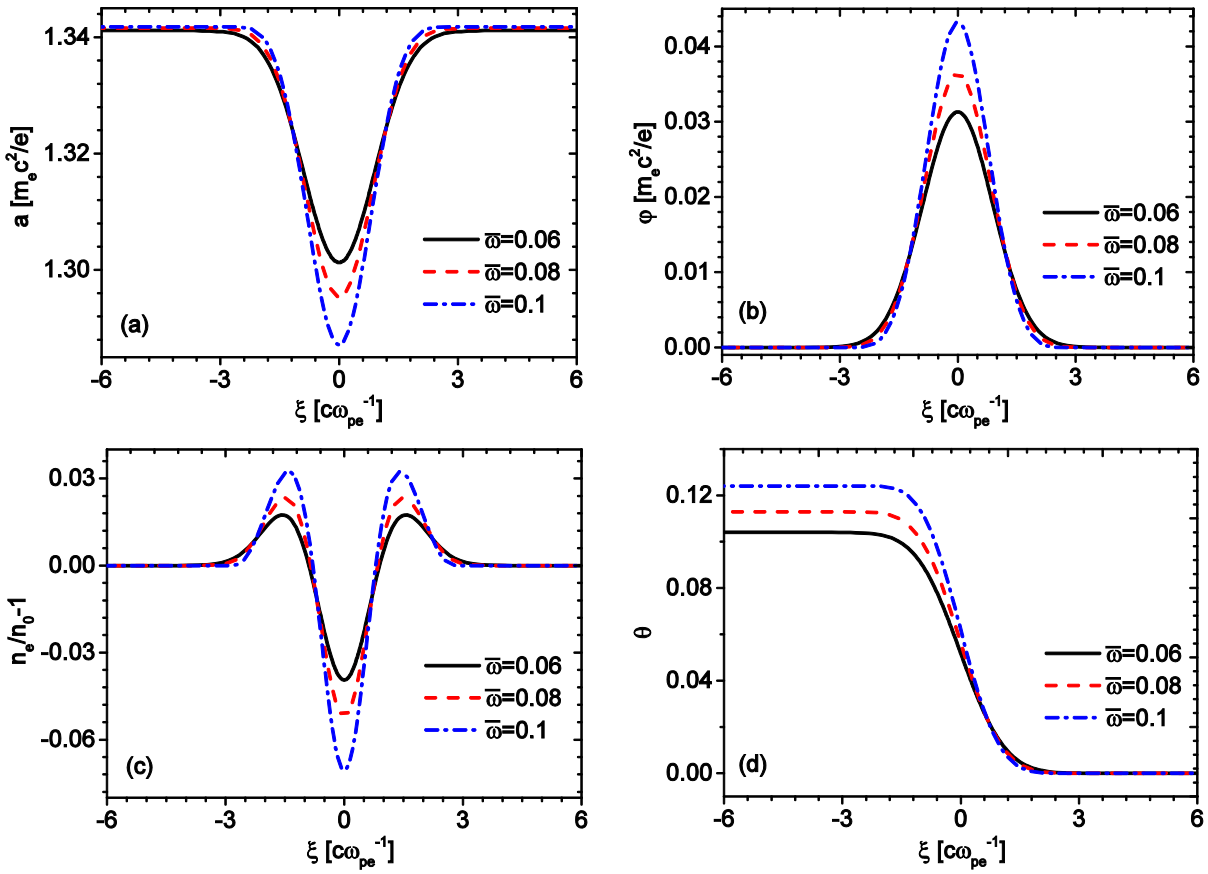

Fig. 6.4. The dark soliton a) envelope, b) scalar potential, c) electron density and d) phase for different soliton frequencies in the cold plasmas. The parameters are $\bar{\alpha} = 3.30$, $\bar{k} = 0.75$ and $\gamma_0 = 1$

For bright solitons $\bar{\alpha}\gamma_0 < 1$, the ponderomotive force is always along the lower intensity direction; however for dark solitons, $\gamma_e^3 - \bar{\alpha}\gamma_0^4$ can be negative, leading to an accumulation of the electron density at the larger laser intensity areas.

6.2 Dark solitons in warm plasmas

For warm plasmas, the Hamiltonian $H(a, a', \varphi, -\gamma_0^2\varphi')$ is,

$$H(a, a', \varphi, -\gamma_0^2\varphi') = \frac{1}{2}\left(a'^2 + \bar{\omega}^2 a^2 + \bar{k}^2\frac{a_0^4}{a^2} - \gamma_0^2\varphi'^2\right) + \gamma_0^2\left[v_{the}^2(n_e - 1) - \varphi\right] \qquad (6.12)$$

6.2.1 Temperature effects

The eigenvalues can be calculated from Eqs. (4.38) – (4.41),

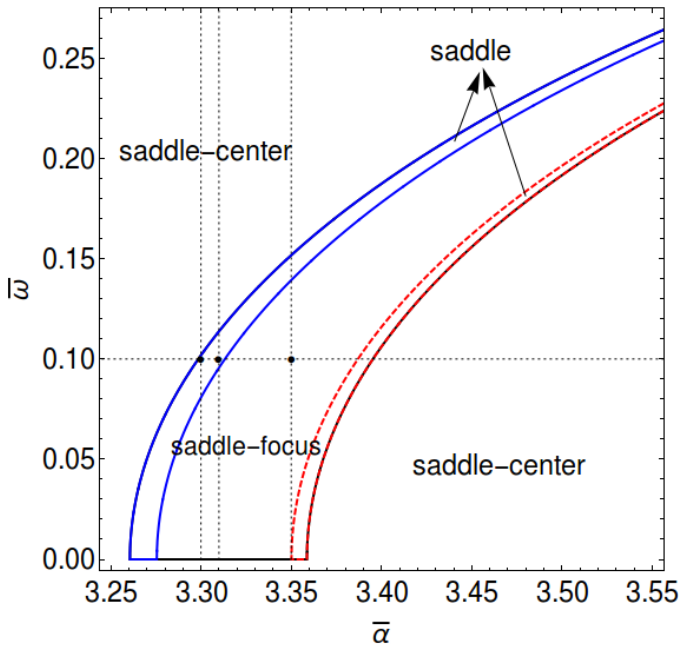

Fig. 6.5. The parametric domain of $(\bar{\alpha}, \bar{\omega})$ for the existence of dark solitons in warm plasmas with $\bar{k} = 0.75$, $v_{te} = 0.548$ and $\gamma_0 = 1$.

$$\lambda_{1-4}^2 = \pm\sqrt{\frac{1}{2}\left(\delta \pm \sqrt{\Delta}\right)} \tag{4.43}$$

with δ and Δ expressed as,

$$\begin{cases} \delta = J_{21} + J_{43} = \eta + \gamma_0^2/(v_{te}^2\gamma_e^2) \\ \Delta = (\eta - \mu_-^2)(\eta - \mu_+^2) \\ \delta^2 - \Delta = 4\eta/v_{te}^2 \end{cases} \tag{6.13}$$

Here $\eta = \gamma_0^4/(\gamma_e^3 - \bar{\alpha}\gamma_0^4) - \left(\bar{\omega}^2 + 3\bar{k}^2 a_0^4/a^4\right)$ and $\mu_\pm^2 = (\gamma_0 p_{e\perp}/\gamma_e \pm 1)^2/v_{te}^2$. A simple calculation shows that, the fixed points can be saddles, saddle-centers and saddle-foci but the focus type is impossible. This is because, the focus type needs $\delta < -\sqrt{\Delta} < 0$, which cannot be satisfied simultaneously. In the case of saddle and saddle-focus, both the stable and unstable manifolds are 2D, hence the soliton solutions are general. $\Delta = 0$ gives the condition that separates the saddle-focus and saddle domains and $\delta^2 = \Delta$ gives the separation condition between saddles and saddle-centers. At fixed points $Q_0^\pm$ they are,

$$\frac{\gamma_0^4}{\gamma_{e0}^3 - \bar{\alpha}\gamma_0^4} - \left(\bar{\omega}^2 + 3\bar{k}^2\right) = \frac{1}{v_{te}^2}\left(\sqrt{1 - \gamma_0^2/\gamma_{e0}^2} \pm 1\right)^2; \tag{6.14}$$

$$\frac{\gamma_0^4}{\gamma_{e0}^3 - \bar{\alpha}\gamma_0^4} - \left(\bar{\omega}^2 + 3\bar{k}^2\right) = 0. \tag{6.15}$$

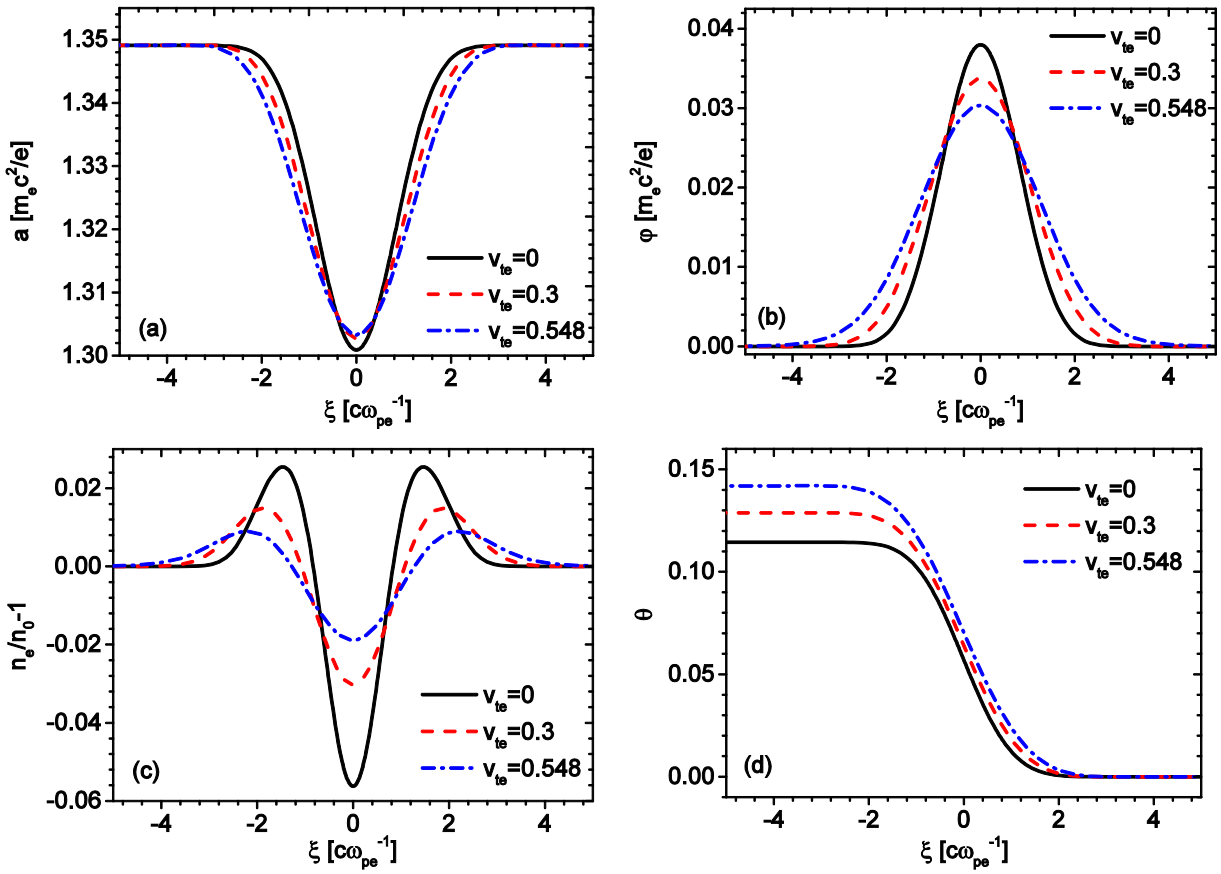

Fig. 6.6. The single hump dark soliton (a) envelop, (b) scalar potential, (c) density and (d) phase with different electron temperatures in warm plasmas for $\bar{\omega} = 0.1$, $\bar{k} = 0.75$, $\bar{\alpha} = 3.31$ and $\gamma_0 = 1$. Notice that the background soliton amplitude does not depends on the temperature. The parameter positions in $(\bar{\alpha}, \bar{\omega})$ space are marked by round dots in Fig. 6.5.

In Fig. 6.5 we show the parametric domain of $(\bar{\alpha}, \bar{\omega})$ for the existence of dark solitons in warm plasmas with $\bar{k} = 0.75$, $v_{te} = 0.548$ and $\gamma_0 = 1$. Comparing with Fig. 6.2, it is found that the saddle domain where the soliton exist in cold plasmas breaks up into one saddle-focus and two saddle domains. As the temperature increases, the left-upper saddle domain expands while the right-lower saddle domain shrinks. As $v_{te} \to \infty$, both the right-lower saddle and saddle-focus domains disappear and the left-upper saddle domain occupies the whole original saddle domain. If $v_{te} \to 0$, the left-upper saddle and saddle-focus domains vanish and the situation recovers to the cold plasmas case.

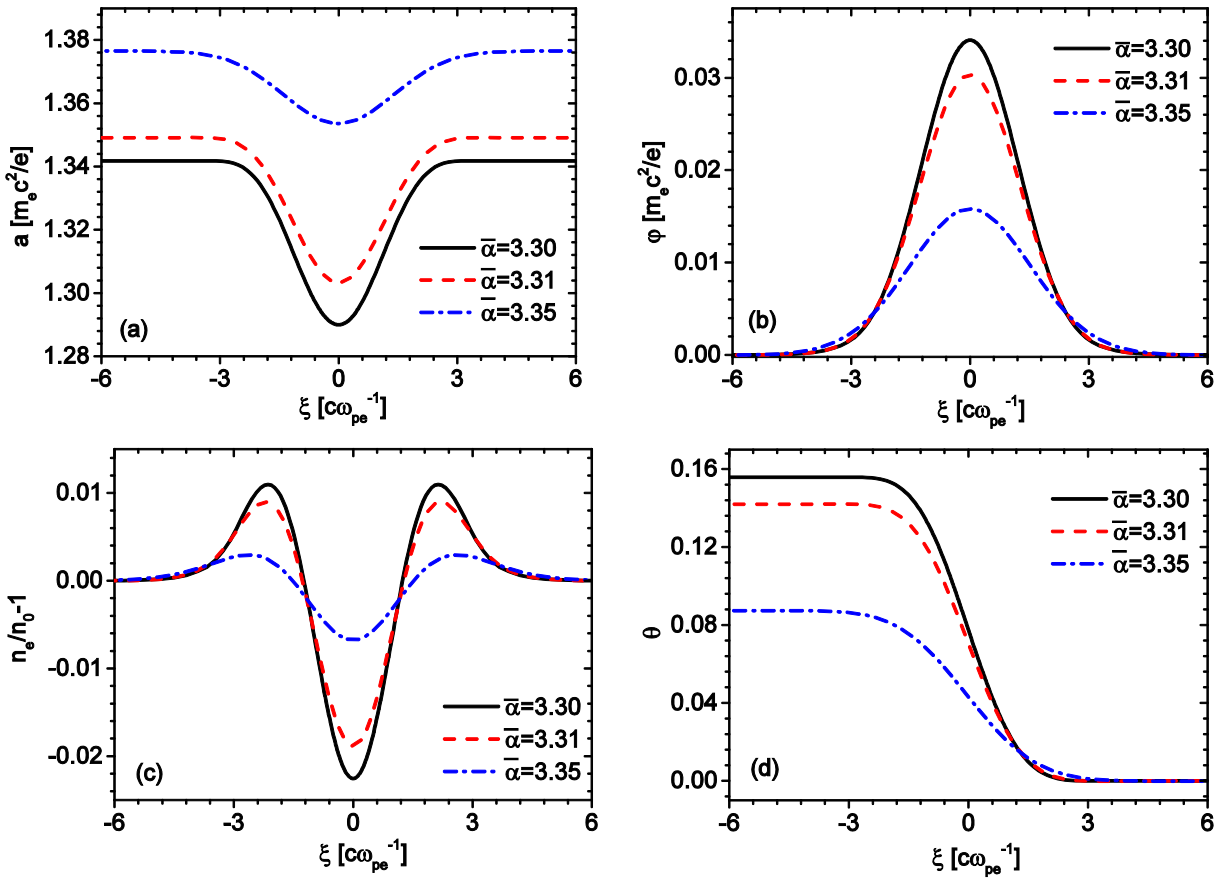

Fig. 6.7. The single hump dark soliton (a) envelop, (b) scalar potential, (c) density and (d) phase with different magnetic fields in warm plasmas for $\bar{\omega} = 0.1$, $\bar{k} = 0.75$, $v_{te} = 0.548$ and $\gamma_0 = 1$. The parameter positions in $(\bar{\alpha}, \bar{\omega})$ space are marked by round dots in Fig. 6.5.

6.2.2 Single hump dark solitons

In Fig. 6.6, Fig. 6.7 and Fig. 6.8 we have shown the numerical calculations of dark soliton envelops with different electron temperatures, magnetic fields and soliton frequencies, respectively. It can be seen that the temperature effects suppress the soliton amplitude which is the same as the bright soliton case. However, the temperature does not affect the background soliton amplitude. Furthermore, as the magnetic field decreases or soliton frequency increases, the soliton amplitude increases. This tendency is same as the cold dark soliton case and opposite to the bright soliton case.

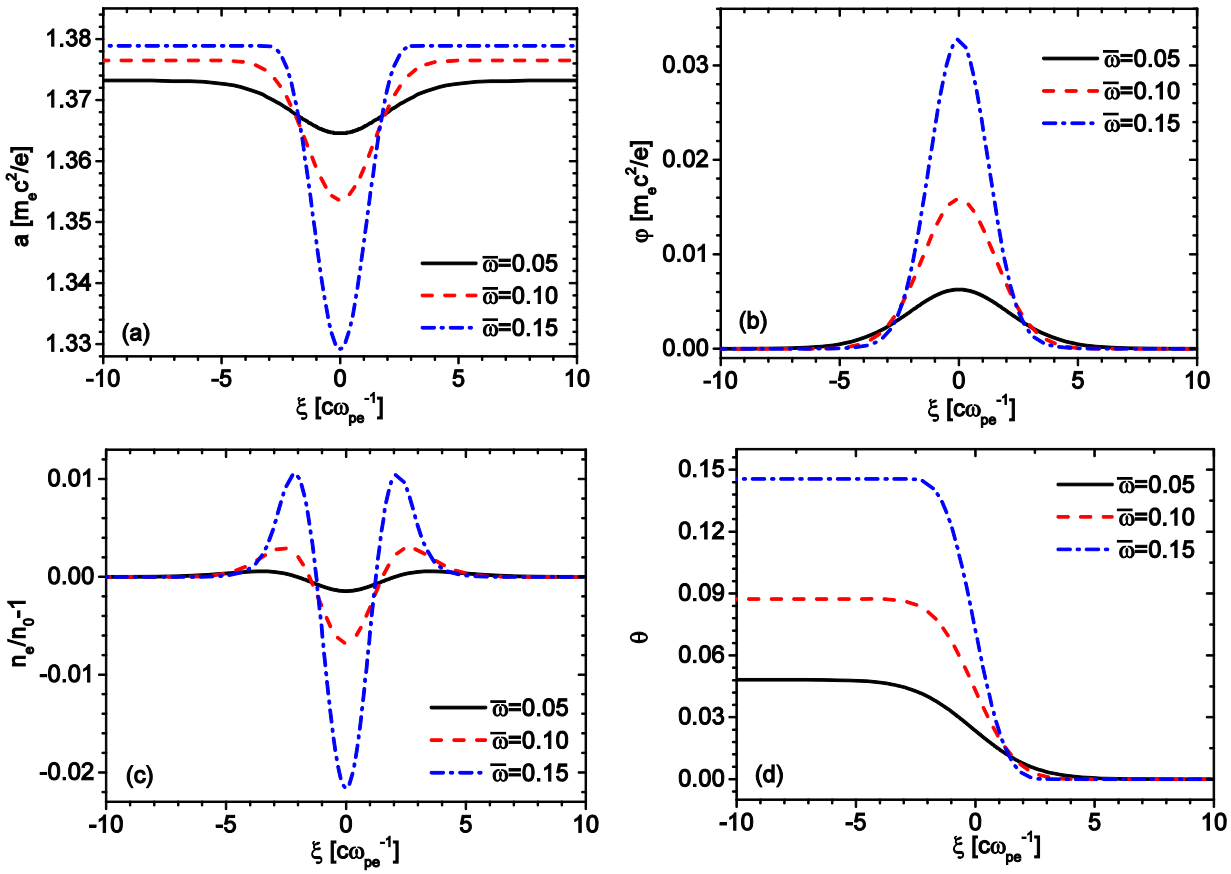

Fig. 6.8. The single hump dark soliton (a) envelop, (b) scalar potential, (c) density and (d) phase with different soliton frequencies in warm plasmas for $\bar{\alpha} = 3.35$, $\bar{k} = 0.75$, $v_{te} = 0.548$ and $\gamma_0 = 1$. The parameter positions in $(\bar{\alpha}, \bar{\omega})$ space are marked by round dots in Fig. 6.5.

6.2.3 Multi-hump dark solitons

It is well-known from the dynamical systems theory that, in the saddle-focus domain, the existence of one prime transverse symmetric homoclinic orbits implies the existence of infinitely many others. The extra homoclinic solutions look like the multiple copies of the prime one. In this case, it means that if a one-hump soliton solution exists, there is a family of multi-hump solitons. In Fig. 6.9, we plot an example of the comparison of one-hump, two-hump and three-hump solitons for the same parameters at the saddle-focus domain. Note that the multi-hump dark solitons in magnetized plasmas is different from the unmagnetized case in that the scalar potential can also have humps and each hump introduces a jump in the phase. In the saddle domain, the homoclinic orbit is usually unique, however, there are some mechanism which can make the multiplicity of the homoclinic solutions. [92] We mention that multi-hump solitons are also observed in the saddle domain.

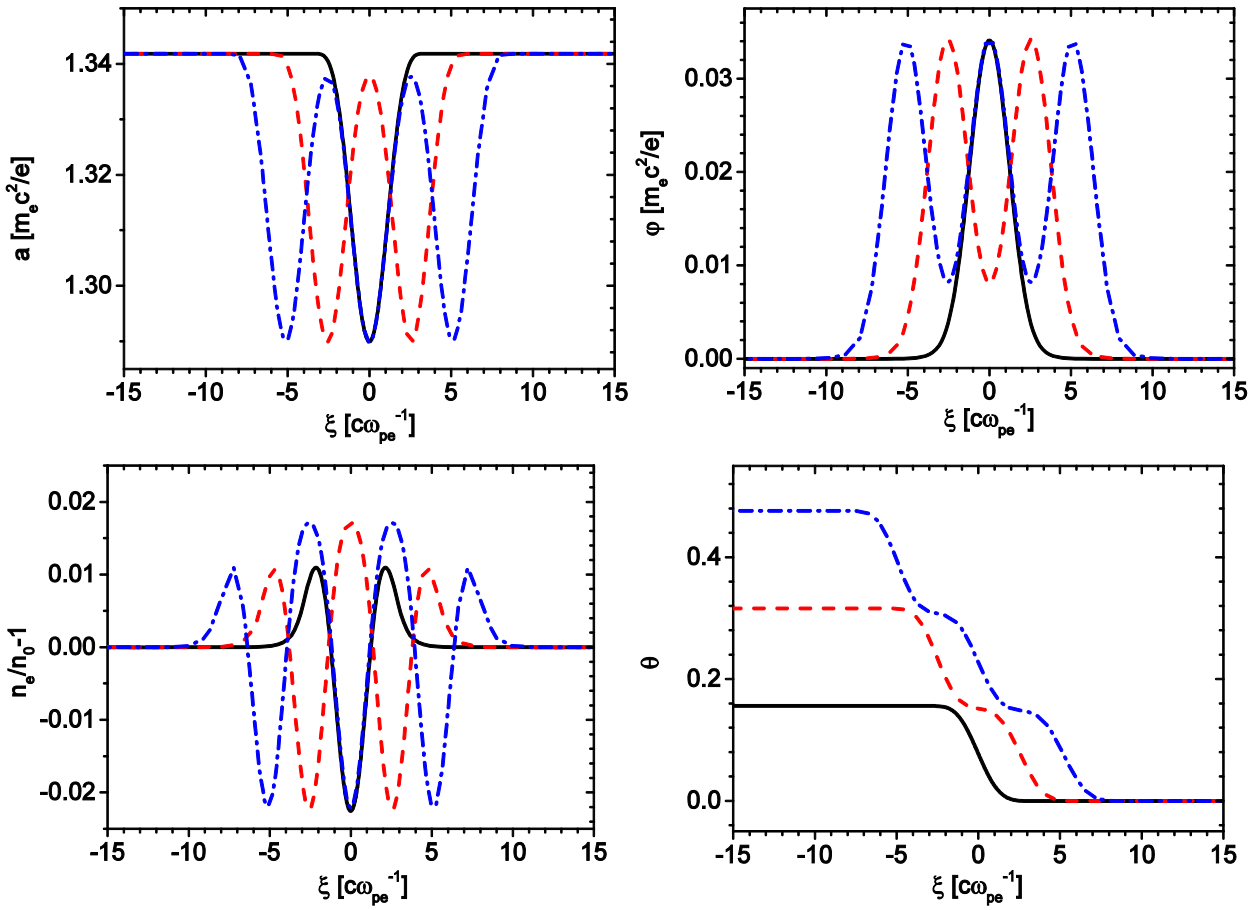

Fig. 6.9. The comparison of single-hump, two-hump and three hump dark soliton (a) envelop, (b) scalar potential, (c) density and (d) phase at the saddle-focus domain with the same parameters $\bar{\omega} = 0.1$, $\bar{k} = 0.75$, $\bar{\alpha} = 3.35$, $v_{te} = 0.548$ and $\gamma_0 = 1$. Each hump introduces a jump in the phase.

6.3 Summary

In this chapter, we have studied the dark soliton formation in magnetized plasmas. The parametric regions for the existence of dark solitons are identified in both cold and warm plasmas. It is found that the temperature effects suppress the soliton amplitude which is the same as the bright soliton case. Furthermore, the temperature makes it possible for the existence of multi-hump solitons. These solitons have multi humps in both the scalar and vector potential profiles, which are different from the solitons in unmagnetized plasmas where they only have multi humps in the vector potential profile. The numerical calculation shows the dark soliton amplitude increases with decreasing magnetic field and increasing soliton frequency. These tendencies are opposite to the bright soliton case.

7. Conclusions and future work

In the previous six chapters, we have presented the research work on the laser plasma interactions in the presence of strong parallel magnetic field, specifically, the various linear and nonlinear propagation modes including the LCP, RCP, electron cyclotron mode as well as the bright and dark solitons. In this chapter, we point out the meaning of our research and give a conclusion about the results. Further, some of the ideas which may be used to extend our research are proposed.

7.1 Conclusion

The ultra-intense laser plasma interactions in the presence of strong parallel magnetic field are of great importance in many applications. Our research aims at understanding the details of the propagation modes and their effects on the laser plasma interactions under different laser intensities, polarizations and magnetic fields. Specifically, the generation condition for the bright and dark solitons is one of our main concerns. Since a significant fraction of the laser energy is converted into solitons, the understanding of the soliton dynamics makes it possible for us to choose the plasma and laser parameters as well as the magnetic field to generate solitons in a controllable manner. One of the potential applications of our research is the magnetically assisted fast ignition where the laser propagates a long distance in the magnetized plasmas. In this case the soliton induced heating may play a role in the energy conversion efficiency. Also there is a possibility of the ultra-short electromagnetic pulse generation by the interactions between the solitons and plasmas wake waves [93,94]. In this case, the electron density modulations in the wake wave serve as parabolic relativistic mirrors and the synchronously oscillating electric and magnetic fields inside the solitons can be reflected in the form of highly compressed and focused electromagnetic pulse with an upper-shifted frequency due to the Doppler effects.

For the sake of convenience, the main results of this research are summarized as follows:

- The exact expressions of the particle's orbit inside the intense linearly and circularly polarized laser field in the presence of strong magnetic field are obtained. Both of the two cases have the resonance

and non-resonance solutions. In linearly polarized case, this orbit is a combination of "8-figure" motion and cyclotron motion. In circularly polarized case, a special situation happens when the cyclotron effects are canceled by the rotation effects of the polarization. In this case, the orbit is the same as the one in linearly polarized laser field without magnetic field, e.g. the "8-figure" structure.

- The relativistic effects on the linear dispersion relations are checked by the PIC simulations. [80, 81] Both the high frequency RCP and LCP branches go down in the dispersion relation plot. Furthermore, in the weakly relativistic regime a new branch appears and the electron cyclotron mode shrinks and totally disappears in the ultra-relativistic regime. The simulation qualitatively matches the theoretical predictions.
- The effects of strong magnetic field on the laser propagation modes and heating in plasmas are investigated with different laser intensities and polarizations by the PIC simulations. The expressions for the linear propagation modes, namely the RCP, LCP and electron cyclotron waves are obtained in the non-uniform plasma areas. Due to the inhomogeneity of plasma, the linearly polarized laser can convert into different propagation modes under different magnetic fields. In the uniform plasmas, the solitary wave together with a density well are observed under certain laser intensity and magnetic field regions. This region shifts to the lower intensity direction as the laser intensity or magnetic field increases. The generation of solitons can greatly increase the heating efficiency up to 37% in 1D simulations, which is comparable to the ECRH heating efficiency. In 2D simulations this enhancement decreases due to the breakup of solitons. The soliton has a very short width and a lower frequency compared to the incident laser and its position shifts as the magnetic field, laser intensity or pre-plasma density profile changes.
- The coupled soliton equations as well as the Hamiltonian of the system are derived in the framework of relativistic, warm fluid model, where the scalar potential φ, the vector potential a and the phase modulation θ are used to describe the longitudinal and transverse waves with zero and non-zero boundary conditions, which correspond to bright or dark solitons, respectively. Different dispersion relations for bright and dark solitons are assumed from the boundary conditions. Using the theory of dynamical systems, the soliton solutions in phase space become the homoclinic or heteroclinic orbits of the 4D $(a, a', \varphi, \varphi')$ reversible autonomous Hamiltonian system, which lie in the intersection of the stable and unstable manifolds. Then the general criterion for the existence of soliton is obtained.
- The coupled soliton equations in cold and warm plasmas are solved numerically through the shooting method and the rational spectral method.
- The parametric regions of the magnetic field and soliton frequency for the existence of bright solitons are obtained in both cold and warm plasmas. In cold plasmas, an additional constraint on the magnetic field and soliton frequency arises from the non-negative condition of the electron density and this

condition disappears in warm plasmas. The numerical calculations show that in the limit of immobile ions, the bright soliton tends to be peaked and stronger as the magnetic field increases and it becomes broader and smaller as the soliton frequency increases. The temperature effects suppress the soliton amplitude. The ion's effects are found to play an important role in determining the lower limit of the soliton frequency, especially when the magnetic field is opposite to the RCP solitary wave propagation direction. The analytical expressions for the small amplitude soliton envelops are obtained under the ion fixed limit and quasi-neutral limit, respectively.

- The parametric regions of the magnetic field, soliton frequency and wavenumber for the existence of dark solitons are obtained in both cold and warm plasmas. The wavenumber is proved to be of great importance in determining the parametric region for dark solitons, e.g. there is no dark solitons when $\bar{k} = 0$. Dark solitons with multiple humps are observed in warm plasmas. These solitons have multiple humps in both the scalar and vector potential profiles, which are different from the solitons in unmagnetized plasmas where they only have multiple humps in the vector potential profile. The numerical calculations of dark solitons without ion's motion show that the dark soliton amplitude decreases with increasing magnetic field and increases with increasing soliton frequency. These tendencies are opposite to the bright solitons. For warm plasmas, the dark soliton amplitude decreases as the temperature increases, which is the same as bright soliton case.

7.2 Extensions of this PhD study

During the PhD, many ideas and results are found but have not been explored further due to the time restrictions. In the following, some ideas are summarized which may be used as an extension of the research.

7.2.1 Chapter 2: The radiation from particle motion and relativistic electron cyclotron mode

- Since the exact expressions for the particle's orbit in the presence of strong magnetic field are obtained, the radiation from this relativistic motion can be calculated. When laser intensity exceeds $10^{23} W/cm^2$, such kind of radiation damping effects become important. [95] In this case, the radiation differs from the usual nonlinear Thomson scattering or the cyclotron radiation. It might be a combination of both effects.
- It has been preliminarily verified by the PIC simulations that the electron cyclotron mode shrinks in the relativistic regime. The details of this phenomena need to be investigated.

7.2.2 Chapter 3: Soliton position dependence and breakup of solitons

- The soliton position dependence on the plasmas density profile, laser intensity, magnetic field, etc. should be further studied.
- The mechanism about the instabilities which lead to the breakup of solitons in 2D simulations needs to be resolved.
- 3D simulations are needed.

7.2.3 Chapter 4: The moving soliton and stability analysis

- In homogeneous plasmas, it seems that the Maxwell-fluid model only admits standing solitons or moving solitons with group velocity equals to the drifting velocity of the plasma. The more generalized case where solitons have arbitrary velocities is needed. Furthermore, the theoretical model in inhomogeneous plasmas should also be developed.
- A theoretical analysis on the soliton stabilities is needed.

7.2.4 Chapter 5: The existence or nonexistence of discrete spectrum soliton

- The theoretical model predicts the potential existence of discrete spectrum solitons under certain parameters (saddle-center regime). Such kind of soliton has been observed in unmagnetized plasmas numerically. [57]. Hence, how to find (or prove the non-existence of) it remains an open problem. This may need more sophisticated numerical calculations.

7.2.5 Chapter 6: The multi-hump dark soliton in the saddle domain

- Generally, the homoclinic orbit is unique in the saddle domain. However, we do observe the multi-hump soliton in the saddle domain. The mechanism which make the multiplicity of the homoclinic solutions should be investigated.

Appendixes

A. Hamiltonian of the soliton system

In this appendix, we validate of the obtained Hamiltonian H. Instead of showing the tedious derivation processes of H, here we simply check its validity by the Hamilton's equations. The obtained Hamiltonian of the system is,

$$H(a,a',\varphi,-\gamma_0^2\varphi') = \frac{1}{2}\left(a'^2 + \bar{\omega}^2 a^2 + \bar{k}^2\frac{a_0^4}{a^2} - \gamma_0^2\varphi'^2\right) + \gamma_0^2\left[v_{te}^2(n_e-1) + \frac{v_{ti}^2}{\rho}(n_i-1)\right] \qquad \text{(A. 1)}$$

with n_e, n_i and $p_{e\perp}, p_{i\perp}, \gamma_e, \gamma_i$ satisfying,

$$v_{te}^2 \ln n_e = \varphi + \frac{1}{2}\bar{\alpha}\gamma_0^2\frac{p_{e\perp}^2}{\gamma_e^2} - \frac{\gamma_e}{\gamma_0^2} - c_{e0}; \qquad v_{ti}^2 \ln n_i = -\rho\varphi - \frac{1}{2}\rho\bar{\alpha}\gamma_0^2\frac{p_{i\perp}^2}{\gamma_i^2} - \frac{\gamma_i}{\gamma_0^2} - c_{i0}. \qquad \text{(A. 2)}$$

$$p_{e\perp} - a = \bar{\alpha}\gamma_0^2\frac{p_{e\perp}}{\gamma_e}; \qquad p_{i\perp} + \rho a = -\rho\bar{\alpha}\gamma_0^2\frac{p_{i\perp}}{\gamma_i}; \qquad \text{(A. 3)}$$

Here c_{e0} and c_{i0} are two constants determined by the boundary conditions. The Hamiltonian $H(a,a',\varphi,-\gamma_0^2\varphi')$ should satisfy the following Hamilton's equations,

$$a' = \frac{\partial H}{\partial a'}; \qquad \varphi' = \frac{\partial H}{\partial(-\gamma_0^2\varphi')}. \qquad \text{(A. 4)}$$

$$a'' = -\frac{\partial H}{\partial a}; \qquad -\gamma_0^2\varphi'' = -\frac{\partial H}{\partial \varphi}. \qquad \text{(A. 5)}$$

Note that n_e, n_i and $p_{e\perp}, p_{i\perp}, \gamma_e, \gamma_i$ are just functions of a and φ, hence it is easy to verify that Eq. (A. 4) is correct. On the other hand, one find,

$$\frac{\partial H}{\partial a} = \left(\bar{\omega}^2 - \bar{k}^2\frac{a_0^4}{a^4}\right)a + \gamma_0^2\left(v_{te}^2\frac{\partial n_e}{\partial a} + \frac{v_{ti}^2}{\rho}\frac{\partial n_i}{\partial a}\right); \qquad \text{(A. 6)}$$

$$\frac{\partial H}{\partial \varphi} = \gamma_0^2 \left(v_{te}^2 \frac{\partial n_e}{\partial \varphi} + \frac{v_{ti}^2}{\rho} \frac{\partial n_i}{\partial \varphi} \right); \tag{A. 7}$$

From Eqs. (A. 2) and (A. 3), we have,

$$\frac{v_{te}^2}{n_e} \frac{\partial n_e}{\partial \varphi} = 1; \qquad \frac{v_{ti}^2}{n_i} \frac{\partial n_i}{\partial \varphi} = -\rho. \tag{A. 8}$$

$$\begin{aligned} \frac{v_{te}^2}{n_e} \frac{\partial n_e}{\partial a} &= \bar{\alpha}\gamma_0^2 \frac{p_{e\perp}}{\gamma_e} \frac{\partial}{\partial a}\left(\frac{p_{e\perp}}{\gamma_e}\right) - \frac{1}{\gamma_0^2}\frac{\partial \gamma_e}{\partial a} = \frac{p_{e\perp}}{\gamma_e}\left(\frac{\partial p_e}{\partial a} - 1\right) - \frac{1}{\gamma_0^2}\frac{\gamma_0^2 p_{e\perp}}{\gamma_e}\frac{\partial p_e}{\partial a} = -\frac{p_{e\perp}}{\gamma_e} \\ \frac{v_{ti}^2}{n_i} \frac{\partial n_i}{\partial a} &= -\rho\bar{\alpha}\gamma_0^2 \frac{p_{i\perp}}{\gamma_i} \frac{\partial}{\partial a}\left(\frac{p_{i\perp}}{\gamma_i}\right) - \frac{1}{\gamma_0^2}\frac{\partial \gamma_i}{\partial a} = \frac{p_{i\perp}}{\gamma_i}\left(\frac{\partial p_i}{\partial a} + \rho\right) - \frac{1}{\gamma_0^2}\frac{\gamma_0^2 p_{i\perp}}{\gamma_i}\frac{\partial p_i}{\partial a} = \frac{\rho p_{i\perp}}{\gamma_i} \end{aligned} \tag{A. 9}$$

Note that we have used the relation $\partial\gamma_s/\partial a = (\gamma_0^2 p_s/\gamma_s)(\partial p_s/\partial a)$ with $s = e, i$. Combining Eqs. (A. 6)-(A. 9), we find,

$$\frac{\partial H}{\partial a} = \left(\bar{\omega}^2 - \bar{k}^2 \frac{a_0^4}{a^4}\right) a + \gamma_0^2 \left(-n_e \frac{p_{e\perp}}{\gamma_e} + n_i \frac{p_{i\perp}}{\gamma_i}\right) = -a''; \tag{A. 10}$$

$$\frac{\partial H}{\partial \varphi} = \gamma_0^2 (n_e - n_i) = -(-\gamma_0^2 \varphi''); \tag{A. 11}$$

This verifies the validity of the Hamiltonian.

B. Additional fixed points of the Hamiltonian

In this appendix, we calculate the additional fixed points $Q_*^{\pm}$ of the system besides $Q_0(Q_0^{\pm})$. $Q_*^{\pm}$ should satisfy the following equations,

$$\bar{\omega}^2 - \bar{k}^2 \frac{a_0^4}{a^4} = n\left(\frac{\gamma_0^2}{\gamma_e - \bar{\alpha}\gamma_0^2} + \frac{\rho\gamma_0^2}{\gamma_i + \rho\bar{\alpha}\gamma_0^2}\right); \tag{B. 1}$$

$$p_{e\perp} - a = \bar{\alpha}\gamma_0^2 \frac{p_{e\perp}}{\gamma_e}; \qquad p_{i\perp} + \rho a = -\rho\bar{\alpha}\gamma_0^2 \frac{p_{i\perp}}{\gamma_i} \tag{B. 2}$$

with $n = 1 - \rho\left(\bar{\omega}^2 a^2 + \bar{k}^2 a_0^4/a^2\right)/(2\gamma_0^2 c_s^2)$. Here a_0 is the dark soliton amplitude at the infinity space, $\rho = m_e/m_i$ is the electron-ion mass ratio and the ion acoustic velocity c_s is denoted as $c_s^2 = v_{te}^2 + \rho v_{ti}^2$.

a. Bright solitons

For the bright solitons $\bar{\omega} = \omega$, $\bar{k} = 0$ and $\bar{\alpha} = \alpha$. Assuming ions are nonrelativistic and using the variable transformation $p_{e\perp} = \sinh u$, where $\sinh u$ is the hyperbolic sine function, we have $p_{i\perp} \approx -\rho a/(1+\rho\alpha\gamma_0)$ with $a = \sinh u - \alpha\gamma_0 \tanh u$. Then at $Q_*^{\pm}$ Eq. (B. 1) becomes,

$$\omega^2(1+\rho\alpha\gamma_0)(1-\alpha\gamma_0 \operatorname{sech} u^*) = \gamma_0(\rho + \operatorname{sech} u^*)\left[1 - \frac{\rho\omega^2}{2\gamma_0^2 c_s^2}(\sinh u^* - \alpha\gamma_0 \tanh u^*)^2\right] \quad \text{(B. 3)}$$

Notice that the right hand side (RHS) of Eq. (B. 3) is always larger than zero ($n^* > 0$), which requires $-1/\rho \le \alpha\gamma_0 \le \cosh u^*$. Furthermore, in this region the derivative of RHS of Eq. (B. 3) is,

$$D_R = -\sinh u^*\left[\gamma_0 n^* \operatorname{sech}^2 u^* + \frac{\rho\omega^2}{\gamma_0 c_s^2}(1+\rho\cosh u^*)(1-\alpha\gamma_0 \operatorname{sech} u^*)(1-\alpha\gamma_0 \operatorname{sech}^3 u^*)\right]$$

It is smaller than zero when $u^* > 0$ and larger than zero when $u^* < 0$. Hence the RHS of Eq. (B. 3) has a maximum given by,

$$\begin{cases} \gamma_0(\rho+1) & \text{when } \alpha\gamma_0 < 1 \\ \gamma_0[\rho + 1/(\alpha\gamma_0)] & \text{when } \alpha\gamma_0 \ge 1 \end{cases}$$

On the other hand, the derivative of LHS of Eq. (B. 3) is,

$$D_L = \alpha\gamma_0\omega^2(1+\rho\alpha\gamma_0)\operatorname{sech} u^* \tanh u^*$$

If $\alpha\gamma_0 > 0$, the left hand side (LHS) of Eq. (B. 3) is an increasing function of $|u|$. It has the following minimum,

$$\begin{cases} \omega^2(1+\rho\alpha\gamma_0)(1-\alpha\gamma_0) & \text{when } 0 < \alpha\gamma_0 < 1 \\ 0 & \text{when } \alpha\gamma_0 \ge 1 \end{cases}$$

Thus, Eq. (B. 3) always has two solutions when

$$\alpha\gamma_0 \ge 1. \quad \text{(B. 4)}$$

If $0 < \alpha\gamma_0 < 1$, Eq. (B. 3) will have two solutions when $\gamma_0(\rho+1) > \omega^2(1+\rho\alpha\gamma_0)(1-\alpha\gamma_0)$ is satisfied. Then it gives,

$$\begin{cases} 0 < \alpha\gamma_0 < 1 & \text{when } \omega^2 \le 4\gamma_0\rho/(1+\rho) \\ \beta_+ < \alpha\gamma_0 < 1 & \text{when } \omega^2 > 4\gamma_0\rho/(1+\rho) \end{cases} \quad \text{(B. 5)}$$

Here $\beta_\pm = \left[\rho - 1 \pm \sqrt{(\rho+1)^2 - 4\rho(\rho+1)\gamma_0/\omega^2}\right]/(2\rho)$. If $-1/\rho < \alpha\gamma_0 < 0$, the LHS of Eq. (B. 3) is also a decreasing function of $|u|$ and it has a maximum $\omega^2(1+\rho\alpha\gamma_0)(1-\alpha\gamma_0)$. The comparison of the decreasing rate between RHS and LHS can be calculated by,

$$
\begin{aligned}
&|D_R| - |D_L| \\
&> |\sinh u^*| \left[\frac{\rho\omega^2}{\gamma_0 c_s^2} (1 + \rho \cosh u^*)(1 - \alpha\gamma_0 \operatorname{sech} u^*)(1 - \alpha\gamma_0 \operatorname{sech}^3 u^*) + \omega^2 (1 + \rho\alpha\gamma_0)\alpha\gamma_0 \operatorname{sech}^2 u^* \right] \\
&> |\sinh u^*| \{\omega^2 (1 + \rho\alpha\gamma_0)[(1 - \alpha\gamma_0 \operatorname{sech} u^*)(1 - \alpha\gamma_0 \operatorname{sech}^3 u^*) + \alpha\gamma_0 \operatorname{sech}^2 u^*]\} \\
&= \omega^2 (1 + \rho\alpha\gamma_0) |\sinh u^*| \{1 - \alpha\gamma_0 \operatorname{sech} u^* [1 - \operatorname{sech} u^* + \operatorname{sech}^2 u^* (1 - \alpha\gamma_0 \operatorname{sech} u^*)]\} \\
&> 0
\end{aligned}
$$

Note that we have used the inequality $\rho/(\gamma_0\, c_s^2) > 1$. This is because $\gamma_0\, c_s^2/\rho$ represents the square of electron acoustic velocity and it should be smaller than the speed of light. Hence, the RHS decreases faster than the LHS. Then the existence of $Q_*^{\pm}$ requests $\gamma_0(\rho + 1) > \omega^2(1 + \rho\alpha\gamma_0)(1 - \alpha\gamma_0)$, or,

$$
\begin{cases}
-1/\rho < \alpha\gamma_0 < 0 & \text{when } \omega^2 \le 4\gamma_0\rho/(1+\rho) \\
-1/\rho < \alpha\gamma_0 < \beta_- & \text{when } \omega^2 > 4\gamma_0\rho/(1+\rho)
\end{cases}
\tag{B. 6}
$$

Combining (B. 4)-(B. 6), we find that for the bright solitons the system has two additional fixed point $Q_*^{\pm}$ if $\alpha\gamma_0$ is in the following interval,

$$
\begin{cases}
-1/\rho < \alpha\gamma_0 < \infty & \text{when } \omega^2 \le 4\gamma_0\rho/(1+\rho) \\
-1/\rho < \alpha\gamma_0 < \beta_-, \quad \beta_+ < \alpha\gamma_0 < \infty & \text{when } \omega^2 > 4\gamma_0\rho/(1+\rho)
\end{cases}
\tag{B. 7}
$$

For immobile ions ($\rho \to 0$), condition (B. 7) is reduced to $1 - \gamma_0/\omega^2 < \alpha\gamma_0 < \infty$. In this case, $n^* \equiv 1$ and Eq. (B. 1) has the exact solution,

$$
\begin{cases}
a^* = \pm \left[\dfrac{\gamma_0^2}{\omega^4} - \dfrac{1}{(1+\alpha\omega^2)^2} \right]^{-1/2} \\
\varphi^* = \dfrac{\alpha}{2} + \dfrac{1}{\omega^2} - \dfrac{1}{\gamma_0} + \dfrac{\alpha\omega^4}{2\gamma_0^2(1+\alpha\omega^2)^2}
\end{cases}
\tag{B. 8}
$$

b. Dark solitons

For the dark soliton, it is difficult to get the simple conditions for $Q_*^{\pm}$ as shown by (B. 7). For simplicity, we only consider the immobile ion case, then $\gamma_e^* = \gamma_0^2\left[\bar{\alpha} + 1/\left(\bar{\omega}^2 - \bar{k}^2\, a_0^4/a^{*4}\right)\right]$ and a^* satisfies,

$$
a^{*2} = \frac{\gamma_0^2}{\left(\bar{\omega}^2 - \bar{k}^2\, a_0^4/a^{*4}\right)^2} - \frac{1}{\left[\bar{\alpha}\left(\bar{\omega}^2 - \bar{k}^2\, a_0^4/a^{*4}\right) + 1\right]^2}.
\tag{B. 9}
$$

Here $a_0^2 = (\gamma_{e0}^2/\gamma_0^2 - 1)(1 - \bar{\alpha}\gamma_0^2/\gamma_{e0})$, $\gamma_{e0} = \gamma_0^2\left[\bar{\alpha} + 1/\left(\bar{\omega}^2 - \bar{k}^2\right)\right]$ and $\bar{\omega}, \bar{k}, \bar{\alpha}$ should satisfy,

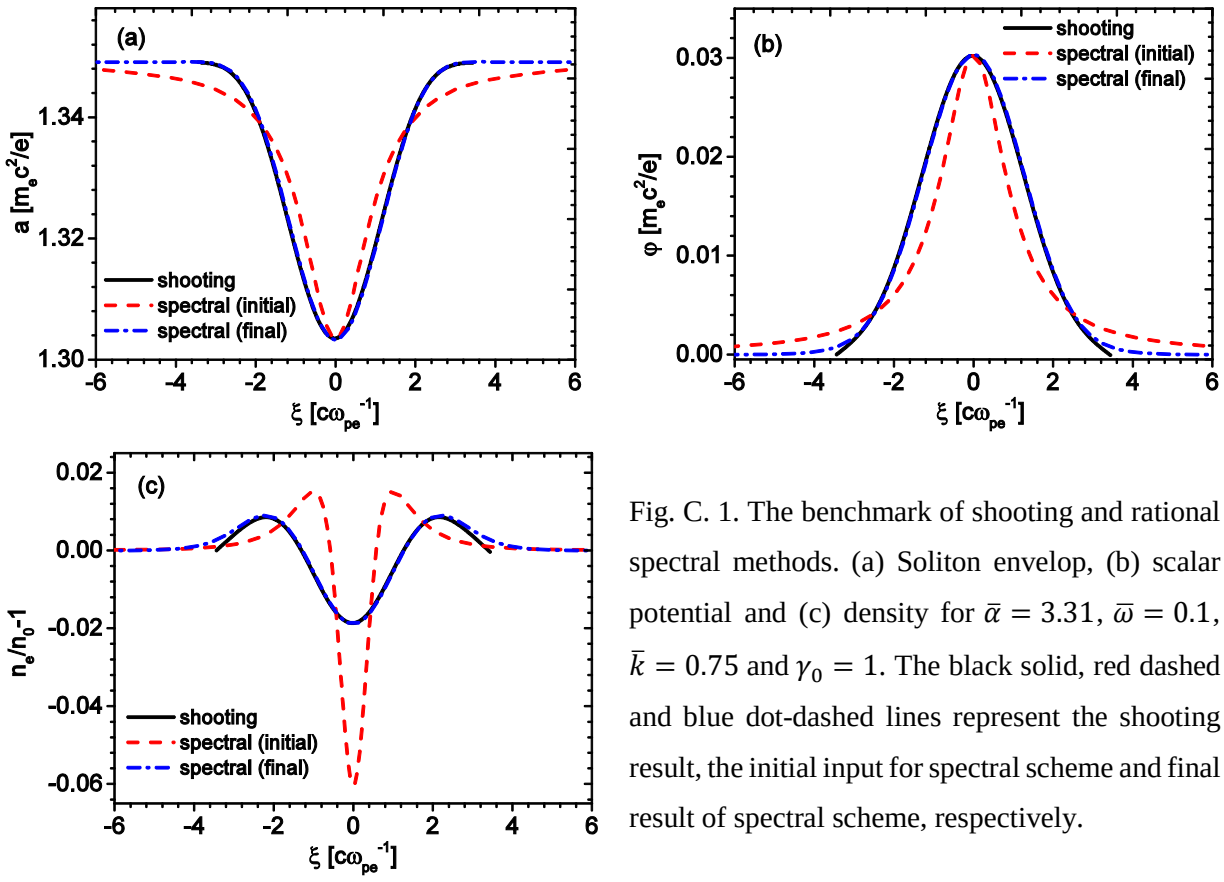

Fig. C. 1. The benchmark of shooting and rational spectral methods. (a) Soliton envelop, (b) scalar potential and (c) density for $\bar{\alpha} = 3.31$, $\bar{\omega} = 0.1$, $\bar{k} = 0.75$ and $\gamma_0 = 1$. The black solid, red dashed and blue dot-dashed lines represent the shooting result, the initial input for spectral scheme and final result of spectral scheme, respectively.

$$\gamma_0\left[\bar{\alpha} + 1/\left(\bar{\omega}^2 - \bar{k}^2\right)\right] > 1 \tag{B. 10}$$

C. Benchmark for the numerical methods

The coupled soliton equations are solved by the shooting method and rational spectral method. Since they are totally different schemes, they can be used to benchmark each other. In this appendix, we show the benchmark for the numerical calculations.

For simplified 2D Hamiltonian systems, e.g. cold plasmas, both the shooting and rational spectral schemes can be applied and they give the same accurate results. When temperature effects are included, the accuracy of shooting scheme decreases. This is due to the temperature term $v_{te}^2 \ln n_e$ in the longitudinal force balance equations,

$$v_{te}^2 \ln n_e = \varphi + \frac{1}{2}\bar{\alpha}\gamma_0^2 \frac{p_{e\perp}^2}{\gamma_e^2} - \frac{\gamma_e}{\gamma_0^2} - c_{e0} \tag{C. 1}$$

Note that $v_{te}^2 < 1$. Any numerical error of density induced by the right hand side of Eq. (C. 1) will be increased by the factor $1/v_{te}^2$ and further amplified by the exponential function. This error becomes non-negligible at the boundary where the scalar potential tends to zero (e.g. see the black solid line of the density profile in Fig. C. 1(c)). Hence, in 4D Hamiltonian systems, we used the rational spectral method after the shooting results. The minimum and maximum of the shooting profiles are used to build up the initial input as shown by the red dashed line in Fig. C. 1, where the comparison of shooting and rational spectral results are plotted. Here the back solid line represents the shooting result, the red dashed line is the initial input for the rational spectral scheme and the blue dot-dashed line is the final result. As we can see, while the soliton envelop is calculated correctly by both schemes, there is significant difference in the density and scalar potential profiles at the place far from the soliton center. For the rational spectral scheme, the density and scalar potential converge to the boundary values correctly. The consistence of the two methods shows the validity of the numerical calculations.

Scientific contributions

Published peer-reviewed papers

(Author underlined)

1. Wu Feng, Jiquan Li and Yasuaki Kishimoto; "*Relativistic soliton formation in laser magnetized plasma interactions*", J. Phys.:Conf. Ser. 717, 012031 (2016)
2. Wu Feng, Jiquan Li and Yasuaki Kishimoto; "*Laser propagation and soliton generation in strongly magnetized plasmas*", Physics of Plasmas, 23, 032102 (2016).
3. Wu Feng, Jiquan Li and Yasuaki Kishimoto; "*Theory on bright and dark soliton formation in strongly magnetized plasmas*", Physics of Plasmas. (Accepted for publication, 2016).

Presentations at academic conferences and symposiums

(Speaker underlined)

1. Wu Feng, Jiquan Li and Yasuaki Kishimoto, "*Soliton formation in strongly magnetized plasmas*", High Energy Density Sciences 2016 (HEDS 2016), May, 2016, Yokohama, Japan (Poster).
2. Wu Feng, Jiquan Li and Yasuaki Kishimoto, "*Relativistic bright soliton formation in laser magnetized plasma interactions*", 9th International Conference on Inertial Fusion Sciences and Applications (IFSA 2015), September, 2015, Seattle, Washington, USA (Poster).
3. Wu Feng, Daiki Kawahito, and Yasuaki Kishimoto; "*Effects of magnetic field on intense laser matter interactions*", The Physical Society of Japan 2015 Annual Meeting (JPS 2015), March, 2015, Tokyo, Japan (Oral).
4. Wu Feng, and Yasuaki Kishimoto; "*High power laser plasma interactions in the presence of strong magnetic field* ", International School and Workshop on Matter in Extreme Conditions: from Material Science to Planetary Physics. (MECMATPLA), February, 2015, Montgenevre, France (Poster).
5. Wu Feng, "*Laser plasma interactions in inhomogeneous magnetized plasma*", レーザプラズマ科学のため最先端シミュレーションコード共同開発・利用に関する研究会, January, 2015, Osaka, Japan (Oral).

6. Wu Feng, Daiki Kawahito, and Yasuaki Kishimoto, *"High power laser plasma interactions in the presence of strong magnetic field"*, Plasma Conference 2014, November, 2014, Niigata, Japan (Oral).
7. Wu Feng, Daiki Kawahito, and Yasuaki Kishimoto; *"Laser plasma interaction in inhomogeneous magnetized plasma*", The 2nd International Conference on High Energy Density Physics. (ICHEDP), September, 2014, Beijing, China (Poster).
8. Wu Feng, Natsumi Iwata, Daiki Kawahito *"High intense-laser matter interaction in magnetized solid density plasma"*, The Physical Society of Japan 2014 Annual Meeting (JPS 2014), March, 2014, Hiratsuka, Kanagawa, Japan (Oral).

Bibliography

[1] D. Strickland and G. Mourou, Opt. Commun. **56**, 219 (1985).

[2] P. Maine, D. Strickland, P. Bado, M. Pessot and G. Mourou, IEEE J. Quantum Electron. **24**, 398 (1988)

[3] N. Sarukura, Y. Nishida and H. Nakano, Opt. Lett **16**, 153(1991).

[4] D. E. Spence, P. N. Kean and W. Sibbett, Opt. Lett **16**, 42(1991).

[5] A. L. Peratt, Astrophys Space Sci, **242**, 93 (1996)

[6] H. Daido, M. Nishiuchi and A. S. Pirozhkov, Rep. Prog. Phys. **75**, 056401 (2012).

[7] E. S. Sarachik and G. T. Schappert, Phys. Rev. D, **10**, 2738 (1970).

[8] H. Schwoerer, S. Afr. J. Sci, **104**, 299, (2008).

[9] P. Sprangle, E. Esarey, J. Krall and G. Joyce, Phys. Rev. Lett. **69**, 2200 (1992).

[10] T. Tajima and J. M. Dawson, Phys. Rev. Lett. **43**, 267, (1979).

[11] S. P. D. Mangles, C. D. Murphy, Z. Najmudin, A. G. R. Thomas, J. L. Collier, A. E. Dangor, E. J. Divall, P. S. Foster, J. G. Gallacher, C. J. Hooker, D. A. Jaroszynski, A. J. Langley, W. B. Mori, P. A. Norreys, F. S. Tsung, R. Viskup, B. R. Walton and K. Krushelnick, Nature, **431**, 535 (2004).

[12] C. G. R. Geddes, Cs. Toth, J. van Tilborg, E. Esarey, C. B. Schroeder, D. Bruhwiler, C. Nieter, J. Cary and W. P. Leemans, Nature, **431**, 538 (2004).

[13] J. Faure, Y. Glinec, A. Pukhov, S. Kiselev, S. Gordienko, E. Lefebvre, J.-P. Rousseau, F. Burgy and V. Malka, Nature, **431**, 541 (2004).

[14] D. Umstadter, J. Phys. D: Appl. Phys. **36**, R151, (2003).

[15] P. Sprangle, C. M. Tang and E. Esarey, IEEE Trans. Plasma Sci, **PS-15**, 145 (1987).

[16] G. Z. Sun, E. Ott, Y. C. Lee and P. Guzdar, Phys. Fluids, **30**, 526 (1987).

[17] A. B. Borisov, O. B. Shiryaev, A. McPherson, K. Boyer and C. K. Rhodes, Plasma. Phys. Control. Fusion **37**, 569 (1995).

[18] C. G. R. Geddes, Cs. Toth, J. van Tilborg, E. Esarey and C. B. Schroeder, D. Bruhwiler, C. Nieter, J. Cary and W. P. Leemans, Phys. Plasmas **12**, 056709 (2005).

[19] E. Esarey, P. Sprangle, J. Krall, A. Ting and G. Joyce, Phys. Fluids B, **5**, 2690 (1993).

[20] L. Gorbunov, P. Mora and T. M. Antonse, Jr. Phys. Rev. Lett. **76**, 2495 (1996).

[21] S. V. Bulanov, M. Lontano, T. Zh. Esirkepov, F. Pegoraro and A. M. Pukhov, Phys. Rev. Lett. **76**, 3562 (1996).

[22] M. Borghesi, A. J. Mackinnon, R. Gaillard and O. Willi, Phys. Rev. Lett, **80**, 5137 (1998).

[23] G. A. Askar'yan, S. V. Bulanov, F. Pegoraro and A. M. Pukhov, JETP Lett. **60**, 251 (1994).

[24] A. Pukhov and J. Meyer-ter-Vehn, Phys. Rev. Lett. **76**, 3975 (1996).

[25] B. Bhattacharyya, P. Mulser and U. Sanyal, Phys. Lett. A, **249**, 324 (1998).

[26] S. Fujioka, Z. Zhang, K. Ishihara, K. Shigemori, Y. Hironaka, T. Johzaki, A. Sunahara, N. Yamamoto, H. Nakashima, T. Watanabe, H. Shiraga, H. Nishimura and H. Azechi, Scientific Reports. **3**, 1170 (2013).

[27] H. B. Cai, S. P. Zhu, M. Chen, S. Z. Wu, X. T. He and K. Mima, Phys. Rev. E, **83**, 036408 (2011).

[28] H. B. Cai, S. P. Zhu and X. T. He, Phys. Plasmas. **20**, 072701 (2013).

[29] W. M. Wang, P. Gibbon, Z. M. Sheng, and Y. T. Li, Phys. Rev. Lett. **114**, 015001 (2015).

[30] D. J. Stozzi, M. Tabak, D. J. Larson, L. Divol, A. J. Kemp, C. Bellei, M. M. Marink and M. H. Key, Phys. Plasmas. **19**, 072711 (2012).

[31] P. Y. Chang, G. Fiksel, M. Hohenberger, J. P, Knauer, R. Betti, F. J. Marshall, D. D. Meyerhofer, F. H. Seguin, and R. D. Petrasso, Phys. Rev. Lett. **107**,035006 (2011).

[32] W. M. Wang, P. Gibbon, Z. M. Sheng, and Y. T. Li, Phys. Rev. Lett. **114**, 253901 (2015).

[33] L. Bhasin, V. K. Tripathi, and P. Kumar, Phys. Plasmas **23**, 023101 (2016)

[34] R. K. Singh and R. P. Sharma, Phys Plasmas **21**, 113109 (2014).

[35] D. Dorranian, M. Starodubtsev, H. Kawakami, H. Ito, N. Yugami, and Y. Nishida, Phys. Rev. E **68**, 026409 (2003).

[36] P. Jha, R. K. Mishra, G. Raj, and A. K. Upadhyay, Phys. Plasmas **14**, 053107 (2007).

[37] P. Sharma and R. P. Sharma, Phys. Plasmas **19**, 122106 (2012).

[38] Y. Nishida, M. Yoshizumi, and R. Sugihara, Phys. Fluids **28**, 1574 (1985).

[39] N. Yugami, K. Kikuta, and Y. Nishida, Phys. Rev. Lett. **76**, 1635 (1996).

[40] H. Chen, G. Fiksel, D. Barnak, P. Y. Chang, R. F. Heeter, A. Link, and D. D. Meyerhofer, Phys. Plasmas **21**, 040703 (2014).

[41] M. Borghesi, S. Bulanov, D. H. Campbell, R. J. Clarke, T. Zh. Esirkepov, M. Galimberti, L. A. Gizzi, A. J. MacKinnon, N. M. Naumova, F. Pegoraro, H. Ruhl, A. Schiavi, and O. Willi, Phys. Rev. Lett. **88**, 135002 (2002).

[42] S. V. Bulanov, T. Zh. Esirkepov, N. M. Naumova, F. Pegoraro and V. A. Vshivkov, Phys. Rev. Lett. **82**, 3440 (1999).

[43] N. M. Naumova, S. V. Bulanov, T. Zh. Esirkepov, D. Farina, K. Nishihara, F. Pegoraro, H. Ruhl and A. S. Sakharov, Phys. Rev. Lett. **87**, 185004 (2001)

[44] D. J. Korteweg, and G. De Vries, Phil. Mag. **39**, 442 (1895).

[45] E. Fermi, J. R. Pasta, and S. M. Ulam, Los Alamos Sci. Lab. Rep., LA-1940 (1955).

[46] N. Zabusky, and M. Kruskal, Phys. Rev. Lett, **15**, 240 (1965).

[47] W. Hereman, Mathematics of Complexity and Dynamical Systems, 1520 (2012)

[48] Y. S. Kivshar, and B. Luther-Davies, Phys. Rep., **298**, 81 (1998).

[49] L. F. Mollenauer, R. H. Stolen, and J. P. Gordon, Phys. Rev. Lett. **45**, 1095 (1980).

[50] P. Emplit, J. P. Hamaide, F. Reynaud, C. Froehly and A. Barthelemy, Opt. Commun. **62**, 374 (1987).

[51] W. J. Tomlinson, R. J. Hawkins, A. M. Weiner, J. P. Heritage, and R. N. Thurston, J. Opt. Soc. Am. B 6, 329 (1989)

[52] H. H. Chen and C. S. Liu, Phys. Rev. Lett. **37**, 693 (1976).

[53] Y. Sentoku, T. Zh. Esirkepov, K. Mima, K. Nishihara, F. Califano, F. Pegoraro, H. Sakagami, Y. Kitagawa, N. M. Naumova and S. V. Bulanov, Phys. Rev. Lett. **83**, 3434 (1999).

[54] V. A. Kozlov, A. G. Litvak and E. V. Suvorov, JETP **49**, 75 (1979)

[55] P. K. kaw, A. Sen, and T. Katsouleas, Phys. Rev. Lett. **68**, 3172 (1992)

[56] S. Poornakala, A. Das, A. Sen, and P. K. Kaw, Phys. Plasmas. **9**, 1820 (2002)

[57] D. Farina and S. V. Bulanov, Fiz. Plazmy **27,** 680 (2001) [Plasma Phys. Rep. **27**, 641 (2001)].

[58] D. Farina and S. V. Bulanov, Phys. Rev. Lett. **86**, 5289 (2001).

[59] D. Farina and S. V. Bulanov, Plasma Phys. Controlled Fusion **47**, A73 (2005)

[60] M. Lontano, S. Bulanov and J. Koga, Phys. Plasmas. **8**, 5113 (2001)

[61] S. Poornakala, A. Das, P. K. Kaw, A. Sen, Z. M. Sheng, Y. Sentoku, K. Mima and K. Nishikawa, Phys. Plasmas. **9**, 3802, (2002)

[62] T. Zh. Esirkepov, F. F. Kamenets, S. V. Bulanov and N. M. Naumova: JETP Lett. **68**, 36 (1998).

[63] G. Sanchez-Arriaga, E. Siminos, and E. Lefebvre, Plasma Phys. Controlled Fusion **53**, 045011 (2011)

[64] G. Sanchez-Arriaga, E. Siminos, and E. Lefebvre, Phys. Plasma **18**, 082304 (2011)

[65] L. Hadzievski, M. S. Jovanovic, M. M. Skoric and K. Mima, Phys. Plasmas **9**, 2569 (2002).

[66] A. Mancic, L. Hadzievski and M. M. Skoric, Phys. Plasmas **13**, 052309 (2006).

[67] G. Lehmann, E. W. Laedke and K. H. Spatschek, Phys. Plasmas **13**, 092302 (2006).

[68] V. Saxena, A. Das, A. Sen and P. Kaw, Phys. Plasmas **13**, 032309 (2006).

[69] V. Saxena, A. Das, S. Sengupta, P. Kaw and A. Sen, Phys. Plasmas **14**, 072307 (2007).

[70] G. Lehmann, E. W. Laedke and K. H. Spatschek, Phys. Plasmas **15**, 072307 (2008).

[71] V. I. Karpman and E. M. Krushkal, Sov. Phys. JETP **28**, 277 (1969).

[72] V. I. Karpman, and H. Washimi, J. Plasma Phys. **18**, 173 (1977).

[73] V. I. Berezhiani, and D. D. Tskhakaya. Fiz. Plazmy **7**, 675 (1981) [Sov. J. Plasma Phys. **7**, 369 (1981)].

[74] P. K. Shukla, and L. Stenflo, Phys. Rev. A **30**, 2110 (1984).

[75] A. Hasegawa, Phys. Fluids. **15**, 870 (1972).

[76] P. K.Shukla, and L. Stenflo, Phys. Rev. A. **30**, 2110 (1984).

[77] N. N. Rao, P. K. Shukla, and M. Y. Yu, Physics. Fluids **27**, 2664 (1984).

[78] D. Farina, M. Lontano, and S. Bulanov, Phys. Rev. E **62**, 4146 (2002)

[79] J. Borhanian, I. Kourakis, and S. Sobhanian, Phys. Lett. A **373**, 3667 (2009)

[80] L. Stenflo, Phys. Scr. **14**, 320 (1976).

[81] N. A. Papuashvili, V. S. Paverman and N. L. Tsintsadze, Plasma Phys. Contr. Fusion **27**, 91 (1984).

[82] Y. Kishimoto and T. Masaki, J. Plasmas Phys. **72**, 971 (2006).

[83] T. Masaki and Y. Kishimoto, J. Plasma Fusion Res. **81**, 643 (2005).

[84] D. G. Swanson, *Plasma Waves* (IOP Publishing, Bristol, 2003), Section 2.12.

[85] S. Wiggins, *Introduction to Applied Nonlinear Dynamical Systems and Chaos,* (Springer Verlag, 2nd edition, 2003) Chap. 3 and 20

[86] A. R. Champneys, Physica D, **112**, 158(1998)

[87] Y. Liu, L. Liu , and T. Tang, J. Comput. Phys. **111**, 373(1994)

[88] B. Krauskope, H. M. Osinga, E. J. Doedel, M. E. Henderson, J. Guckenheimer, A. Vladimirsky, M. Dellnitz and O. Junge, Int. J. Bifurcation Chaos. **763**, 15(2005)

[89] E. J. Doedel, Congr. Numer. **30**, 265(1981)

[90] E. J. Doedel, B. E. Oldeman, A. R. Champneys, F. Dercole, T. Fairgrieve, A. Y. Kuznstsov, B. Sandstede and X. J. Wang, C. H. Zhang available via http://cmvl.cs.concordia.ca/.

[91] E. L. Allgower and K. Georg, *Introduction to numerical continuation methods,* (SIAM, 2003) Chap. 1.

[92] B. Sandstede, C. K. R.T. Jones and J .C. Alexander, Physca D, **106**, 167 (1997).

[93] A. Isanin, S. S. Bulanov, F. kamenets and F. Pegoraro, Phys. Lett. A, **337**, 107 (2005)

[94] S. S. Bulanov, T. Zh. Esirkepov, F. F. kamenets and F. Pegoraro, Phys. Rev. E, **73**, 036408 (2006)

[95] J. Koga, T. Zh. Esirkepov and S. V. Bulanov, Phys. Plasmas **12**, 093106 (2005).